# EPITAXIAL GROWTH OF SEMI-POLAR (11-22) GALLIUM NITRIDE FOR UV PHOTOSENSING APPLICATION

ABDULLAH HAAZIQ BIN AHMAD MAKINUDIN

FACULTY OF SCIENCE
UNIVERSITI MALAYA
KUALA LUMPUR

2020

# EPITAXIAL GROWTH OF SEMI-POLAR (11-22) GALLIUM NITRIDE FOR UV PHOTOSENSING APPLICATION

**ABDULLAH HAAZIQ BIN AHMAD MAKINUDIN**

**THESIS SUBMITTED IN FULFILMENT OF THE REQUIREMENTS FOR THE DEGREE OF DOCTOR OF PHYLOSOPHY**

**DEPARTMENT OF PHYSICS**
**FACULTY OF SCIENCE**
**UNIVERSITI MALAYA**
**KUALA LUMPUR**

**2020**

**UNIVERSITY OF MALAYA**

**ORIGINAL LITERARY WORK DECLARATION**

Name of Candidate: **ABDULLAH HAAZIQ BIN AHMAD MAKINUDIN**

Matric No: **SVA170014**

Name of Degree: **DOCTOR OF PHYLOSOPHY**

Title of Thesis ("this Work"):

**EPITAXIAL GROWTH OF SEMI-POLAR (11-22) GALLIUM NITRIDE FOR UV PHOTOSENSING APPLICATION**

Field of Study:

**EXPERIMENTAL PHYSICS**

I do solemnly and sincerely declare that:

(1) I am the sole author/writer of this Work;
(2) This Work is original;
(3) Any use of any work in which copyright exists was done by way of fair dealing and for permitted purposes and any excerpt or extract from, or reference to or reproduction of any copyright work has been disclosed expressly and sufficiently and the title of the Work and its authorship have been acknowledged in this Work;
(4) I do not have any actual knowledge nor do I ought reasonably to know that the making of this work constitutes an infringement of any copyright work;
(5) I hereby assign all and every rights in the copyright to this Work to the University of Malaya ("UM"), who henceforth shall be owner of the copyright in this Work and that any reproduction or use in any form or by any means whatsoever is prohibited without the written consent of UM having been first had and obtained;
(6) I am fully aware that if in the course of making this Work I have infringed any copyright whether intentionally or otherwise, I may be subject to legal action or any other action as may be determined by UM.

Candidate's Signature Date:

Subscribed and solemnly declared before,

Witness's Signature Date:

Name:

Designation:

# EPITAXIAL GROWTH OF SEMI-POLAR (11-22) GALLIUM NITRIDE FOR PHOTOSENSING APPLICATION

## ABSTRACT

Semi-polar (11-22) gallium nitride (GaN) epilayers have attracted numerous interests in GaN based technology as it possess significant advantages over its polar (c-plane) counterparts such as low to none spontaneous and piezoelectric polarization which is known to impair the device performance. However, growth along semi-polar (11-22) orientation has been known to exhibit numerous defect densities such as dislocations and stacking faults (SFs). In order to acquire high quality semi-polar (11-22) GaN epilayers, various growth optimizations must be employed. In this work, the semi-polar (11-22) GaN epilayers were grown on planar m-plane sapphire substrate with the use of a 2-inch capability horizontal metal organic chemical vapor deposition (MOCVD). This work is divided into three main phases namely phase I, where the optimization of the unintentionally-doped GaN epilayer was conducted with variations of three key parameters which includes the nitridation procedure, the V/III ratio of the Uid-GaN epilayer as well as the insertion and variation of the V/III ratio of the aluminum nitride (AlN) nucleation layer. The V/III ratios of the Uid-GaN were optimized via the variation of the ammonia ($NH_3$) flux from 0.4 to 1.0 standard liter per minute (slm) whilst the V/III ratios of the AlN nucleation layer were conducted through the variation of the aluminum (Al) source, trimethylaluminum (TMA) from 50 to 98.5 standard cubic centimeters (sccm). Upon attaining the desired quality of the subsequent Uid-GaN epilayer, implementation of three in-situ defect reduction technique was conducted in phase II of the work namely, (i) insertion of single $NH_3$ treatment with constant $NH_3$ flux of 1 slm at different duration of 90-360 seconds, (ii) multiple $NH_3$ treatment with $NH_3$ flux of 1 slm and different number of alternations and (iii) inter-multilayers of AlN and GaN with

different pairing numbers from 20-200 pairs prior to the growth of the subsequent Uid-GaN epilayer. The final stage of the work is Phase III where optimization of the final structure of the device is optimized prior to the ultraviolet (UV)-photodetector device performance evaluation. Additional transition layer consists of a thin n-GaN epilayer was grown on the Uid-GaN epilayer of higher and lower qualities prior to a thin Uid-GaN layer was realized for the device structure. Symmetric nickel (Ni) contact electrodes for the metal-semiconductor-metal device structure were further deposited via an electron beam deposition prior to the device performance analysis. The crystal qualities of the epilayers were then analyzed via a high resolution x-ray diffraction (HR-XRD) through a phase analysis, on- and off-axis x-ray rocking curve (XRC) analysis and reciprocal space mapping (RSM). Morphological analysis was conducted via a field emission scanning electron microscope (FESEM) and an atomic force microscope (AFM). Electrical properties were analyzed via Hall-effect measurement and the in depth defect analysis were analyzed via a transmission electron microscope (TEM). The device performance on the other hand was analyzed via a photodetection measurement with the use of Keithley 236 Source Measure Unit equipped with an Oriel (Xenon arc lamp) solar simulator.

**Keywords:** Gallium Nitride, m-plane sapphire, MOCVD, in-situ defect reduction technique, UV-photodetector.

**PERTUMBUHAN EPITAXY SATAH SEPARUH KUTUB (11-22) GALLIUM NITRIDE UNTUK APLIKASI FOTO PENGINDARAAN**

## ABSTRAK

Gallium nitride (GaN) lapisan epitaxy satah separuh kutub (11-22) telah menarik banyak perhatian dalam teknologi berasaskan GaN disebabkan oleh kelebihannya yang dapat melangakui polar (satah-c) seperti medan spontan dan piezoelektrik lebih rendah atau tiada yang mana telah diketahui akan merosotkan prestasi peranti. Akan tetapi, pertumbuhan di sepanjang satah separuh kutub (11-22) telah deketahui mempunyai bilangan kecacatan seperti dislokasi dan kesalahan penyusunan yang teramat banyak. Untuk mendapatkan lapisan epitaxy bersatah separuh kutub (11-22) yang berkualiti tinggi, pelbagai pengoptimuman ketika pertumbuhan perlu dilaksanakan. Di dalam kerja ini, pertumbuhan lapisan epitaxy bersatah separuh kutub (11-22) dilakukan di atas substrat nilam bersatah-m melalui pemendapan wap kimia logam-organik (MOCVD) dengan kemampuan 2-inci. Kerja ini terbahagi kepada tiga fasa utama, iaitu fasa I yang mana pengoptimuman lapisan epitaxy suntikan tidak sengaja-gallium nitride (Uid-GaN) melalui tiga variasi termasuk prosidur nitridasi, nisbah V/III lapisan epitaxy Uid-GaN dan juga sisipan dan variasi nisbah V/III lapisan nukliasi aluminium nitride (AlN). Nisbah V/III Uid-GaN telah dioptimasi melalui variasi ammonia ($NH_3$) fluks dari 0.4 hingga 1 standard liter per minit (slm) manakala nisbah V/III AlN lapisan nukliasi pula dilaksanakan melalui variasi sumber aluminium (Al) iaitu trimethyaluminium (TMA) dari 50 hingga 98.5 sentimeter padu per minit (sccm). Setelah mencapai kualiti lapisan epitaxy Uid-GaN yang diingini, implementasi tiga jenis teknik pengurangan kecacatan secara in-situ telah dilaksanakan dalam fasa II di dalam kerja ini, yakni (i) sisipan rawatan $NH_3$ secara tunggal dengan fluks $NH_3$ yang sama iaitu 1 slm dengan variasi masa rawatan dari 90-360 saat, (ii) sisipan berselang-seli rawatan $NH_3$ dengan fluks 1 slm dan variasi nombor alterasi dari 20 hingga 60 alterasi, dan (iii) alterasi antara AlN dan GaN sebagai lapisan pelbagai dengan variasi nombor alterasi dari 20 hingga 200 pasangan sebelum pertumbuhan lapisan epitaxy Uid-GaN. Fasa terakhir di dalam kerja ini merangkumi pengoptimuman struktur akhir peranti sebelum analisa prestasi peranti ultraviolet (UV)-fotodetektor. Penambahan lapisan transit yang merangkumi lapisan nipis epitaxy n-GaN telah ditumbuhkan di atas lapisan epitaxy Uid-GaN yang mempunyai kualiti tinggi dan rendah sebelum penambahan lapisan nipis epitaxy Uid-GaN bagi struktur penuh peranti. Nikel (Ni) contak elektrod secara simetrik bagi struktur peranti logam-semikonduktor-logam telah didepositkan melalui sinar elektron sebelum analisa peranti dilakukan. Kualiti kristal lapisan-lapisan epitaxy telah dianalisa melalui difraksi sinar-x beresolusi tinggi (HR-XRD) termasuk analisa fasa, on- dan off-axis keluk ayunan sinar-x (XRC) dan pemetaan ruang timbal balik (RSM). Analisa morfologi telah dilakukan melalui pelepasan lapangan elektron mikroskop (FESEM) dan mikroskopi daya atom (AFM). Analisa sifat elektrik dilakukan melalui pengesanan Hall-effect dan analisa yang lebih mendalam mengenai kecacatan kristal dilakukan melalui transmisi elektron mikroskopi (TEM). Prestasi peranti pula dianalisa melalui pengukuran fotodeteksi Keithley 236 Source Measure Unit yang dilengkapi Oriel (lampu lengkok Xenon) solar simulator.

**Kata Kunci:** Gallium nitride, satah-m nilam, MOCVD, teknik pengurangan kecacatan secara in-situ, UV-fotodetektor.

## ACKNOWLEDGEMENTS

First and foremost, all praise to God Almighty for giving me the strength and courage to partake my doctorate studies. With His help and blessings, I have managed to complete my research, especially during this dire time of the COVID-19 pandemic.

I would like to extend my sincerest thanks to University of Malaya along with my supervisor Dr Azzuliani binti Supangat for her endless support, morally and physically guiding me during the whole duration of my doctorate studies. Her motivation and teachings have lifted me in numerous occasions for completing this thesis. I would also like to thank my second supervisor, Dr Ahmad Shuhaimi bin Abu Bakar for the opportunity for me to conduct my studies in his advanced epitaxial laboratory in University of Malaya. Without both of my supervisors help and guidance, I would not have been able to complete my research and finish my studies.

Special thanks to my beloved parents, Ahmad Makinudin bin Dahlan and Noor Marina binti Baharom for their unconditional love to me and encouraging me to further my studies to the higher level ever since. Needless to say, their love and support is and always will have a special place in my heart for I am who I am today is because of them.

My deepest thanks to my lovely wife Sara Hasny binti Hassim for standing by me throughout the duration of our marriage whilst always encouraging me to better myself in all aspects of my life. Her endless encouragement has fueled me to finish my doctorate studies.

I would also like to express my gratitude to my close friend Omar Al-Zuhairi for his help and teachings during my studies. His support has managed to aid me in acquiring the skills and knowledge in the field of epitaxial growth for which I am very grateful for.

My sincerest thanks also to my colleagues in the Low Dimensional Material Research Center, for which have helped me during my studies in any way possible.

Last but not least, I would like to thank OSRAM Opto-Semiconductor for their sponsorship for which their financial support has crucially supported me during my whole study.

# TABLE OF CONTENTS

## LIST OF FIGURES

## LIST OF TABLES

## LIST OF SYMBOLS AND ABBREVIATIONS

| | | |
|---|---|---|
| $N$ | : | Charge density |
| $\Sigma$ | : | Conductivity |
| $J$ | : | Current density |
| $V$ | : | Drift velocity |
| $X$ | : | Electron affinity |
| $Q$ | : | Elementary charge carrier |
| $\boldsymbol{\tau_f}$ | : | Fall time |
| $G$ | : | Gain |
| $R_H$ | : | Hall coefficient |
| $V_H$ | : | Hall voltage |
| $P_{opt}$ | : | Incident light power |
| $\Phi_M$ | : | Metal work function |
| $M$ | : | Mobility |
| $I_{ph}$ | : | Photocurrent |
| $\Phi$ | : | Photon flux |
| $P^{pz}$ | : | Piezoelectric polarization |
| $h$ | : | Planck's constant |
| $\eta$ | : | Quantum efficiency |
| $R_i$ | : | Response coefficient |
| $\boldsymbol{\tau_r}$ | : | Rise time |
| $C$ | : | Speed of light |
| $P^{sp}$ | : | Spontaneous polarization |
| AlN | : | Aluminum nitride |
| Au | : | Gold |

| | | |
|---|---|---|
| BSE | : | Back scattered electron |
| BSF | : | Basal stacking faults |
| DFM | : | Dynamic force mode |
| ELOG | : | Epitaxial lateral overgrowth |
| FPD | : | Frank-Shockley partial dislocation |
| GaN | : | Gallium nitride |
| HVPE | : | Hydride vapor phase epitaxy |
| InN | : | Indium nitride |
| LD | : | Laser diode |
| LED | : | Light emitting diode |
| MBE | : | Molecular beam epitaxy |
| MD | : | Misfit dislocation |
| MFC | : | Mass flow controller |
| MO | : | Metal organic |
| MOCVD | : | Metal organic chemical vapor deposition |
| MSM | : | Metal-semiconductor-metal |
| Ni | : | Nickel |
| PLC | : | Programmable logic controller |
| PR | : | Photoresist |
| PSF | : | Prismatic stacking faults |
| RLP | : | Reciprocal lattice point |
| RMS | : | Root mean square |
| RSM | : | Reciprocal space mapping |
| SCR | : | Space charge region |
| $Si_2H_6$ | : | Disilane |
| SiN | : | Silicon nitride |

| | | |
|---|---|---|
| TD | : | Threading dislocation |
| TMG | : | Trimethylaluminum |
| TMG | : | Trimethylgallium |
| UV | : | Ultraviolet |
| VFET | : | Vertical field effect transistor |
| WZ | : | Wurtzite |
| XRC | : | X-ray rocking curve |
| ZB | : | Zinc-blende |

# CHAPTER 1: INTRODUCTION

## 1.1 Brief Introduction of Gallium Nitride (GaN)

Compound semiconducting materials have been the lead materials for various technological advancements. These include the group III-V compound materials such as the binary (Ga, Al, and InN), and its respective ternary and quaternary alloys. The III-V materials fall within the class of direct bandgap semiconductors with broad potential applications in semiconductor optoelectronics. Their energy bandgaps has the capability to cover a large spectral region including the visible-ultraviolet (0.64 - 6.20 eV) region which have been highly unlikely for other conventional semiconductors (Maruska & Tietjen, 1969; Ponce & Bour, 1997). For the last few decades, III-V materials have been extensively exploited in the field of light emitting diodes (LEDs) (Nakamura et al., 1995) and laser diodes (LDs) (Nakamura, 1996) as well as photodiodes (UV-infrared region) (Walker et al., 1999). The revolutionary discoveries of such applications have transcended the technological usage to a far more superior capability for human life experience. Smart electronic developments have shown its mark which allows remarkable ease in human daily tasks. Such wide range applications include general lightings (automotive, housings agricultures), military applications (satellite transmitters, secure light communications, early missile detection systems), environmental protection (water purification, fire detection, ozone breach) and etc.

Since the discovery of the wurtzite structured gallium nitride in the early 1970s, attentions have grown exponentially in exploiting its remarkable properties mainly in LEDs (Ponce & Bour, 1997). Only in the late 1990s, few people looked upon the potentials of GaN and its related binary and ternary compounds in other optoelectronic applications such as photosensing applications (Walker et al., 1999). As the breakthrough in efficient energy saving blue LEDs in 1990s (Nakamura et al., 2000; Nakamura et al., 1995), numerous attentions have been paid towards the LEDs application rather than its photosensing applications. Only few researchers reported on the uses of GaN and its cousins in the field of photosensors (Walker et al., 1999) and even then, the device performance is somewhat lacking behind as compared with the advancements done in the field of LEDs. Henceforth, various developments in enhancing the device performance of GaN-based photosensors have been conducted.

Within the range of GaN-based photosensing applications, great interest have been escalating in the UV region of the spectrum. This is mainly due to the realization of the impact of UV emissions on human life experience. This includes medical awareness with regards to cancer implications presumed to be directly correlated to overexposure of UV emissions from the sunlight (Diffey, 2002; Huang et al., 2017). In order to evaluate such presumptions, development of efficient UV-photodetectors is deemed significant. Other than that, numerous developments in military hardware such as long range missiles have also attracted interests towards UV-photosensors as the missile plumes would also exert UV emissions. Furthermore, acquiring highly efficient yet robust UV-photodetectors for early flame detection systems in extreme environments such as the forests have also been conducted (Hirano et al., 2001). Since GaN and its binary/ternary cousins offers an unlimited range of wavelength emission/absorption as well as its superior physical and chemical properties, numerous interests have grown in developing highly efficient UV-photodetectors with the use of various growth techniques. Amongst them, metal-organic chemical vapor deposition (MOCVD), molecular beam epitaxy (MBE), and hydride vapor phase epitaxy (HVPE) have been the key foundations for the growth of the III-V material (Matsumoto et al., 2008; Nakamura et al., 1991; Nasser et al., 2001; Rahman & Hasan, 2016).

Furthermore, the current state of the art GaN-based optoelectronics are commonly grown along the c-plane orientation (Hwang et al., 2014; Saito et al., 2013). It is known the growth along such orientations exhibit a strong spontaneous and piezoelectric polarizations which hinders the device performance (Tsai et al., 2009). Such polarizations are known to limit the accessible wavelength emissions/absorptions of GaN-based optoelectronics (Tsai et al., 2009). This includes another photodetection design, the photovoltaic device applications where in order to access the whole visible spectrum, higher indium (In) content is required which significantly reduces the device performance. This is owing to the higher polarization fields inducing a resulting photovoltaic IV with a poor fill factor (Dahal et al., 2009).

These limitations have been addressed by many via implementing the growth of polarization-free/low GaN-oriented materials such as the non-polar planes or semi-polar planes (Chakraborty, Haskell, et al., 2005). However, the growth of GaN along such planes have raised yet another issue which includes acquiring an acceptable crystal quality of the epilayers. Additionally, GaN-based materials have been grown commercially on a relatively large lattice mismatched substrate such as sapphires. Regardless of the targeted plane of orientation, growth of GaN on sapphire would exhibit numerous defect existence, mainly due to the 16% lattice mismatch between the GaN epilayer and the sapphire substrates (Akasaki, Amano, Koide, Hiramatsu, & Sawaki, 1989). Even though homoepitaxial growth of GaN have shown impressive device performance (Chakraborty et al., 2005; Funato et al., 2006; Xie et al., 2011; Yamamoto et al., 2010), the production rate is highly cost ineffective. Consequently, the growth of GaN on sapphire is still highly favorable by many inclusive of various defect reduction techniques. This include the use of patterned sapphire substrates (PSS) wherein significantly better crystal quality can be realized (Alhassan et al., 2016; Jiang et al., 2015).

In non-polar and semi-polar oriented planes, the use of PSS was seen quite successful. However, the construction of the PSS was quite complicated for other plane of orientation as compared with c-plane PSS. This includes various etching and masking steps to be implemented with careful control over the patterning process. The repeatability of the process is also questionable as various factors would contribute towards acquiring the same patterning conditions. Since the non- and semi-polar planes offers better device performance if an enhanced crystal epilayer is realized, numerous studies have developed various methods in achieving such goals (Johnston et al., 2009; Jung et al., 2013).

In addition, several groups have presented the potential capabilities of non-polar (10-10) and (11-20) GaN in the field of UV-sensing applications (Ghosh et al., 2007; Gundimeda et al., 2017; Wang et al., 2018). The polarization-free non-polar GaN-based UV-photodetectors have exhibited significantly enhanced device performance including low dark currents as well as fast response towards UV illuminations (Gundimeda et al., 2017). Gosh et al. have reported a narrow-band absorption in the UV region of non-polar GaN based UV-photodetector via a customized configuration (Ghosh et al., 2007). However so, only few studies have developed a semi-polar oriented GaN-based UV-photodetector. Even then, such device exhibited poor performance as compared with the non-polar GaN-based devices which is mainly attributed towards the significantly poor crystal quality which will be further discussed in the next chapter. This opens an opportunity in discovering the potential application of semi-polar GaN-based UV-photodetector for enhanced device performance.

## 1.2 Motivation and Aim

Since numerous studies have shown the potential of non-polar oriented GaN based UV-photodetectors, it is only fair that semi-polar (11-22) GaN to be exploited in the same purpose as both planes have exhibited remarkable properties in other device applications such LEDs and LDs. Furthermore, both non- and semi-polar planes share similar behavior when it comes to its respective challenges for enhanced device performance. This includes the high defects densities generated within the resulting epilayers specifically the basal stacking faults (BSFs). Such high densities of defects would lead to the degradation of the device performance. Hence, tackling the poor crystallinity exhibited by semi-polar (11-22) GaN would surely enable compatible integration for an enhanced UV-photodetector as shown by the non-polar GaN. Therefore, the aim of this work is to articulate the relationship between the growth conditions (during the epitaxial growth) and its respective device performance.

The three main objectives of the study include:

1. To determine the optimal growth conditions of semi-polar (11-22) GaN via implementing 1-step and 2-step growth parameters.
2. To enhance the crystallinity and morphological properties of the semi-polar (11-22) GaN epilayers via implementing various in-situ defect reduction techniques.
3. To integrate the acquired enhanced semi-polar (11-22) GaN epilayer in a metal-semiconductor-metal (MSM) UV-photosensing application for device performance evaluation.

## 1.3 Thesis Organization

The thesis is divided into 7 main chapters which comprises of a brief introduction to the compound group III-V semiconductors, challenges and motivations in Chapter 1. Chapter 2 discusses the main properties of the materials as well as the advantages of different orientation of GaN (specifically semi-polar (11-22) GaN). Then, the key challenges of the growth in semi-polar (11-22) GaN are addressed and methods of overcoming such issues are presented. The details of the experimental procedures and characterization methods as well as a brief discussion of the related equipment utilized in this study are elaborated in Chapter 3. Chapter 4 discusses the findings of the first phase of the work including the nitridation procedure, the 1-step growth of single crystal semi-polar (11-22) GaN epilayer, as well as the 2-step growth for better crystal and surface. In, Chapter 5, a detailed discussion on the phase II of the work where implementing three dissimilar defect reduction techniques is presented. This includes the single ammonia ($NH_3$) treatment with various duration prior to the growth of the thick Uid-GaN epilayer. Subsequently the multiple ammonia ($NH_3$) treatment is further discussed prior to the inter-multilayer insertion. Furthermore, upon complete analysis of the pre-optimized samples, a detailed discussion on the integration of the semi-polar (11-22) GaN into the MSM UV-photodetector is presented in Chapter 6. Finally, the comparison between the device performance as a result of dissimilar crystal and morphological qualities are elaborated. Further concluding the work is as presented in Chapter 7.

# CHAPTER 2: LITERATURE REVIEW

The group III-V nitride materials are considered one of the most significant compound semiconducting material after silicon. They have been developed extensively for lighting applications due to its remarkable properties. It is imperative that such remarkable properties be understood for further applicability in other devices. In this chapter, the fundamental properties of GaN and its binary cousins are briefly discussed and its potential use for UV-photo detection is highlighted.

## 2.1 GaN Properties

Group III-nitride semiconductors falls under the classifications of a direct bandgap semiconducting material wherein the minimum energy in the conduction band have the same momentum as the maximum energy in the valance band (Fujita, 2013). GaN and its binary, ternary, quaternary cousins have shown great potential in light emitting diodes since the 1960s due to its wide bandgap allowing a broad spectrum coverage from 0.7 eV (InN), to 3.4 eV(GaN) and 6.2eV (AlN) igniting its potential for optical devices which are active within the red-ultraviolet wavelength range (Maruska & Tietjen, 1969). The bandgaps of the III-V nitrides with respect to its commonly used substrates as well as other conventional semiconductors are depicted in Figure 2.1 (Morkoç, 2009). Unlike the group III-V nitrides, the conventional II-VI compounds, III-Arsenides and III-Phosphides possess significant limitations, such as only long wavelength emission for III Arsenides or short wavelength for II-VI compounds (Rössler, 1969; Shen & Kwok, 1994). The group III-nitrides however can be manipulated via formation of its ternary compounds to efficiently emit or absorb longer range of the spectrum (Hashimoto et al., 2014; Sheu et al., 2016; Shioda et al., 2012).

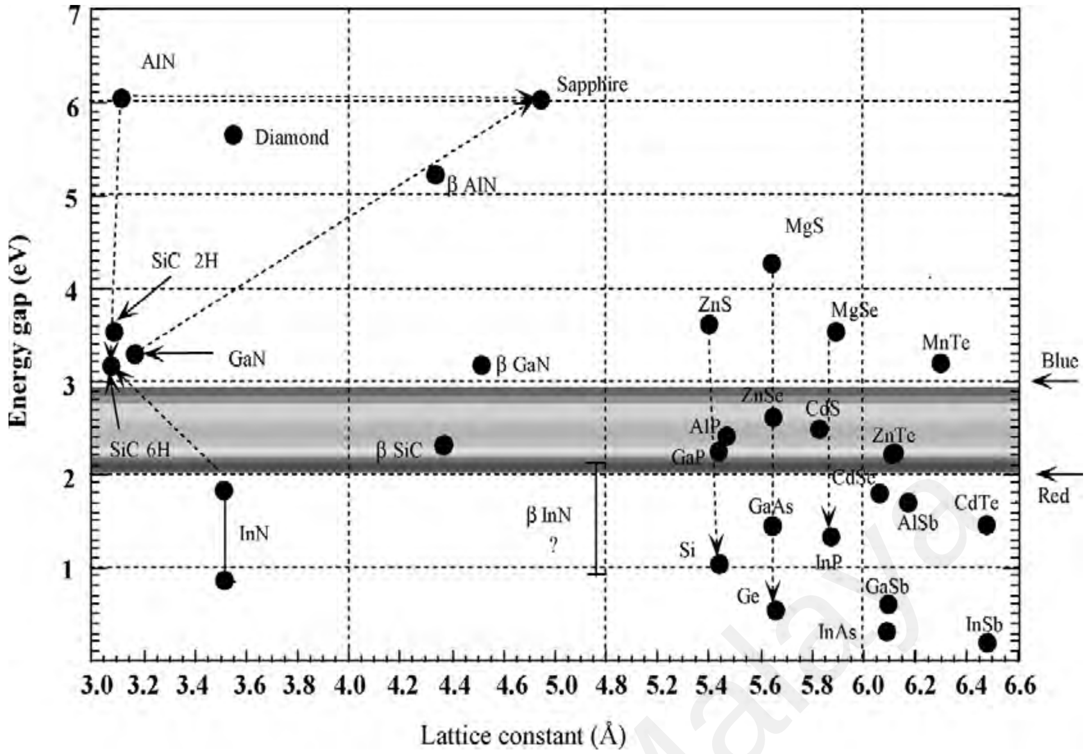


**Figure 2.1: An energy bandgap spectrum of the group III-nitrides compound material as compared with other compound semiconductor materials with respect to their lattice constants (Morkoç, 2009).**

GaN and other III-V semiconductors crystallizes into three structures, namely the wurtzite (WZ), zinc-blende (ZB) (or also known as cubic phase) and rock salt (Maruska & Tietjen, 1969; Morkoç, 2009; Scholz & Thiemann, 1977; Xia & Ruoff, 1993). The most thermodynamically stable commonly existing structure of GaN and other III-nitrides is the WZ structure. The ZB and rock salt structures are unstable where the ZB is metastable whilst the rock salt would only stabilize under high pressure (Morkoç, 2009; Paisley et al., 1989; Strite et al., 1991). The WZ structure has a hexagonal unit cell with two lattice constants, *a* and *c* which consists of two interpenetrating hexagonal closely-packed (hcp) sublattice with one type of atom each (Lähnemann et al., 2014; Morkoç, 2009). The lattice constants of GaN as well as its binary cousins are tabulated in Table 2.1.

**Table 2.1: The lattice parameters of the main three III-nitrides materials, AlN, GaN, and InN (Leszczynski et al., 1996; Scholz & Thiemann, 1977).**

| Lattice Constant | AlN | GaN | InN |
|---|---|---|---|
| ***a*** **(Å)** | 3.111 | 3.189 | 3.544 |
| ***c*** **(Å)** | 4.978 | 5.185 | 5.718 |
| ***u*** **(Å)** | 0.382 | 0.382 | 0.379 |

Each group-III atom is coordinated by four nitrogen atoms and each nitrogen atom is coordinated by four group-III atoms. The stacking sequence of the (0001) plane would be AaBbAa in the [0001] direction due to the alternating biatomic close-packed (0001) planes of the Ga and N pairs (Gil, 2014; Morkoç, 2009). Additionally, the WZ structures of III-nitrides lack an inversion plane perpendicular to the c-axis resulting in the surface polarity being either Ga polarity (referring to the group III element Al, Ga, and In) or N-polarity as depicted in Figure 2.2. Such property will implicate the polarization charge polarity in nitride compounds.

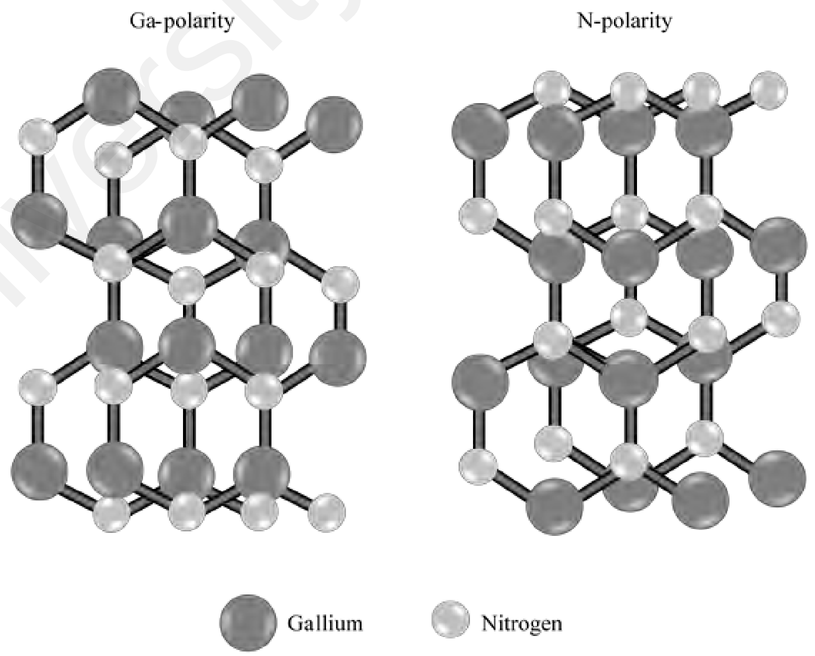


**Figure 2.2: Stick-and-ball representation of the different polarity governed by GaN and its binary cousins.**

Four indices (miller-Bravais indices) designated as h,k,i and l (hkil) would be used to identify the crystal planes in the hexagonal unit cell in conjunction with the axes of the coordinate systems ($a_1$, $a_2$, $a_3$, and C) as depicted in Figure 2.3. The crystallographic directions on the other hand, are designated by four indices [*uvtw*], where $a_1$, $a_2$, $a_3$, and C are the corresponding lattice vectors for *u*, *v*, *t*, and *w*, respectively. From the Figure 2.3, 3 dissimilar crystal planes can be derived from the main (0001) basal plane of the WZ structure, namely non-polar (either (10-10) or (11-20)) and semi-polar (with various tilt angle respect to the (0001) plane). Each crystal planes possess different advantages over the other. In GaN such dissimilar crystal planes possess different advantages such as doping capability, polarization effects, and light emission/absorption capability (Das et al., 2010; Y. Zhao et al., 2012). For example, due to the angle between the non-polar plane and polar plane of 90°, the net polarization field becomes zero upon realizing the growth on such planes.

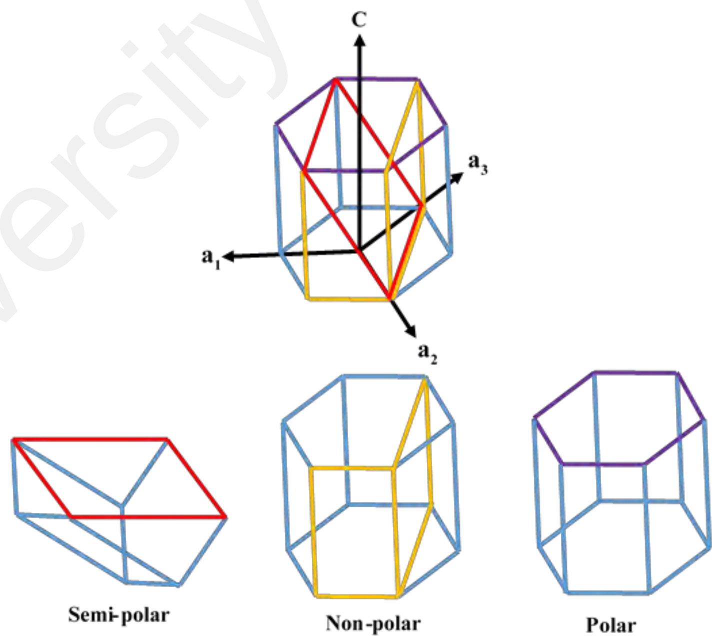


**Figure 2.3: Schematic diagram of the different orientations of III-V materials.**

## 2.2 Semi-polar GaN

Within the various planes of GaN, semi-polar (11-22) plane offers a significant advantage over its polar (c-plane) counterpart. Amongst them, semi-polar (11-22) oriented GaN offers low piezoelectric polarization with higher doping capabilities when the growth of the ternary alloy is required (Das et al., 2010; Mierry et al., 2009; Funato et al., 2006; Northrup, 2009). In most optoelectronic applications, such properties are highly desired as to enhance the spectral coverage as well as the device efficiency. As reported in numerous publications, the critical polarizations effect presents in the c-plane oriented GaN films have shown hindrance in the device performance including LEDs and UV-photodetectors (Das et al., 2010; Ghosh et al., 2007; Gundimeda et al., 2017; Zhao et al., 2018). Such effects originate from the spontaneous polarization ($P^{sp}$) due to the non-symmetric WZ structure along the c-plane GaN and the strain induced piezoelectric polarization ($P^{pz}$) (Bernardini et al., 1997; Romanov et al., 2006; Zhao et al., 2014). Semi-polar and non-polar oriented GaN however, offers a reduction to low or none of such polarization effects. The polarization change is determine from (Romanov et al., 2006) as:

$$\Delta P_{Z\prime} = P_{LZ'}^{PZ} + (P_{L}^{SP} - P_{LT}^{SP})cos\vartheta \tag{2.1}$$

Where the spontaneous polarization for the layer is $P_{L}^{SP}$, $P_{LT}^{SP}$ is the spontaneous polarization for the template and $P_{LZ'}^{PZ}$ is the piezoelectric polarization. The higher tilt angle with respect to the c-plane would correspond to lower polarization effect. This ignites the fact that the III-nitrides grown along both non- and semi-polar orientation would allow the full potential of the III-nitrides to be exploited. Despite that, non-polar III-nitrides have been extensively studied within the field of LEDs, LDs and photodetectors with somewhat remarkable properties (Chakraborty et al., 2005; Gundimeda et al., 2017; Onuma et al., 2008). However, such achievement relies highly on the quality of the crystal growth. Semi-polar III-nitrides on the other hand, even though numerous studies have reported on its uses in the field of LEDs and LDs with remarkable device efficiency (Funato et al., 2006; Sizov et al., 2009), their uses in photodetection application have yet seen much advancements. Furthermore, similar to non-polar III-nitrides, their device performance relies highly on the crystal growth quality wherein mostly, the devices were fabricated on high quality semi-polar GaN templates (Funato et al., 2006).

Semi-polar orientations are (*hkil*) planes with a nonzero *h* or *k* and *l* indices where the plane $hkl$ is perpendicular to the vector (*h,k,l*) in the reciprocal lattice of the WZ nitride structure. In general, semi-polar planes diagonally extend crosswise forming an angle relative to the c-plane other than 90° (Baker et al., 2006). The angle between the surface normal vectors of the (0001) plane and the semi-polar plane can be defined as $\theta$ (Gil, 2014):

$$\theta = \arccos(\frac{\sqrt{3}al}{\sqrt{4c^2(h^2+k^2+hk+3a^2l^2}}) \qquad (2.2)$$

The various semi-polar orientation with respect to its tilt angle is as tabulated in Table 2.2. Studies have shown, that the growth of the various semi-polar planes can be achieved on different types of substrates with different growth conditions (Saito et al., 2008). For example, the growth of semi-polar (11-22) and (10-13) GaN can achieved on planar m-plane sapphire with different growth temperature or pressure (Frentrup et al., 2011).

**Table 2.2: The various semi-polar orientations achievable with their respective tilt angles.**

| Semi-polar (Planes) | Tilt angle $\theta$ (°) |
|---|---|
| (10-13) | 32 |
| (10-12) | 43 |
| (11-22) | 58 |
| (10-11) | 62 |
| (20-21) | 75 |
| (20-2-1) | 105 |

Numerous studies have shown the use of various semi-polar orientation on dissimilar device application with vast potential (Chakraborty et al., 2005; Li et al., 2017; Sharma et al., 2005). Enhanced green semi-polar (10-13) InGaN/GaN LEDs were demonstrated with low turn-on voltage due to the reduced polarization fields (Sharma et al., 2005). Blue InGaN/GaN LEDs grown along (10-11) and (10-13) semi-polar GaN templates have also shown remarkable advancements in the recent years (Chakraborty et al., 2005). In addition, high efficiency semi-polar (11-22) Yellow/Green InGaN based LED have also been developed with low efficiency droop as well as low blue-shift with increasing injection currents (Li et al., 2017). Even so, most device applications of the semi-polar orientations have been drawn towards the LED and LD applications. This is mainly owing to the high indium incorporation capability of semi-polar growth orientation (Northrup, 2009). Few studies have reported on the use of semi-polar GaN in other device applications such as vertical field effect transistors (VFETs), solar cells and UV-photodetector (Bai et al, 2018; Mukundan et al., 2014; Qian et al., 2017). However, such studies have shown the device dependencies on the crystallinity of the epilayers remains a crucial matter for enhanced device performance.



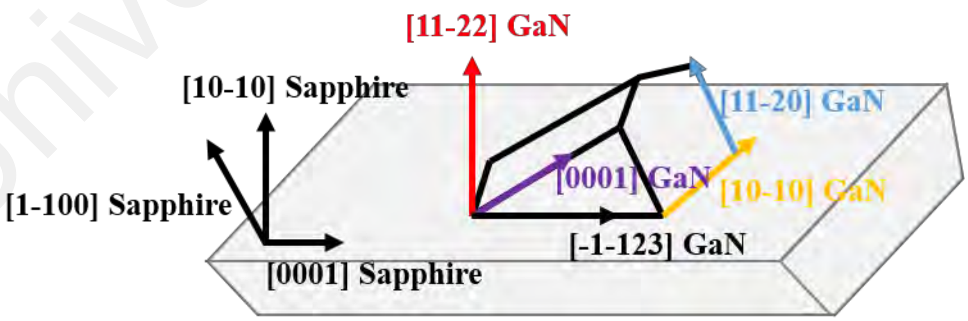


**Figure 2.4: Epitaxial relationship of semi-polar (11-22) GaN grown on m-plane (10-10) sapphire.**

For this study, the main orientation that would be of focus is the semi-polar (11-22) GaN orientation. The most commonly used substrate for the growth of semi-polar (11-22) GaN would be on the inexpensive m-plane sapphire. However, various groups have shown its remarkable crystal enhancement via the use of either bulk GaN substrates (semi-polar oriented) (Funato et al., 2006; Ueda et al., 2006) or on patterned r-plane and m-plane sapphire (Kriouche et al, 2010; Tendille et al., 2016) which will be discussed later in the chapter. However so, the growth of semi-polar (11-22) remains a challenge as the native substrate (bulk semi-polar substrate) still remains scarce and highly expensive. In turn, researchers have turn towards growing semi-polar oriented GaN on inexpensive foreign substrates such as sapphire. The epitaxial relationship of semi-polar (11-22) GaN on m-plane sapphire is depicted in Figure 2.4 (Dasilva et al., 2010; Frentrup et al., 2011; Stellmach et al., 2012) and can be rewritten as follows:

$$[11\text{-}22]_{GaN} \parallel [10\text{-}10]_{sap},\ [1\text{-}100]_{GaN} \parallel [11\text{-}20]_{sap},\ [\text{-}1\text{-}123]_{GaN} \parallel [0001]_{sap} \quad (2.3)$$

Even so, the growth of semi-polar (11-22) GaN on m-plane sapphire requires precise growth conditions as three dissimilar growth orientation can be achieved on planar m-plane sapphire (Mogilatenko et al., 2014; Ploch et al., 2010) which will be discussed later. Furthermore, the growth of semi-polar (11-22) GaN on sapphires have shown tremendous defects generations due to the large lattice mismatch of GaN and sapphire (16%) (Dinh et al., 2015). Defect densities in semi-polar growth have been reported to be significantly higher as compared with its polar c-plane counterparts (Dasilva et al., 2010).

## 2.3 Defects in semi-polar GaN

III-nitride growth on sapphire is no stranger to numerous defects generations. As mentioned before, the main causality for such phenomenon is due to large lattice mismatch between the sapphire and epilayer. In c-plane GaN epitaxy, the predominant defects would be the perfect threading dislocations TDs (Fujita, 2013; Ponce, 1997). Mainly few defect characters would constitute towards the formation of the so-called TDs, namely edge, screw or mixed dislocation with Burgers vector of 1/3⟨11-20⟩, ⟨0001⟩, or 1/3⟨11-23⟩, respectively (Lu et al., 2007; Wu et al., 1996). The formation of such TDs are mainly due to the mosaic growth mode which constitute low/high grain boundaries angles (Ponce, 1997; Potin et al., 2000). Since the growth orientation of c-plane comprises of the (11-20) and (10-10) lattice planes which contains the [0001] growth direction, they provide slip planes for the TDs wherein upon formation, the dislocation would propagate within the epilayers reaching the surface (Dasilva et al., 2010).

Semi-polar GaN (specifically grown on m-plane sapphire) on the other hand, have been known to exhibit numerous various defect generations. Twinned grain growth of semi-polar (10-13) and (11-22) GaN can also be achieved via the growth on planar m-plane sapphire (Dinh et al., 2015; Frentrup et al., 2011; Mogilatenko et al., 2014). Depending on the growth conditions such as temperature, pressure, V/III ratio, and growth steps, achieving the twinned grain growth can be realized (Ploch et al., 2010). However, such growth leads to the formation of polycrystalline oriented epilayer accommodated with numerous defects generations resulting in significantly poor crystal quality and morphology (Frentrup et al., 2011). If avoidance of the twinned grain growth is realized, still the numerous defects generated in semi-polar GaN epilayers surpass the densities reported in polar c-plane GaN.

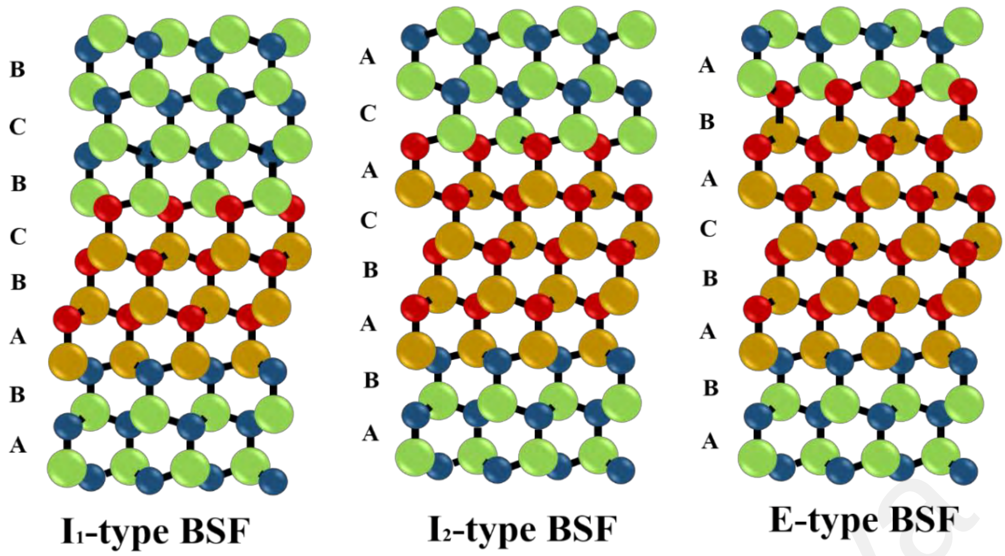


**Figure 2.5: The three dissimilar types of BSFs with its corresponding stacking sequence.**

Furthermore, it is well known that the most dominant exiting defects in semi-polar epilayers would be the basal plane stacking faults (BSFs) (Dasilva et al., 2010; Vennéguès, 2012). BSFs are mainly divided into three types, the intrinsic types ($I_1$ and $I_2$ type) and an extrinsic (E) type BSF (Lähnemann et al., 2014). The prior are resulted from the fault in their stacking sequence where the change of one hcp to another should occur (Stampfl & Walle, 1998) and they differ in the stacking fault sequence as shown in Figure 2.5. The later are mainly resulted from an insertion of an extrinsic layer. To put it simply, $I_1$-type BSF comprises of a violation of the WZ stacking rule, $I_2$ corresponds to two breaches in the WZ stacking sequence and E-type BSFs resulted in three breaches in the WZ stacking sequence. Their respective formation energy also follows the trend wherein higher number of breaches would endure higher formation energy.

Studies have shown that the generation of $I_1$-type BSFs are among the highest densities in semi-polar, and commonly generated between the first epilayer and the sapphire interface (Dasilva et al., 2010; Lähnemann et al., 2014; Vennéguès et al., 2007). A slip in the basal plane during post-growth would however facilitate the formation of the $I_2$-

type BSFs (Frank & Nicholas, 1953; Lähnemann et al., 2014). The E-type BSFs on the other hand would significantly be generated upon the growth of nanostructure such as nanowires (Lähnemann et al., 2014). It is crucial to address the existence of BSFs in semi-polar GaN epilayers as it would perturb its conductivity, giving rise to an anisotropic conductivity due to the carrier scatterings from the BSFs (Baik et al., 2010; Potin et al., 2000; Stampfl & Walle 1998).

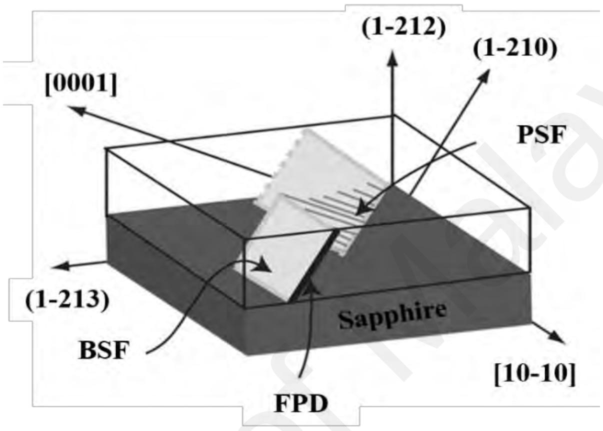


**Figure 2.6: Schematic illustration of planar defects in semi-polar GaN epilayer including basal stacking faults (BSFs), prismatic stacking faults (PSFs) and Frank-Shockley partial dislocation (FPD). Taken from (Dasilva et al., 2010).**

The existence of numerous variant types of BSFs would also constitute dissimilar associated partial dislocations. As tabulated in Table 2.3, the $I_1$-BSFs is always bounded by the Frank-Shockley partial dislocations (FPD) whilst the $I_2$-type BSFs is bounded by the Shockley partial dislocation and the E-type BSFs are bounded by the Frank partial dislocations (Dasilva et al., 2010; Moram et al., 2009). Due the high densities of BSFs type $I_1$ and $I_2$ in semi-polar epilayers, hence the presence of Frank-Shockley and Shockley partial dislocations would be of the highest densities. Few studies have reported that the Frank-Shockley and Shockley partial dislocation would introduce deep gap states which affects the electrical properties of the grown epilayer, resulting in the hindering of the device efficiency (Kioseoglou et al., 2011; Komninou et al., 2005).

**Table 2.3: Stacking faults in hexagonal structure with its displacement vectors, P: prismatic, B: basal plane, and SS: stacking sequence.**

| Stacking Faults | | | |
|---|---|---|---|
| Type | Displacement Vector **R** | SS or plane | Associated dislocation |
| B-$I_1$ | 1/3 ⟨1-100⟩ | AB**ABC**BCB | Shockley partial |
| B-$I_2$ | 1/6 ⟨20-23⟩ | AB**ABCA**CA | Frank-Shockley partial |
| B-E | 1/2 ⟨0001⟩ | AB**ABCAB**AB | Frank-partial |
| P | 1/2 ⟨1-101⟩ | {11-20} | - |
| P | 1/6 ⟨20-23⟩ | {11-20} | - |

In addition, another type of stacking fault can be found in the (11-20) planes, namely the prismatic stacking faults (PSFs) (Drum, 1965). PSFs are known to form within the epilayers during the coalescence of the islands (Komninou et al., 2005). The coexistence of certain interfacial structures near the epitaxial interface would facilitate the formation of PSFs (Stampfl & Walle, 1998). These PSFs can be found to connect two $I_1$-type BSFs and leading to a loop of the SFs (Dasilva et al., 2010; Lähnemann et al., 2014). In addition, the PSFs are also known to fold the $I_1$-BSFs within the slip plane causing a generation of $I_2$-BSFs (Dasilva et al., 2010).

Perfect dislocations of type a, c and a + c on the other hand can also be found within the semi-polar (11-22) GaN epilayers, and since the formation energy of the a-type perfect dislocations is the lowest, it would be the most abundance perfect type dislocation (Dasilva et al., 2010). However, it should be noted that the slip planes [11-20] and [10-10] are away from the growth direction. Consequently, most of a-type perfect dislocation would most probably be forced to dissociate into Shockley partial dislocations. This would then facilitate the generation of $I_2$-type BSFs, henceforth inducing lower density of the perfect dislocation whilst increasing the $I_2$-type BSF densities (Dasilva et al., 2010). The dislocation types and characters are as tabulated in Table 2.4.

**Table 2.4: Types of dislocations in hexagonal structure with their Burger vectors.**

| Dislocations | | |
|---|---|---|
| Characters | Type | Burger Vectors **b** |
| Perfect | a | 1/3 ⟨11-20⟩ |
| Perfect | a + c | 1/3 ⟨11-23⟩ |
| Perfect | c | ⟨0001⟩ |
| Shockley partial | | 1/3 ⟨1-100⟩ |
| Frank-Shockley partial | | 1/6 ⟨20-23⟩ |
| Frank partial | | 1/2 ⟨0001⟩ |

## 2.4 Defects Reduction Techniques

Since the numerous existences of the BSFs along with various other defects were found in the growth of semi-polar (11-22) GaN, several attempts have been conducted in overcoming such issues. This leads to a multitude of defect reduction techniques being employed and categorized under two distinct approach namely, ex-situ and in-situ approach. Even so, both approaches have one common goal, by which the presence of the defect densities within the semi-polar (11-22) GaN epilayer must be lowered.

### 2.4.1 Ex-situ Defects Reduction Techniques

In the ex-situ approach, the growth of the epilayer would be grown on pre-masked templates or growth interruption was introduced and additional process was implemented during which the defect reduction step is included outside the epitaxial process (using other means than the epitaxial process).

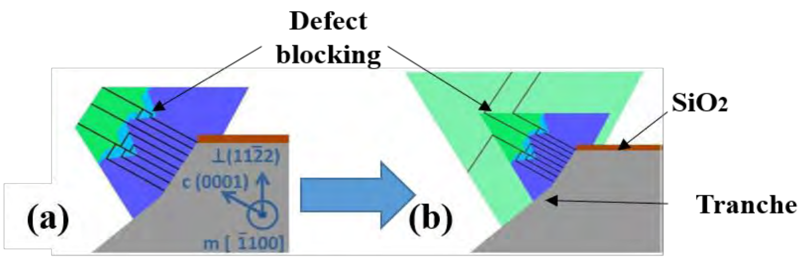


**Figure 2.7: ELOG mechanism on grooved or tranche r-plane sapphire with $SiO_2$ mask (Tendille et al., 2016).**

One of the most distinguished approach among them would be the use of what is known as the epitaxial lateral overgrowth (ELOG) on pre-pattern sapphire substrates (Tendille et al., 2014). The use of dissimilar sapphire oriented substrates such r-plane and m-plane can be realized with this approach (Ni et al., 2007; Tendille et al., 2016). In this technique, two main principles govern the resulting epitaxial growth which depend on the type of substrate used. For r-sapphire, most cases implement either a chemical or dry etching process to form tranches or grooves near the surface of the sapphire (Li et al., 2017; Tendille et al., 2016). In some cases, further deposition of $SiO_2$ mask was implemented to cover most area whilst the c-plane-like facets were being left exposed as shown in Figure 2.7 (Caliebe et al., 2015; Scholz et al., 2014; Schwaiger et al., 2011; Tendile et al., 2016). In m-plane sapphire on the other hand, few hundreds nanometers of $SiO_2$ layer were commonly deposited after the growth of thick GaN epilayer prior to lithographic procedures to construct a $SiO_2$ mask wherein stripes and windows were formed as shown in Figure 2.8(a) (Lacroix et al., 2011; Ni et al., 2007). Some cases have also shown the patterning of the m-plane similar to the r-sapphire conversely without the formation of tranches or grooves, instead, the formation of hemi-spheres-like structures were formed as shown in Figure 2.8(b) (Jang et al., 2012; Min et al., 2013).

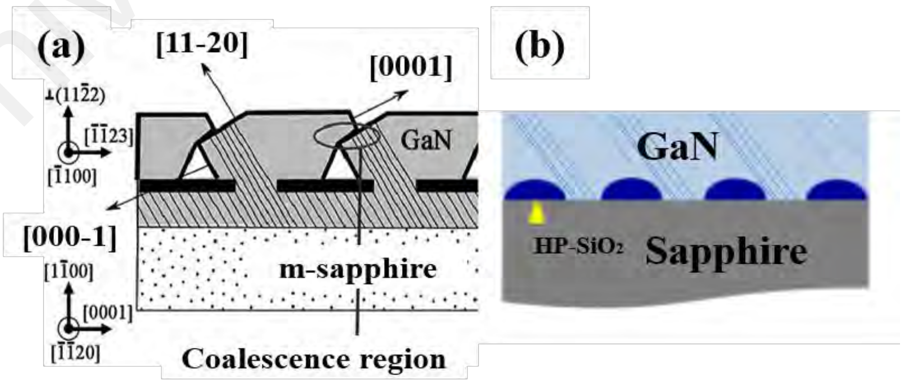


**Figure 2.8: ELOG mechanism for dissimilar maskings of $SiO_2$ on m-plane sapphire, (a) thin $SiO_2$ masks layer with windows (Lacroix et al., 2011)and (b) hemispherical $SiO_2$ masks with windows (Min et al., 2013).**

Generally, the principle governing the ELOG approach on patterned m-plane sapphires utilizes a defect blocking mechanism where the defects (mainly BSFs) propagation were considerably blocked at the mask interface as shown in Figure 2.8 (a-b). Only few defects within the masks window were allowed to propagate through whilst the defects underneath the masked layer will permanently blocked (Kriouche et al., 2010; Zhu et al., 2013). The ELOG approach on grooved r-plane sapphire on the other hand enhances the growth rate along [0001] relative to the [11-20] direction, resulting in the (11-22) semi-polar epilayer with low defect densities wherein the highly defective region were overgrown completely whilst simultaneously blocking and eliminating the dislocations and BSFs at the coalescence boundary (Bougrioua et al., 2007; Zhu et al., 2013). Furthermore, in both cases, controlling the growth window is crucial as to ensure minor allowed defects propagation is achieved without morphological deterioration occurring (Caliebe et al., 2016). Few works have also shown that with the implementation of such approach, the defect densities were significantly reduced, and enhanced device performance was achieved (Jang et al., 2012; Li et al., 2017).

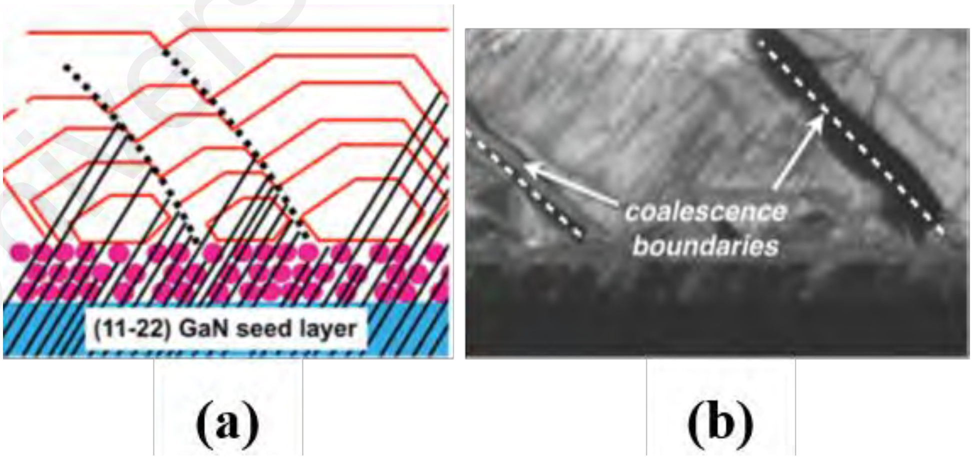


**Figure 2.9: ELOG mechanism involving the use of silica nanospheres (Zhu et al., 2016).**

Another interesting defect reduction technique that is quite similar to the ELOG on patterned sapphire (via sapphire etching or $SiO_2$ masking) is the use of silica nanospheres (Zhu et al., 2016). This approach utilizes a porous nanomasks consisting of self-assembled silica nanospheres near the surface of the substrate, wherein the growth takes place in between the porous layer and further coalescence of the subsequent layer was of enhanced crystal with low defect density (Zhu et al., 2016). Such work was influenced by the demonstration of enhanced a-plane GaN with the use of such techniques whereby numerous defects including dislocations and BSFs were significantly reduced with the use of silica nanospheres interlayer (Park et al., 2012). Zhu et al. implemented multiple silica nanospheres on thin GaN seed layer and observed an enhanced crystal quality epilayer due to the perturbation of the BSFs and dislocations propagations as shown in Figure 2.9.

Despite all the mentioned above, even though the ex-situ process of defect reductions technique enables the achievement of high-quality crystal of semi-polar GaN. However, such approaches require additional ex-situ process which are considered cost ineffective as well as complex and time-consuming process. For instance, in order to acquire the mentioned patterns, etching process must be implemented prior to the growth which includes the use of reactive ion etching (RIE) for dry etching process and potassium hydroxide (KOH) for chemical etching process (Leung et al., 2012; Min et al., 2013; Tendille et al., 2016). Furthermore, the use of additional deposition techniques such as plasma-enhanced chemical vapor deposition (Min et al., 2013; Zhang et al., 2016) or radio frequency (RF) sputtering technique for the $SiO_2$ deposition must also be realized (Kriouche et al., 2010; Scholz et al., 2014). Such complexities have motivated many researchers in developing other means of defect reduction techniques for growth of semi-polar GaN.

### 2.4.2 In-situ Defects Reduction Techniques

As complexity has become a factor, simplicity have arose for the purpose of defect reduction in semi-polar GaN epitaxy. This includes the use of non-complex in-situ process without the use of any additional ex-situ etchings and maskings. In-situ defect reduction approach manly utilizes the epitaxial growth technique within the reactor itself. It can be of various different ways such as introducing porous silicon nitride (SiN) interlayers (Monavarian et al., 2016), indium nitride (InN) island interlayers (Jung et al., 2013), double AlN buffer layers (Zhao et al., 2016), in-situ etchings via ($H_2$ or $NH_3$) (Song et al., 2013), in situ asymmetric island sidewall growth (AISG) (Wu et al., 2017) and insertion of strain layer superlattice (SLs) (Xu et al., 2012).

Such techniques have its advantages and disadvantages where most of the techniques exhibit remarkable properties. In light of that, such in-situ techniques do not require additional complicated deposition or etching methods. They offer a simple flow of certain gas in combination with the organometallics or none with different purposes. When the use of dissimilar growth conditions of the SiN interlayers, island-like or porous structures can be formed (Sakai et al., 2000). Similar to previous ELOG technique, the island or porous structure will allow fewer defects to propagate through to the subsequent epilayer resulting in lower defect densities as shown in Figure 2.10 (Monavarian et al., 2016). Although the defects were remarkably stopped upon reaching the SiN interlayer, regeneration of newly formed defects above the SiN can also be realized which might be resulted from the folding of the BSFs by PSFs (Dasilva et al., 2010). Furthermore, the use of SiN interlayer have also shown to roughen the surface of the subsequent epilayer even though the defects were reduced (Monavarian et al., 2016).

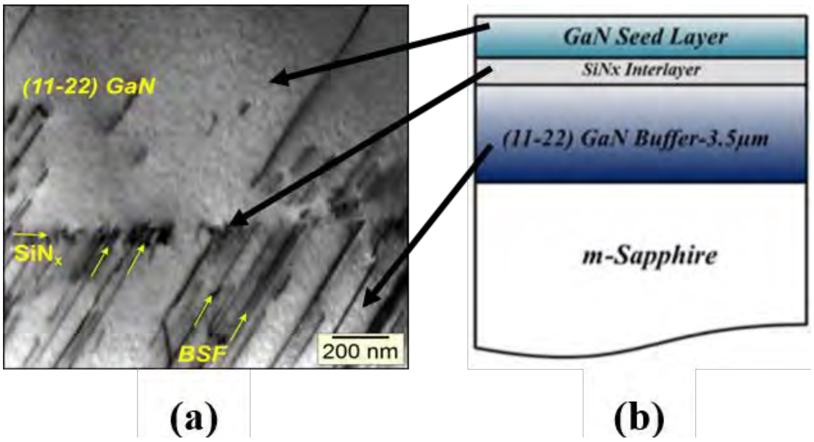


**Figure 2.10: STEM image of SiN nano-network on semi-polar (11-22) GaN buffer layer exhibiting enhanced defect reduction in the subsequent epilayer (a) and (b) the growth structure. Taken from (Monavarian et al., 2016).**

Similarly, the use of InN as interlayers or islands have also showed improved crystal quality as defects such as BSFs were terminated upon reaching the InN/GaN interface which might be resulted from the presence of MDs (Dinh et al., 2012). However, such growth constitutes a highly rough 3D surface structure as shown in Figure 2.11(a) with distance between two protruding peaks as high as 72 nm. Utilizing InN islands on the other hand was presumed to exhibit similar defect blocking mechanism as the SiN nano-network where the defects propagating within the epilayer were terminated upon having contact with the InN islands as shown in Figure 2.11 (a) (Jung et al., 2013). Despite that, the distribution of the InN islands was highly random with variant sizes, as in Figure 2.11 (b). Such property would still allow numerous defects able to propagate through within the subsequent epilayers. The reported surface property was also significantly high with numerous arrowhead-like features and deep elongated valleys which constitutes a root mean square (RMS) roughness of ~8.9 nm (Jung et al., 2013).

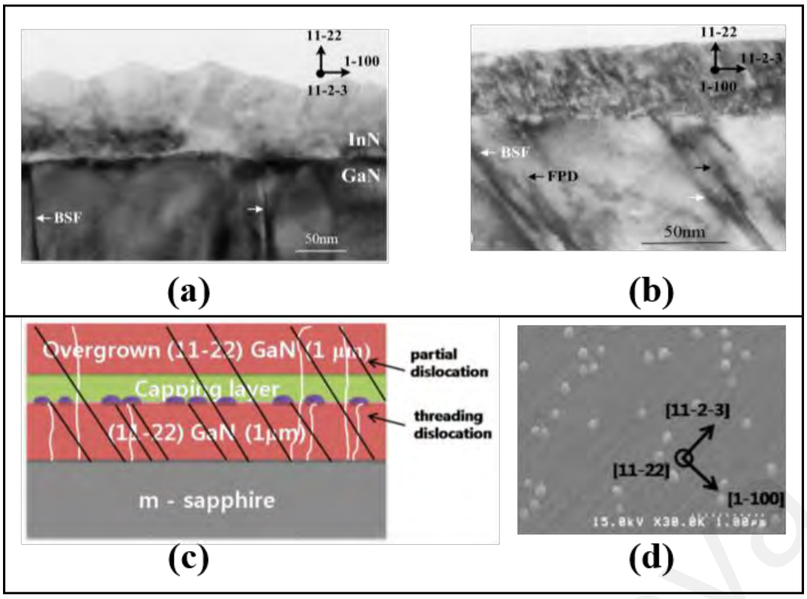


**Figure 2.11: Utilization of InN for defect blocking purposes (a-b) TEM images of InN/GaN interface (Dinh et al., 2012) and (c-d) InN island defect blocking mechanism with surface properties, taken from (Jung et al., 2013).**

The use of double AlN buffer layers on the other hand, depends on the growth conditions of such layer to exhibit sufficient strain in the epilayers to force the dislocations to annihilate each other via a cross-slip between them (Zhao et al., 2016). Other in-situ techniques offer similar defect reduction technique would be the SLs, where the strain difference between the different epilayers would aid in the cross-slip between the dislocations leading to better crystal quality (Xu et al., 2012). The in-situ etching via $H_2$ and $NH_3$ gas however, offers a simpler method wherein the surface of a GaN underlying layer was etched with the presence of optimum flux of $NH_3$ and $H_2$ (Hsu et al., 2011). It was presumed that such technique would aid in the disorientation of the dislocation sites which would result in the enhanced crystal quality (Hsu et al., 2011; Song et al., 2013). From all the mentioned in-situ defect reduction techniques, most of them are currently still undergoing optimizations where the growth condition via the use of such techniques is tuned in various ways to obtain dissimilar outcomes. Such approach has yet reached its maturity as numerous reports have still reported on such matter with higher degree of defect reductions.

### 2.4.3 GaN-based UV-Photodetector

As mentioned in the previous chapter, the utilization of III-nitrides material have shown significant enhancement in device performance of LEDs and LDs, regardless of the defect density, it should be noted their remarkable properties and capability should not be limited. GaN and its ternary cousins have also demonstrated efficient light detecting/harvesting capabilities (Bai et al., 2018; Shen et al., 2017; Zakutayev, 2016). The most interesting topic related to GaN-based photodetector would be related to the UV-photodetection capability. As GaN and its cousin AlN possess a bandgap of (3.4 eV and (6.2 eV), respectively, they possess the capability to absorb light within the whole UV region from UV-A until UV-B and UV-C by realizing the growth of its respective alloys (Velazquez et al., 2016; Zheng et al., 2015). Despite that, various types of photodetectors have been fabricated on GaN and AlGaN for enhanced UV-detection (Lee et al., 2003; Ozbay et al., 2004).

Three main structures for UV-photodetection have been numerously reported via the use of III-nitride materials (GaN and its alloys such as AlGaN), namely the p-n and p-i-n photodiodes (Ozbay et al., 2004; Xu et al., 1997), Schottky barrier (Mou et al., 2017) and MSM photodiodes (Chang et al., 2007; Walker et al., 1999). The general principle governing the mentioned photodetectors would surround the bandgap energy of the epilayer upon photons illumination. As photons (with higher energy than the bandgap) are incident on the material, electron-hole pairs are generated from the absorption. Upon applying an electric field by an external voltage source to the photodetector, the charge carrier would move in a direction towards the electrodes. Consequently, a current is created proportional to the incident photon flux which is called the photocurrent (Decoster & Harari, 2013; Munoz et al., 1997).

The p-n and p-i-n structures are similar in terms of functionality and differs only with the additional intrinsic semiconductor layer between the p and n (Xu et al., 1997). The main obstacles hindering the device performance in such structures are their dependencies on the doping mechanism/concentration of the p-type material which relates to the growth of conditions of the p-type layer (Decoster & Harari, 2013). Additionally, the high resistivity of the associated Ohmic contacts have also contribute towards the device inefficiency (Decoster & Harari, 2013).

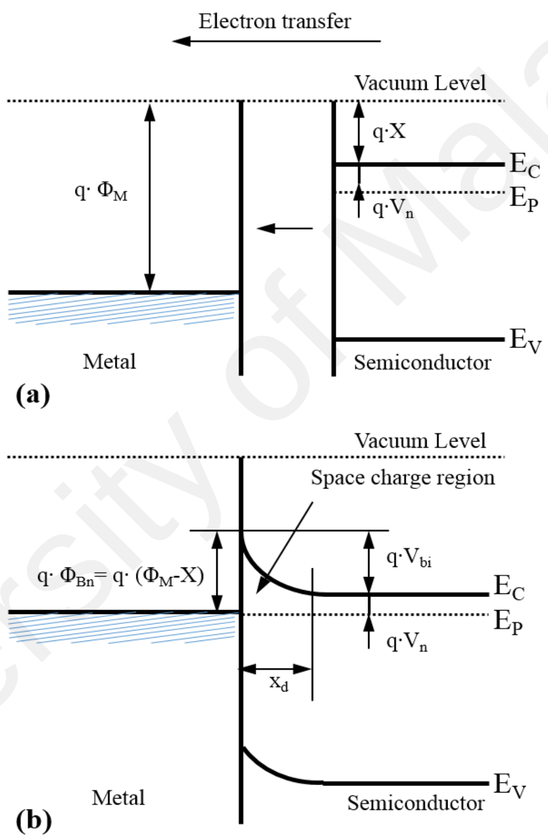


**Figure 2.12: Schottky junction formation upon metal and semiconductor contact.**

The Schottky junction however is formed by bringing a metal and semiconductor material into contact, wherein the work function of the metal ($\Phi_M$) with the elementary charge (q) would be higher than the electron affinity of the semiconductor material (X) (Decoster & Harari, 2013; Kumar et al., 2015). The formation of Schottky barrier is as shown in Figure 2.12. The formation of the space charge region (SCR) at the edge of the semiconductor next to the junction with a width $x_d$ is formed as soon as the metal and semiconductor comes into contact (Guo et al., 2014). An energy band curvature would occur resulting in the existence of the energy barrier (called Schottky barrier, $\Phi_{Bn}$) between the metal and semiconductor. The barrier height is given by:

$$q \cdot \Phi_{Bn} = q \cdot (\Phi_M - \chi) \tag{2.4}$$

An intrinsic electric field is therefore immediately generated next to the metal-semiconductor junction. The photogeneration of charge carriers inside/near the SCR would cause the appearance of the photocurrent wherein separation of the electron-hole pairs would occur (Xie et al., 2011). If an n-type semiconductor material is realized with an applied reverse bias between the metal and semiconductor electrodes, an increase in the barrier height would be attained giving favorable conditions for photodetection (Decoster & Harari, 2013). This would be due to the prevention of charge carriers (electron) being able to flow towards the Schottky contact whilst the minority carriers (holes) generated via the photogeneration would reach the Schottky contact. Two main illumination methods can be chosen within this structure, either front or rear illumination where the front would require a semi-transparent Schottky contact with the metal thickness commonly around 100 Å (10nm) to allow sufficient optical transmission (Su et al., 2005). The latter is often favored as utilization of transparent substrate are commonly observed such as sapphires.

Additionally, in MSM structures, two Schottky electrodes are deposited on a semiconductor material and they are normally interlinked in a form of a comb structure (commonly known as interdigitated structure) as shown in Figure 2.13. Due to this, each contact would exhibit similar to a traditional junction current-voltage (I-V) characteristic. If both the contacts are of the same metal, under bias, a symmetric global I-V characteristic can be realized (Jain et al., 2018; Velazquez et al., 2016).

As sufficient voltage bias is applied, an electric field would be generated due to the depletion of the region between the electrodes. Since certain area of the semiconductors surface are left exposed (no metal contact) between the two contacts allowing light absorption under illumination, electron-hole pairs would be generated. The generated electron-hole pairs would then be subjected to separation under the effects of the electric field by which different types of carriers (electron or holes) would be collected by a different electrodes giving rise to the photocurrent (Mishra et al., 2018). However, since the MSM structure is categorized under a planar structure, and even though it has the capability of collecting carrier over a large area (whilst maintaining short inter electrode distance), its capability in collecting the photogenerated carriers deep within the material is quite low. This is due to the dissimilar electric field distribution from near the contacts and further into the semiconductor material giving rise to specific distribution of carrier transit times (Decoster & Harari, 2013).

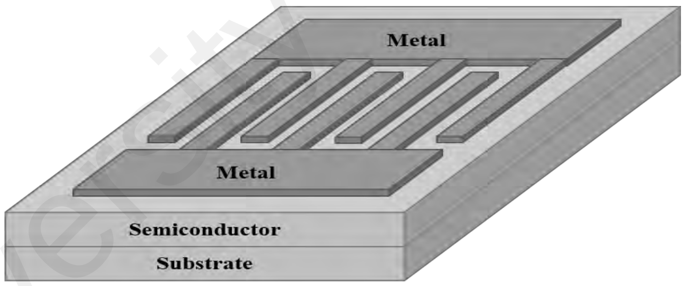


**Figure 2.13: Schematic illustration of a MSM photodetector with an interdigitated structure.**

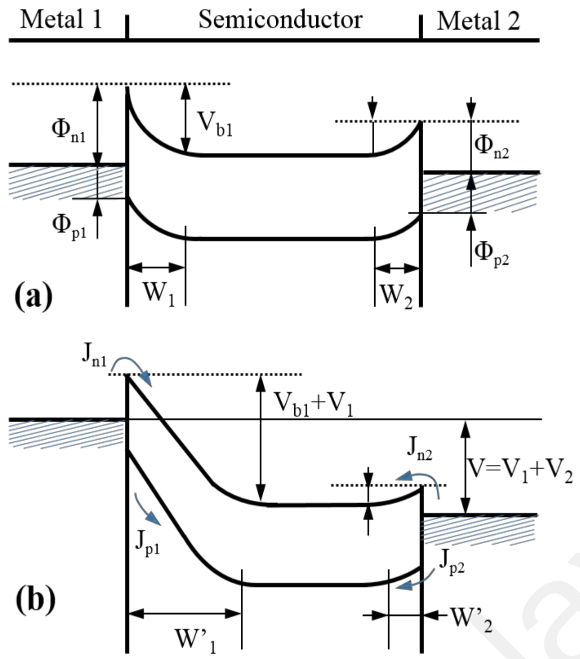


**Figure 2.14: MSM photodetector behavior without illumination (a) in equilibrium and (b) under bias.**

A bias voltage applied between the electrodes would then break the initial electrical symmetry of the contacts as shown in Figure 2.14. This results in a reversed-biased Schottky junction at one end of the electrodes whilst the other being forward biased (Wang et al., 2014). At the reverse-biased junction, the SCR produced is now with increased width ($W'_1$) whilst the forward biased junction shrinks ($W'_2$) (Guo et al., 2014).

The SCRs within the MSM device structure are of significant width which allows the electric field of the junction to easily extend into the semiconductor regions from the contact electrode, enabling the separation of electron-hole pairs to easily occur and collected by its corresponding electrodes (Decoster & Harari, 2013; Mishra et al., 2018). Such occurrence offers significant potential advantages which includes simple fabrications, high speed operations, very low dark currents resulting in low noise-device characteristics (Garrido et al., 1998). Such advantages are mainly owing to the short distance between the contact electrodes allowing the electric field of the junction to easily extend into the semiconductor regions. Within the operation of photodetectors, the few key parameters of concerns are the response coefficient.

The response coefficient (or also known as responsivity) is given by:

$$I_{ph} = R_i \cdot P_{opt} \tag{2.5}$$

Where $I_{ph}$ is the photocurrent, $R_i$ is the response coefficient of the photodetector and $P_{opt}$ is the incident light power. It should be noted that $R_i$ is independent of the photodetector's active optical surface whilst $I_{ph}$ and $P_{opt}$ are dependent on the active optical surface (in an ideal case). Considering the wavelength $\lambda$ of the incident light, the photon flux ($\Phi$), arriving on the active optical surface can be defined as:

$$\Phi = P_{opt} \cdot (\frac{\lambda}{h \cdot c}) \tag{2.6}$$

where $c$ is the speed of light and $h$ is the Planck constant. If the probability of generating an electron-hole pair is taken into account (defined as the quantum efficiency $\eta$), presuming complete absorption of the incident light by the semiconductor material, the rate of electron-hole pair generation per unit time ($G$) can thus be defined by:

$$G = \eta \cdot \Phi = \eta \cdot P_{opt} \cdot (\frac{\lambda}{hc}) \tag{2.7}$$

Further introducing the gain ($g$) which is the number of charge carriers detected in relation to the number of electron-hole pairs generated, then the photocurrent can now be expressed as:

$$I_{ph} = q \cdot G \cdot g = q \cdot \eta \cdot P_{opt} \cdot (\frac{\lambda}{hc}) \cdot g \tag{2.8}$$

$$I_{ph} = (\frac{q \cdot \eta \cdot \lambda \cdot g}{(hc)}) \cdot \ P_{opt} \tag{2.9}$$

Where $q$ is the elementary charge (1.602 x $10^{-19}$ C). The expression of the response coefficient can now be written as:

$$R_i = (\frac{q \cdot \eta \cdot \lambda \cdot g}{(hc)}) \tag{2.10}$$

Furthermore, the cut off frequency ($f_c$) of the photodetector can be defined as half of the response coefficient for a continuous optical signal. The temporal response however, is defined by the fall time ($\tau_f$) which is the time of the photocurrent to fall from 90% to 10% of the maximum and rise time ($\tau_r$) which is the time of the photocurrent to rise from 10% to 90% of the maximum (Decoster & Harari, 2013).

In most cases, the UV-photodetectors are commonly fabricated on GaN grown along the c-plane orientations. However, few significant reports have also demonstrated the use of non-polar (m- or a-plane) GaN and AlGaN orientations for UV-photodetector applications (Ghosh et al., 2007; Gundimeda et al., 2017). It was shown that utilization of non-polar GaN and AlGaN would significantly enhance the device applications as compared with the polar c-plane orientation, mainly owing to the reduced polarization fields as well as the anisotropic in-plane strain exhibited by the non-polar orientations (Ghosh et al., 2007). Furthermore, several studies have also reveal the consequences of high defect densities towards the device performance (Munoz et al., 1997). Visible absorption (below the bandgap response) is modeled to originate from defects localized in lattice discontinuities such as dislocations, grain boundaries, interfaces and etc. (Mishra et al., 2018; Monroy et al., 1999). Although, the semi-polar oriented GaN (as well as its alloys) have yet been extensively reported in its uses for UV-photodetection applications. It was previously reported that the semi-polar oriented GaN would exhibit low device efficiency as compared with the non-polar oriented GaN (Mukundan et al., 2014). However, it can be deduced that the crystal quality exhibited by the semi-polar GaN in such work was considerably low.

Theoretically, the device performance is highly impacted by the crystal quality of the semiconducting layer. Hence in this work, various methods are implemented which mainly focuses on reducing the defects generated within the epilayers to enhance the crystal quality. The integration of semi-polar (11-22) GaN with the MSM structure is further conducted and the impact of the crystal quality towards the device performance is evaluated.

# CHAPTER 3: EXPERIMENTAL PROCEDURE

## 3.1 Growth Technique

Amongst the various growth technique for III-nitride, MOCVD have the advantage over its HVPE and MBE counterparts due to its remarkable growth properties including considerably higher growth rates with potentially flexible uniform growth via selective growth. Even though HVPE systems are known to exhibit the fastest growth rate of III-V materials, recent advancements in MOCVD systems have shown remarkably high growth rates further challenging the advantages of HVPE (Matsumoto et al., 2008; Rahman & Hasan, 2016). MOCVD and MBE shares a common advantage when it comes to epilayer interfaces. If an atomically sharp interface modification is required, then MOCVD and MBE systems are more favored compared with the HVPE where the atomically sharp interfaces are significantly difficult to achieve (Nasser et al., 2001). Despite that, the MBE growth environment usually favors a low temperature growth with significantly lower growth rate as compared with the MOCVD. Furthermore, MBE growth costs are significantly more expensive as compared with the MOCVD igniting the advantage of the MOCVD system.

### 3.1.1 Metal-Organic Chemical Vapor Deposition (MOCVD)

The current state of the art MOCVD system is separated into two systems, the commonly used vertical (showerhead) and lesser favored laminar (horizontal system). Both systems have the similar growth property such as the metal organic (MO) source, the gas precursors and the reaction pathway. However they differ in the direction of the gas delivery system, the showerhead system flows the gas from the top vertically downwards towards the substrate at the bottom whilst the horizontal system utilizes a laminar flow within a gas flow channel (FC) (Nakamura et al., 1991). One of the key advantages of the laminar flow MOCVD system against its vertical flow counterpart, is the capability to grow the epilayers with precise homogeneity and high growth reproducibility.

In this study, a laminar flow MOCVD system (Taiyo Nippon Sanso, SR-2000) was utilized for the growth of the semi-polar (11-22) GaN epilayers prior to the UV photodetector device fabrication. Figure 3.1 depicts the SR-2000 TNSC MOCVD system whereby numerous parts and components works together simultaneously at the edge of technological advancement. Due to that, only few key parameters are highlighted, which constitutes most within the growth conditions. Having said that, each component plays a huge role, in ensuring the operation of the MOCVD system to be in the best condition. Still, extra attention needs to be prioritized towards few components as to ensure the best quality of the epilayers were attained and avoid any additional factors that could impact the growth conditions. In general, the MOCVD is separated into four compartments where the first compartment comprises of the electrical circuits to control most of the components of the MOCVD. A computer is placed here in order to enable the construction of the growth recipe such as the MO flux used, temperature and pressure alterations as well as the growth window (time). The second compartment comprises of the MFCs, MO sources, and valves control panel. Then the reactor compartment attached to a glove box for the main growth and sample handling, respectively. Finally, the pump system and gas manual controls compartment. It should also be noted that the utilization of high purity gases during the growth is crucial as to avoid any contaminations that would affect the resulting purity of the grown epilayers. The use of regen and in-line purifiers is deemed significant to avoid such occurrence. Each gas line was connected through a regen-purifier prior to the inline purifier from the gas sources (high pressure cylinders) before entering the MOCVD system.

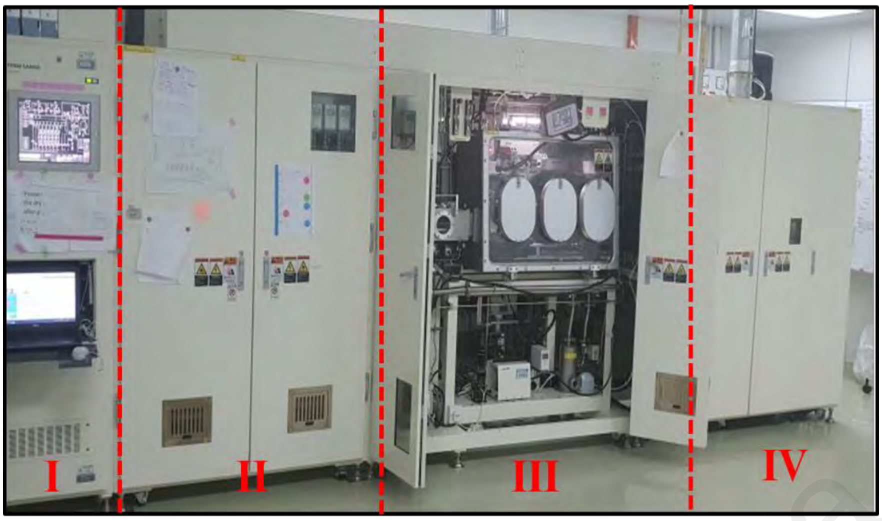


**Figure 3.1: Taiyo Nippon Sanso, SR-2000 MOCVD system with its 4 main compartments.**

As mentioned in the previous chapter, the factors that would contribute towards the quality of the grown epilayers includes the pressure, temperature, MO sources, nitrogen precursor, and gas carrier. The pressure within the reactor where the reaction between the gases occur is altered and maintained via the use of a dry pump which is controlled by the programmable logic controller (PLC). Generally, the PLC would control every aspect of the MOCVD such as the MFCs, valves, pressure, temperature, and etc. Due to the growth being highly dependent on the growth pressure, such parameter must be constantly maintained at the desired value via the pump system. The chemical reactions during the growth however, occurs within the flow channel in the reactor as presented in Figure 3.2.

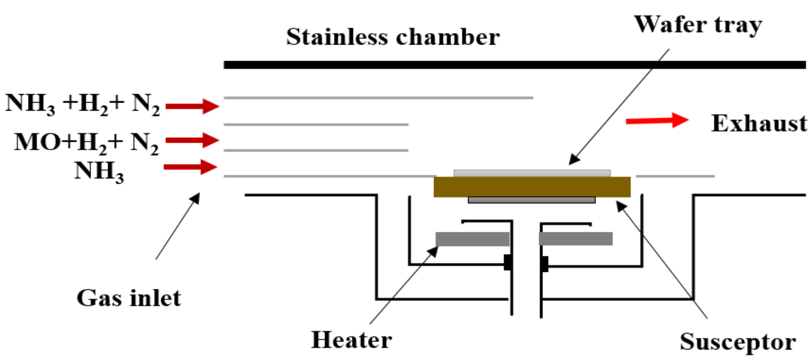


**Figure 3.2: SR-2000 reactor schematics with three gas flow system.**

From the figure, it can be observed that few key components involved is highlighted. The FC comprises of three nozzle gas inlets. The top inlet allows the flow of hydrogen ($H_2$) and Nitrogen ($N_2$) gasses to counter-balance the pressure of the two underlying nozzle inlets (also known as the subflow) which ensures a continuous film can be obtained (Nakamura, 1991). The metal precursors (in the form of trimethylgallium (TMG), trimethylaluminum (TMA) flows through the middle inlet whilst the nitrogen precursor (in the form of ammonia) flows through the bottom inlets. The presence of the 3-vertical aligned gas flow channel ensures the prevention of premature gas phase reaction prior to the growth occurrence on the substrate. The substrate is placed on a wafer tray which sits above a rotating susceptor and attached to a temperature heater below. The sidewalls of the heater are further covered by a boron nitride reflector to ensure the consistency of the temperature provided to the substrate. Finally, any excess gases by-products will flow through the exhaust outlet towards a hydrogen burner system.

It should also be pointed out that within the growth, few key calculations must be taken into account which is well known to contribute to the growth conditions. This includes the calculation of the commonly known V-III ratio ($\boldsymbol{M_{NH_3}/M_{MO}}$), where:

$$M_{MO}(mol/\,min) = \frac{F_C(sccm)}{22{,}400(cm^3/mol)} \times \frac{P_V}{P_T - P_V} \tag{3.1}$$

$$M_{NH_3}(mol/\,min) = \frac{F_{NH_3}(sccm)}{22{,}400(cm^3/mol)} \tag{3.2}$$

Since the MO and $NH_3$ flux is measured in standard cubic centimeters per minute (sccm) the unit conversion through Equation (3.1) and (3.2) must first be realized prior to attaining the V-III ratio where $F_C$, $P_V$, $P_T$ and $F_{NH_3}$ are the flow rate of the carrier gas, MO vapor pressure, total pressure and ammonia gas flow rate respectively.

Additionally, the main reaction pathway of the precursors during the growth is as shown in Equation (3.3) and (3.4) where decomposition of $NH_3$ and the methyl eliminations occurs prior to the GaN formation. However, numerous factors can contribute to the resulting outcome which might be resulted from the deviation of the growth reaction pathway which is elaborated in the next sub-chapter.

$$NH_3 \longrightarrow \frac{1}{2}N_2 + \frac{3}{2}H_2 \tag{3.3}$$

$$(CH_3)_3Ga + NH_3 \xrightarrow{T\,°C} GaN + 3(CH_4) \tag{3.4}$$

### 3.1.2 Growth Phases

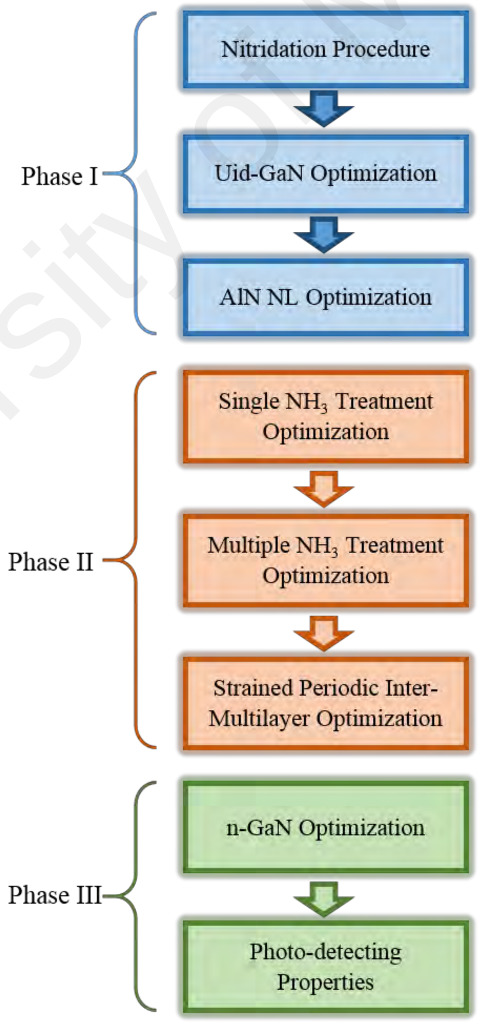


**Figure 3.3: Growth methodology included within the entire work.**

The growth phases included within the whole study are as depicted in Figure 3.3. The whole work comprises of three phases. In the first part of phase I, the aim of the optimization is to acquire a single crystal semi-polar (11-22) GaN epilayer without any additional nucleation layer (NL) or buffer layer (BL) by which the nitridation procedure was first pre-optimized. Subsequently, optimization of the thick Uid-GaN epilayer was conduction by varying the V/III ratio. Once the acceptable quality of the thick epilayer was achieved, the insertion of an aluminum nitride (AlN) NL prior to the thick GaN epilayer for better crystal and morphological quality was conducted. The AlN NL optimization includes the use of dissimilar TMA flow whilst the $NH_3$ flow kept constant yielding different V/III ratio. It should be noted that the first 2 optimizations within phase I is the most crucial optimization step as it will be further used in the subsequent growth until the device application. Table 3.1 summarizes the growth optimizations for phase I. All the growth steps in all three phases were kept at constant temperature of 1050 °C and pressure of 13.3 kPa.

**Table 3.1: Summary of the growth parameters variations in phase I of the work.**

| **Optimization Step** | **Parameters Changed** | **Sample I.D** | **Uid-GaN parameter** | |
|---|---|---|---|---|
| | | | **TMG flow (sccm)** | **$NH_3$ flow (slm)** |
| Nitridation | With nitridation<br>Without nitridation | -<br>- | 60.00 | 0.7 |
| | | | | |
| Uid-GaN | Low to High $NH_3$ flow | UG-1<br>UG-2<br>UG-3 | 60.00 | 0.4<br>0.7<br>1.0 |
| | | | **AlN NL parameter** | |
| | | | **TMG flow (sccm)** | **$NH_3$ flow (slm)** |
| AlN NL | Low to High TMA flow | NL-1<br>NL-2<br>NL-3 | 50.00<br>75.00<br>98.50 | 2.3 |

The next phase of the study comprises of a step-by-step optimization of additional defect reduction technique such as the single-step in-situ ammonia treatment, followed by the in-situ multiple alternating ammonia treatment and finally the insertion of the strained periodic AlN/GaN multilayers. All the growth conditions were taken from the previous pre-optimized growth parameters. In this phase, a detailed analysis of each technique as well as its respective outcome will be discussed and further elaboration on which would endure the better quality. The final phase of the work will include the growth of an n-type GaN on the enhanced pre-optimized semi-polar template prior to the device fabrication. The summary of the growth conditions is tabulated in Table 3.2.

**Table 3.2: Summary of the growth parameter variations in phase II and phase III of the work.**

<table>
<tr><th rowspan="2">Optimization Step</th><th rowspan="2">Parameters Changed</th><th rowspan="2">Sample I.D</th><th colspan="5">$NH_3$ treatment step</th></tr>
<tr><th colspan="3">$NH_3$ flow</th><th colspan="2">Duration</th></tr>
<tr><td>Single $NH_3$ treatment</td><td>Short to Long duration</td><td>ST-1<br>ST-2<br>ST-3</td><td colspan="3">1 slm</td><td colspan="2">90 seconds<br>180 seconds<br>360 seconds</td></tr>
<tr><td colspan="3" rowspan="2"></td><th colspan="5">$NH_3$ treatment step</th></tr>
<tr><th>$NH_3$ flow</th><th colspan="2">Duration</th><th colspan="2">Alternates</th></tr>
<tr><td>Multiple $NH_3$ treatment</td><td>Low to High alternates</td><td>MT-1<br>MT-2<br>MT-3</td><td>1 slm</td><td colspan="2">5 seconds</td><td colspan="2">20<br>40<br>60</td></tr>
<tr><td colspan="3" rowspan="2"></td><th colspan="5">I-ML step</th></tr>
<tr><th>AlN</th><th colspan="2">GaN</th><th colspan="2">Pairs</th></tr>
<tr><td>AlN/GaN multilayers</td><td>Low to High pairing of AlN/GaN</td><td>I-ML-1<br>I-ML-2<br>I-ML-3<br>I-ML-4<br>I-ML-5<br>I-ML-6</td><td>Same growth condition as AlN NL</td><td colspan="2">Same growth condition as Uid-GaN</td><td colspan="2">20<br>40<br>60<br>80<br>100<br>200</td></tr>
<tr><td colspan="3" rowspan="2"></td><th rowspan="2">Template</th><th colspan="4">n-GaN step</th></tr>
<tr><th>TMG (sccm)</th><th colspan="2">$NH_3$ (slm)</th><th>$Si_2H_6$ (sccm)</th></tr>
<tr><td>n-type GaN</td><td>Low to high disilane ($Si_2H_6$) flow</td><td>NG-1<br>NG-2<br>NG-3<br>NG-4</td><td>I-ML-6</td><td>60.00</td><td colspan="2">0.7</td><td>5<br>10<br>15<br>20</td></tr>
</table>

## 3.2 Device Fabrications

In the device fabrication, the pre-optimized n-GaN templates will undergo various fabrication steps which includes the photolithography and metal contact deposition. The proposed structure for this study is the metal-semiconductor-metal (MSM) UV-photodetector where the main instrument utilized would comprise of the mask aligner, spin coater and electron beam deposition technique.

### 3.2.1 Photolithography

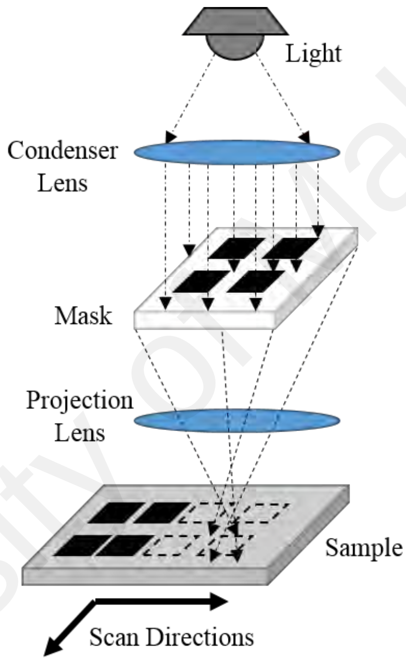


**Figure 3.4: Mask aligner working principle.**

In photolithography, a mask aligner is commonly used for imprinting a desired mask on a pre-deposited photoresist (PR) on a sample. It is an instrument which a microfabrication process is used to selectively remove parts of a thin film to create a pattern or a design onto a substrate (Stuerzebecher et al., 2010). Figure 3.4 depicts the schematic illustration of the working principles of a standard mask aligner system which comprises of the main key components: light source, condenser and projection lens, patterned masks and the sample stage.

To generate the desired pattern, the substrate is first coated with a light-sensitive photoresist prior to introducing it into the mask aligner. A mask with the desired pattern is then inserted into a stage placed above the substrate. A high intensity ultraviolet light is superimposed over the mask through the condenser lens (Stuerzebecher et al., 2010). Since the mask consists of openings/closings, transmittance of the light will be allowed through the openings in the pattern resulting in the pattern to evaporate corresponding areas of the photoresist layer on the substrate which is also known as shadow printing process. Further baking the patterned masks or developing would then commence based on the type of PR used prior to the contact deposition through the different various vapor deposition methods.

### 3.2.2 Electron Beam Deposition

The electron beam deposition (or also known as electron beam evaporation, EBPVD) is a type of physical vapor deposition technique. The e-beam offers the directionality of the deposition process enabling efficient undercut of the resist with easier subsequent lift-off. As oppose to the thermal evaporation (TE) deposition technique, the electron beam deposition offers a significantly higher purity deposition of the desired material. This is due to the TE only heats the surface of the target material rather than the material and crucible entirely as in the thermal evaporation technique. If the crucible is also heated, there would be a probability of the charge contaminations due to the impurity diffusion from the crucible to the charge (Vu et al., 2019).

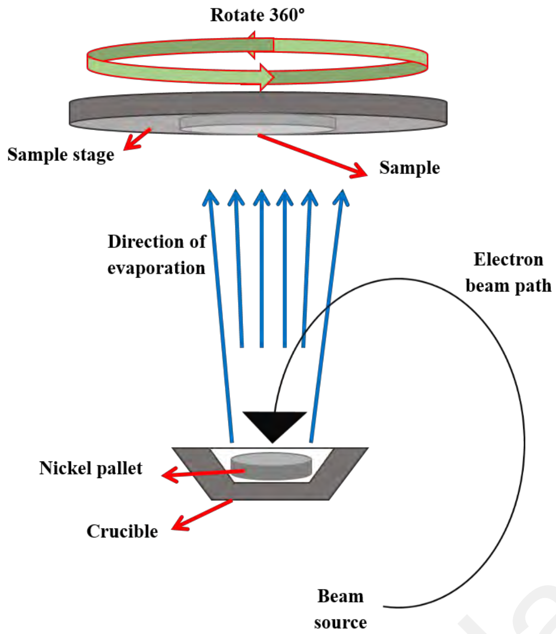


**Figure 3.5: Working principles of an electron-beam deposition technique.**

The general working principles of the EBPVD is as depicted in Figure 3.5 where the key components are highlighted. The operational principles is as follows: (i) the tungsten filament was charged up and an electron beam is given off, (ii) the bending of the electron beam towards the target materials within a crucible which is connected to a cooling system, (iii) bombardment of the target material causes the atoms from the target material to transform into its gaseous phase, (iv) the gaseous atoms evaporates towards the target substrate located above and precipitate into solid form coating the substrate as well as the entire walls of the vacuum chamber. Few advancements have been made with the current available e-beam systems where the system can be controlled rather precisely with the presence of additional thickness controller, automatic shutters, and automatic pocket control which allows different materials to be deposited subsequently after each other. This enables a staggered metal structure deposition for various purposes such as titanium (Ti)/Aluminum (Al)/Nickel (Ni)/Gold (Au) for light emitting diode applications with significant lower time consumption. The thickness meter and automated shutter would also allow better surface homogeneity of the deposited material. Normally, the thickness meter will be positioned below the substrate shutter as to measure the depositional rate prior to the actual deposition. This prevents premature deposition of the material which causes a fluctuation of the desired thickness as well as surface inhomogeneity. In this work, a (Korea coating materials and components, KCMC) e-beam deposition was utilized. In this system, the e-beam can either be operated manually via the analog control panel or automatically controlled via the PLC. The target material used is nickel (Ni) pallets, with deposition rate of 1Å per second. The deposition time used were 100 seconds for a desired thickness ~100 nm.

## 3.3 Characterization Techniques

### 3.3.1 High-Resolution X-ray Diffraction (HR-XRD)

In the field of crystallography, x-ray diffraction have been the main driving tool for crystal analysis. This includes determination of crystal phases, crystal quality, in/out plane strain/stress state of the crystal, and defect density estimations. Even though the conventional XRD systems have been around for decades and proven its uses, newly developed high-resolution XRD systems have advanced the capabilities of its older counterparts. In general, the HR-XRD performs similar to the conventional XRD systems with additional advanced setup such as monochromators (2-bounce or 4-bounce monochromator), goniometers (with $2\theta$, $\omega$ 2-axes + tilt ($\chi$) and rotation ($\Phi$) (=4-axes goniometer)), and optional detectors (1D or 2D). Such advancements is crucial for further detailed crystal analysis which will elaborated later in the chapter.

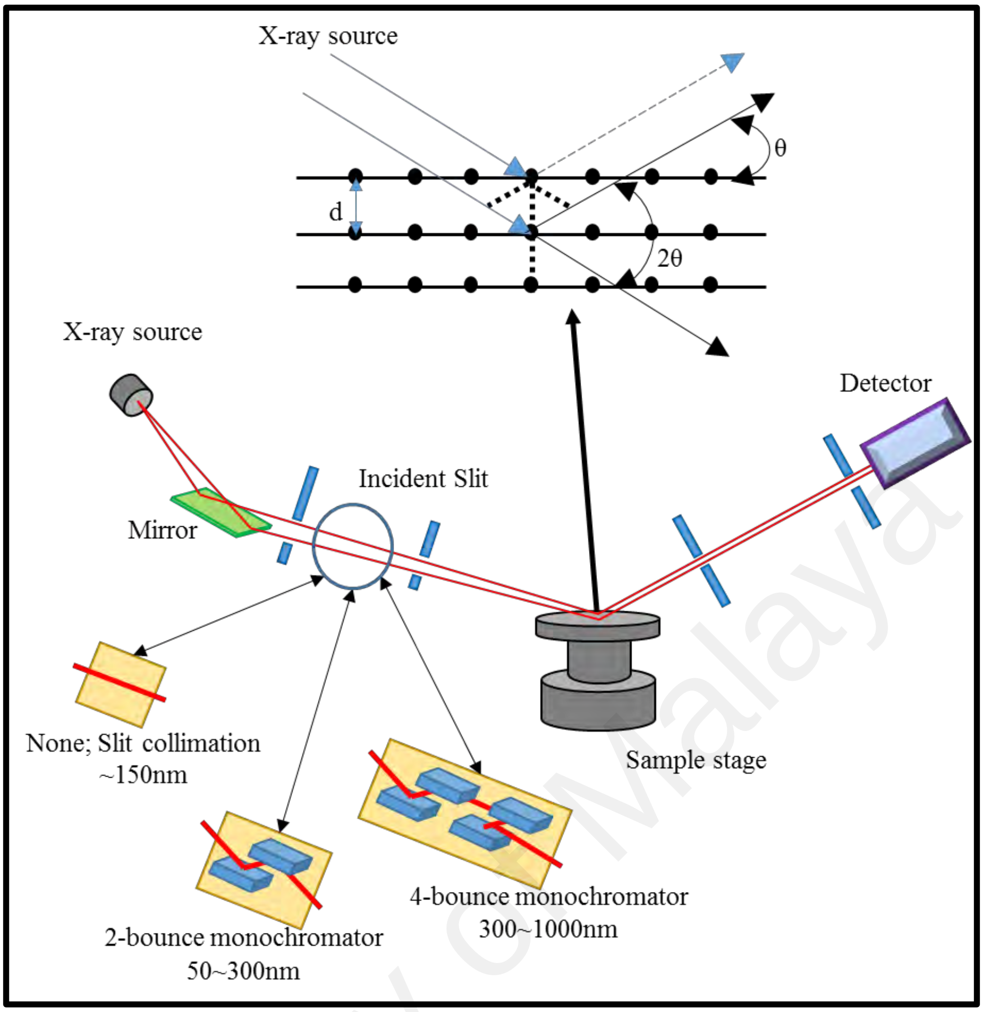


**Figure 3.6: Schematic illustration of the key principles involved in a HR-XRD measurement system.**

The key principles of XRD systems operates via x-ray light projection on a material. Figure 3.6 depicts the working principles governed by the XRD system. As the x-rays (generated by the cathode ray tube) were focused on the test sample, a constructive interference is generated as a consequence of the interaction between the incident beam and the test sample. The constructive interference would result in diffraction where the emitted x-rays is a component of the characteristic angles depending on the test samples atomic spacing giving rise to the variant crystal planes illumination. The correlation between the atomic spacing (d), angle and wavelength should obey the Bragg's Law:

$$2d \cdot \sin\theta = n\lambda \tag{3.5}$$

Where $\lambda$ is the wavelength of the x-ray, $n$ is the diffraction order, $\theta$ is the incident angle and $d$ is the interplanar spacing of the reflected planes. From the equation, as the illuminating wavelength is known, the diffracted angle can be measured by the diffractometer and hence the interplanar distance can be known.

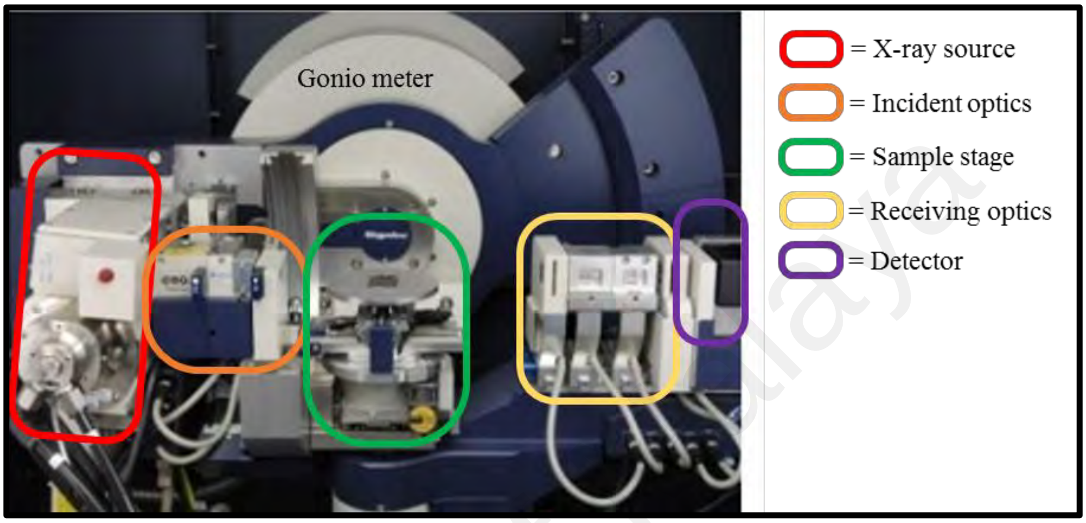


**Figure 3.7: The key components of the Rigaku HR-XRD measurement system.**

In this work, the Rigaku HR-XRD as depicted in Figure 3.7 was utilized which generally consist of an x-ray tube (operating at high voltage of 10-40 kV), Ge (220) 2-bounce monochromator (for thin film suitability) incident optics, sample stage (4-axes goniometer), receiving optics and detector. Prior to each measurement, sample calibration was conducted to determine the $2\theta$ zero point and further measurement of the $2\theta/\omega$ scan, x-ray rocking curve (XRC) and reciprocal space mapping (RSM) can now be conducted.

In the phase analysis, samples were rotated by $\omega$ whilst the detector was fixed at $2\theta$ hence the plot of $2\theta/\omega$ with its corresponding XRD intensity would be attained. This would aid in revealing the crystallographic nature of the sample. Since semi-polar (11-22) GaN growth have been known to exhibit various diffracted peaks corresponding to the polycrystalline nature of the growth orientation (due to unsuitable growth conditions), determination of the resulted crystal orientation must be addressed. It is crucial, to ensure a single crystal semi-polar (11-22) GaN was achieved as to eliminate additional contributing factors towards the epilayer property which will further impact the device performance.

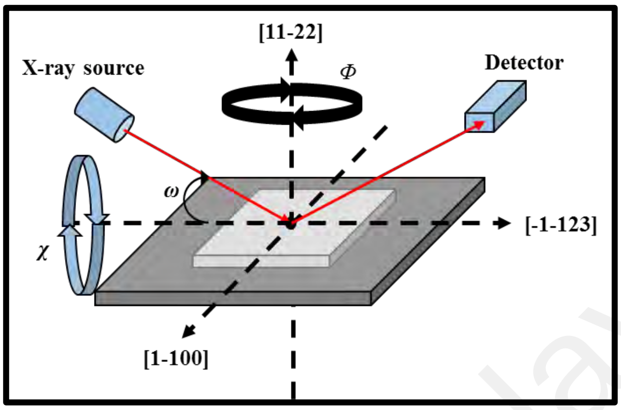


**Figure 3.8: Schematic diagram of the experimental setup for all XRD, XRC on- and off-axis measurement.**

Distribution of diffraction intensity along the reciprocal lattice vector would then be measured via the XRC measurement. The XRC measurement was performed by rocking the sample stage via $\omega$ whilst the detector was fixed at the $2\theta$ angle as depicted in Figure 3.8. In doing so, the peak width of the rocking profile would be determined and correlated with the tilt in the Bragg's angle. Such phenomenon would highly be influenced by the presence of defects within the crystal. The two common XRC measurement employed is the on-axis (symmetric plane) and off-axis (asymmetric plane) XRCs. Both axis XRC would have their own rocking profiles broadening factors.

Within this work, the on-axis XRC was conducted on the (11-22) reflection whilst rotating the azimuthal angle ($\Phi$). The steps interval was chosen at 30° increments from 0 to 360°along the azimuth ($\Phi$). It should be noted that the angle was set at 0° and 90 when the beam projection was parallel to [-1-123] and [1-100] respectively. In semi-polar, an occurrence of different broadenings within both directions have been reported to occur due to the various reasons as mentioned in the previous chapter, which results in the commonly known M-shaped azimuthal dependence profile. This phenomenon is also known as the crystal anisotropic properties wherein the FWHM along [1-100] is always broader than along [-1-123].

On the other hand, the off-axis XRC was conducted as to determine detailed defects dependence XRC broadenings. As mentioned in the previous chapter, the defects generated in semi-polar GaN would mostly consists of BSF type $I_1$ and $I_2$, PSFs, partial dislocations and perfect dislocations. Each defect has their own respective formation direction/plane whereby it cannot be distinguished via a single XRC measurement. This requires the variant off-axis XRC measurement wherein specific diffraction planes were analyzed via dissimilar incident beam direction consisting of $\omega$, $2\theta$, and $\chi$ variations.

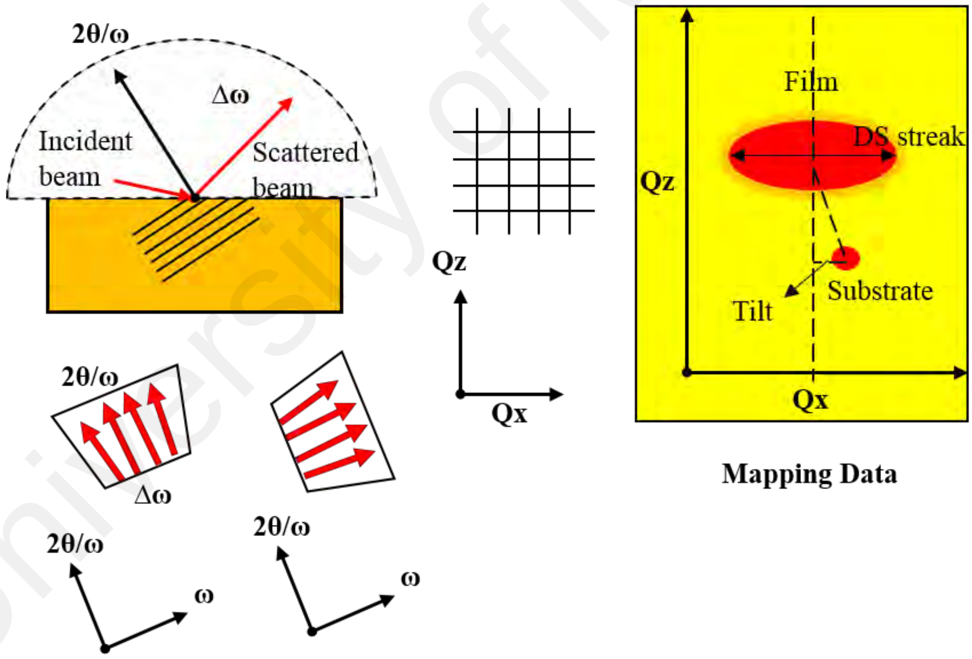


**Figure 3.9: Schematic illustration of the type of measurement performed in the RSM configuration.**

The final stage of the HR-XRD measurements was the RSM analysis. From the RSM, additional information regarding the crystal orientation, relaxation and certain defects estimation. The RSM measurement obtains the distributions of the diffracted intensity via scanning the diffraction angle whist rotating the sample. The results were then plotted in the reciprocal space to yield the RSMs. Upon scanning the $2\theta$ and $\omega$ with specific $\chi$ and $\Phi$ in the scattering plane, the peak position and shape of the reciprocal lattice points (RLPs) can be acquired. Three main scanning variations of RSMs can be conducted as depicted in Figure 3.9: (I) $2\theta/\omega$ step ω scan (where the $2\theta/\omega$ was gradually changed whilst repeating the $\omega$ scan, (II) $\omega$ step $2\theta/\omega$ scan (where the $2\theta/\omega$ scan were repeated whilst the $\omega$ was gradually changed and (III) the mesh measurement (where the axes were scanned whilst the step intervals in the Q coordinates were kept constant. The main interest in the RSM measurement for semi-polar GaN would be the diffuse scattering (DS) streaks elongation as well as the tilt in the RLPs. Studies have shown that along [-1-123], the DS streak elongations would correspond to the presence of PSFs whilst the RLP tilts correspond to the relaxation state of the grown epilayers.

### 3.3.2 Atomic Force Microscope (AFM)

Amongst the various scanning probe microscope (SPM) available, AFM has shown dominance in its reliability of measuring the surface property of a material with great accuracy. Generally, an AFM utilizes a probe to scan the surface of a material generating superior information regarding the surface property via topographic. Various details could be obtained such as surface roughness, undulations, and even grain sizes down to sub-nanometer range. The working principle of an AFM is as illustrated in Figure 3.10 where the main components are elucidated. When a sample is measured the measuring tip will move across the sample surface, in a defined grid. The forces between the small measuring tip and the surface of the sample will then be measured via the solid-state laser deflected towards the photo-sensor. The deflection oscillation signal would then be process through the preamplifier and DC converter which will finally be sent to the Z-voltage feedback circuit along with the signals from the Z-piezo actuators. The signals are then processed via the CPU software simultaneously with signal from the X- and Y-piezo actuators resulting in the topographic image of the sample.

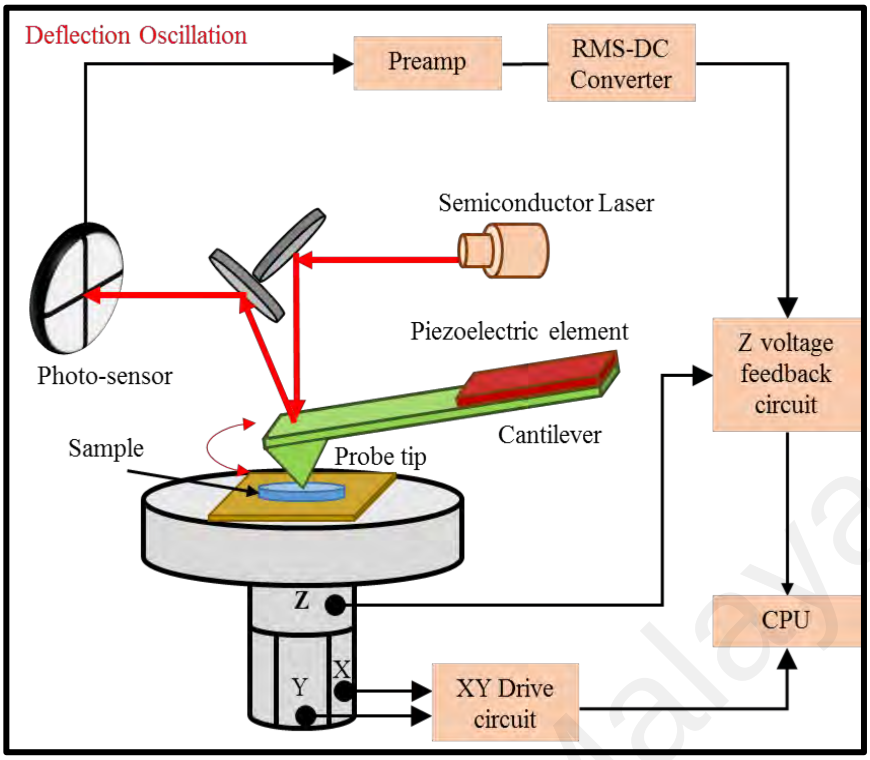


**Figure 3.10: Schematic illustration of the working principles of an AFM with its key components.**

Few key advancements have been realized in the AFM measurement where the use traditional tripod architecture for sample stage was replaced with a piezo-tube actuator which comprises of individual piezo actuators for different X, Y, and Z motions. The use of piezoelectric element on the cantilever have also been developed to induce dynamic vibrations in the measuring tip for non-contact mode and dynamic force mode (DFM) or also known as tapping mode. Generally, the key differences between the existing modes of probing would include the surface contact between the probe tip and the sample surface. In contact mode AFM, the probe tip will actually come in full contact with the surface of the measured sample. If the sample surface is fragile, then the probe tip will graze the surface leading to an inaccurate imaging would be generated. However, if the probe tip is unable to graze the sample surface, then the generated image would be in the highest accuracy. Conversely, the non-contact mode AFM would endure the opposite probing method whereby the probe tip would not be in contact of the surface and the measurement relies on the attractive Van Der Waals force to generate the topographic image. However, the Van Der Waals attractive force is substantially small compared with other forces present hence induce a low resolution/accuracy topographic image. The DFM or tapping mode the cantilever is kept close to the surface whilst oscillating near its resonant frequency. The distance between the sample and the cantilever was controlled via a feedback electronic keeping either the phase or amplitude of the oscillating cantilever constant ensuring the avoidance of lateral tip-to-surface forces. This would generate higher resolution image as compared with the other two AFM modes. Within this work, the DFM mode was selected as it possesses various advantages of its contact and non-contact counterparts.

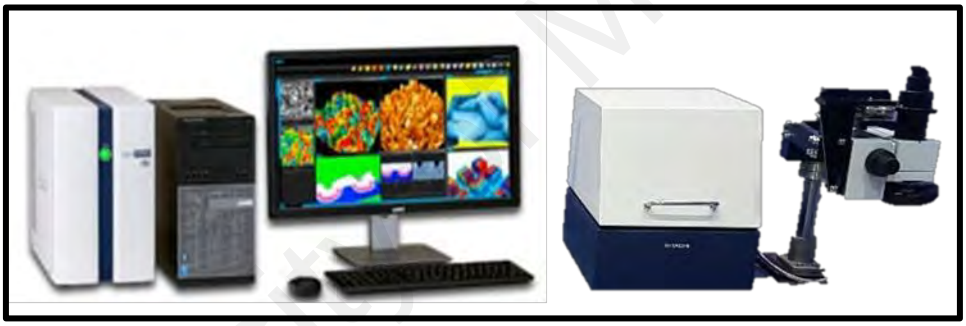

**Figure 3.11: Image of the Hitachi-AFM5000II.**

In this work, a considerably high accuracy Hitachi-AFM5000II probe station was utilized as depicted in Figure 3.11. Since semi-polar (11-22) GaN exhibit a highly irregular surface property, few additional information based on the topographic image was extracted. These includes the standard RMS roughness of the area and the highest peak-to-valley of the area measurement. In addition, the topographic images were also rendered in the 3-dimensions to elucidate the surface property. Prior to the measurement, the 2-inch sample was first cleaved with a standard issue diamond cutter into small 1×1 cm$^2$. Surface cleaning via the use of an ozone cleaner was first realized to rid of any surface contamination such as dust particles prior to the placement of the sample on the measurement stage. A rough scan of the surface was first initiated before each sample measurement as to ensure the suitability of the measured area (no contamination induced measurement). Upon realization of the area of interest, a thorough scan of the area was conducted starting from higher scan size (lower magnification) of 10×10 $\mu m^2$ to lower scan size (higher magnification) of 0.5×0.5 $\mu m^2$.

### 3.3.3 Field Emission Scanning Electron Microscope (FESEM)

Similar to conventional SEM, FESEM utilizes the same working principles with the use of different types of electron source. In SEM, the electron source comprises of a thermionic emitter where the use of a tungsten filament. However, the use of such electron source commonly thermal drift with relatively low brightness during the measurement leading to a poor image quality. FESEM on the other hand, utilizes a field emission gun (FEG) or also known as a cold cathode field emitter as the electron source. With the use of FEG, the electrons are enabled to escape from the cathode with ease to give rise to a cleaner, less electrostatic distortions images with spatial resolutions of < 2 nm. The working principles with the key components of the FESEM is as illustrated in Figure 3.12.

The steps involved prior to image generation includes: (i) Electron generation and extraction from the FEG and extracting anode, respectively, (ii) travelling electron beam passes through an accelerating anode and an electromagnetic lens for beam focusing on the sample and (iii) emission of secondary electrons (SE) post bombardment towards the detector where the signal would then be processed generating the resulting image.

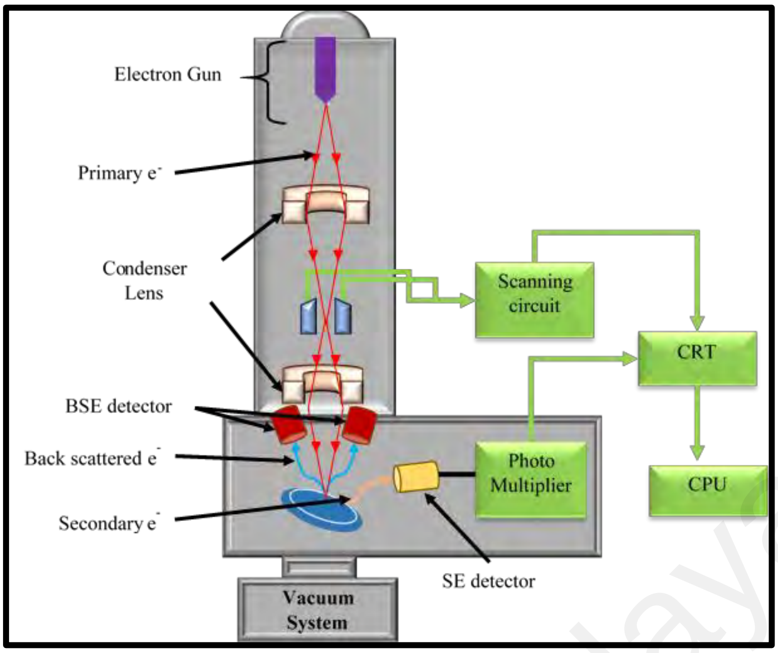


**Figure 3.12: Schematic diagram of the working principles of FESEM with different configurations (SE and BSE).**

In this study, an SU8220-Hitachi, UHR-FESEM was used for surface and cross-sectional imaging of the epilayers as depicted in Figure 3.13. It should be noted that the SU8220 (as many other FESEM) has the capability to collect and measure not only the secondary electron (SE) emitted from the sample, but also the backscattered electrons via a different type of electron detector (also known as the BSE mode). Normally, surface imaging of the epilayer was conducted via the use of SE mode as no anticipation of different material composition is expected. However, in the cross-sectional imaging, it would be more suitable to utilize the BSE mode. This is due to the function of the BSE as to ensure different contrast imaging material composition dependent image can be attained as the cross-section would comprise of different material composition. This includes interfacial composition between the sapphire substrate, thin AlN epilayer, and the thick Uid-GaN epilayer itself. Via the use of the BSE mode, such different compositional structure can be elucidated. The main interest upon FESEM imaging within this work resides with the surface morphology and epilayer structure which can be yielded via surface and cross-sectional imaging.


**Figure 3.13: The image of the Hitachi –SU8220-UHR FESEM instrument.**

Sample preparation of prior to the measurement consist of sample cleaving via the use of the standard issue diamond cutter for significantly small size (2×2 cm$^2$). This is due to the stage of the measurement stage being relatively small and utilizing a relatively large sample would not be well suited. Sample cleaving for cross-sectional purposes however requires additional care as the sample cleaving must be conducted from the surface of the sample as to ensure a clean cut of the cross-section for high quality imaging during the measurement.

### 3.3.4 Transmission Electron Microscope (TEM)

Among the various characterization methods, TEM have always been considered the ultimate tool in defects imaging. It should be noted that the term imaging must always be considered and not overlooked as the approach to quantitatively define the numbers of defect present in an epilayer. Having said that, TEM would be highly reliable when the types of defect present in an epilayer is to be revealed. This is mainly due to the main function of the TEM wherein the plane of which a crystal defect resides can be observed via imaging and most probable cause and origin of its formation can be realized. To put it simply, the working principle of a TEM is quite similar to a slide projector where the slide film is projected as a beam of light shines through and the pattern on the slide film would allow certain parts of the light beam to pass. Hence the transmitted beam replicates the pattern on the slide towards a screen (in an enlarged scale). However, TEM works by shining electrons (instead of light) through a thin specimen (instead of the slide film). In addition, the transmission of electron beam depends highly on the material properties. If a dense material is to be viewed, then lower density of electrons will be enabled to pass through giving rise to the contrast imaging of TEM and vice versa.

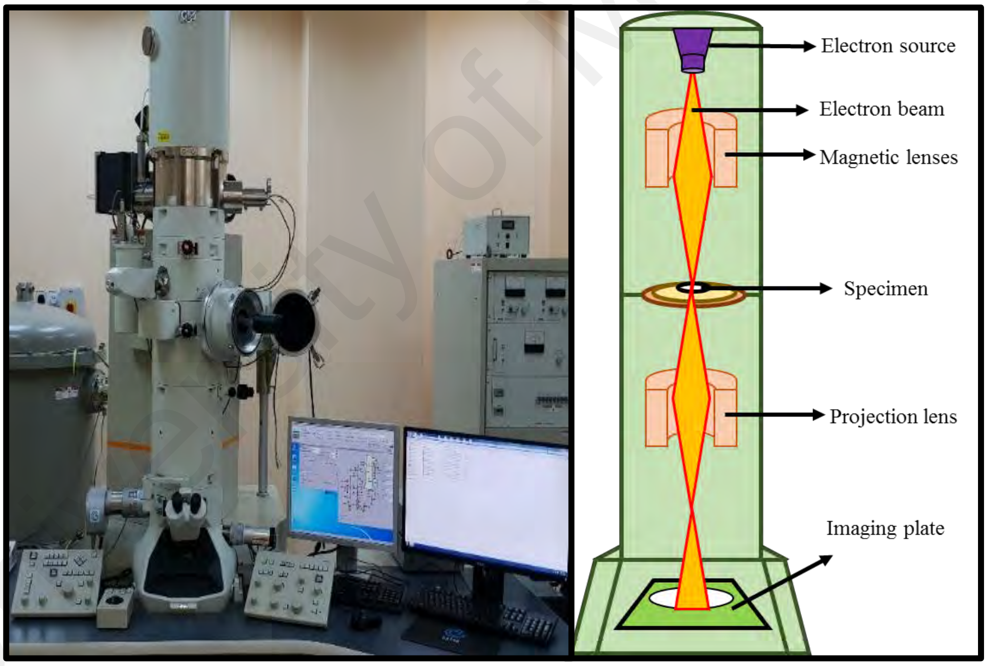


**Figure 3.14: Image of the Jeol-JEM-2100F TEM instrument with its schematic diagram of the working principles of a TEM.**

Schematic illustration of the key components of a TEM and its working principle is as shown in Figure 3.14 where (i) electrons are emitted from the tungsten filament cathode and accelerated by the positive anode below, (ii) the electron beam is focused through the electromagnetic lens and metal apertures allowing a small energy range of electrons to pass through giving then their own specific defined energy, (iii) the focused beam passes through the specimen, (iv) travels through the secondary electromagnetic lens (for electrons refocusing and enlarging the resulted image) and projection of the image onto a phosphorescent plate.

In this study, the main interest upon utilization of the TEM is to acquire and analyze the defect reduction mechanism on an enhanced semi-polar (11-22) GaN template. The preparation of the specimen, however, requires an additional step with the use of focused ion beam (FIB) technique where the sample is cut into significantly small sizes via an ion beam and the placed on a copper grid prior to the specimen thinning process. It is known that with the help of a FIB system, ensuring the specimen quality being analyzed remains in the most upmost optimum conditions (Lechner et al., 2012). Furthermore, this additional process is required as to ensure the thickness of the sample is sufficiently low enough for the electron beam to pass through and generate the desired image of the specimen. Consequently, unveiling the presence of defects within the microstructures can be realized.

It is also crucial to determine to orientation direction of the desired specimen prior to cutting and extracting. This is one of the key principles in viewing certain types of defects especially in semi-polar GaN where the defects generated possess their own plane/direction of existence. To determine such parameter, the visibility criteria of the defects must be first addressed as mentioned in the previous chapter.

### 3.3.5 Hall Effect Measurement

Within this work, various optimization was conducted including n-type GaN optimization. Due to the variations of the doping (disilane) concentrations during the growth, an additional key factor that would contribute towards the device performance is the carrier concentration/mobility. If such parameter is ignored, the absolute causality of the enhanced/degraded device performance would not be completely determined as other factors such as the surface and crystal property is also known to influence the device performance. By measuring the electrical properties, hence further detailed contributing factor towards the device performance can be determined. In this study, the Hall Effect measurement was conducted to reveal the electrical properties of the n-GaN samples. The schematic illustration of the measurement setup is as depicted in Figure 3.15.

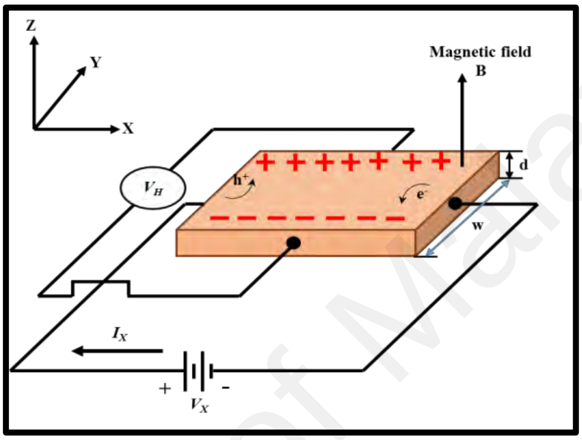


**Figure 3.15: Schematic diagram of the Hall Effect measurement setup and working principles.**

As illustrated in the figure, when a perpendicular magnetic field (***B***) is applied, the charges (electrons and holes) will experience a force called the Lorentz Force, by which their path between collisions are bent where $e^-$ are accumulated at one side of the material face whilst $h^+$ on the other. The separation of the charges generates an electric field in the direction of the assigned $\boldsymbol{V_H}$. Where the measured $\boldsymbol{V_H}$, ***B***, d, and I can be used to find the Hall coefficient ($\boldsymbol{R_H}$) defined by:

$$\boldsymbol{R_H} = \frac{\boldsymbol{V_H}\mathrm{d}}{\mathbf{B.}\,\mathrm{I}} \tag{3.6}$$

where $\boldsymbol{R_H}$ is interconnected with the findings of the conductivity and mobility given by:

$$\boldsymbol{\mu = \sigma R_H} \tag{3.7}$$

# CHAPTER 4: OPTIMIZATION OF SEMI-POLAR (11-22) UID-GAN

This chapter discusses thoroughly Phase I of the work wherein optimization of the nitridation procedure, thick unintentionally doped-GaN (Uid-GaN) growth, as well as the thin AlN nucleation layer (NL) growth conditions. These steps in Phase I are significantly important before further optimization of the semi-polar (11-22) GaN growth with additional defect reduction and surface enhancement technique in Phase II. Obtaining a pre optimized nitridation step will be further used in the subsequent Uid-GaN growth optimization. After the desired property of the Uid-GaN was achieved, such parameters would be also implemented in the optimization of the AlN NL growth and finally, all the three steps will be utilized in Phase II and Phase III of the work.

## 4.1 Nitridation

In order to fully comprehend the understanding of semi-polar (11-22) GaN grown on planar m-plane (10-10) sapphire, in depth analysis of the mechanism involved must be appointed. As numerous studies have reported on the growth techniques utilized in obtaining high quality single crystal semi-polar (11-22) GaN epilayers, it is significantly important to first optimize the nitridation procedure of the m-plane sapphire substrates. Various groups have thoroughly discussed on such importance whereby certain nitridation conditions would promote single crystal or poly-crystalline properties of semi-polar (11-22) GaN without or with a mixed (10-13) plane, respectively (Ploch et al., 2010; Wang et al., 2017; Won et al., 2014). This work elaborates the significance of such procedure which highlights the resulting outcome of flat two dimension of semi-polar (11-22) GaN and three dimensions of semi-polar (11-22) GaN with presence of (10-13) and (10-10) facets being exposed.

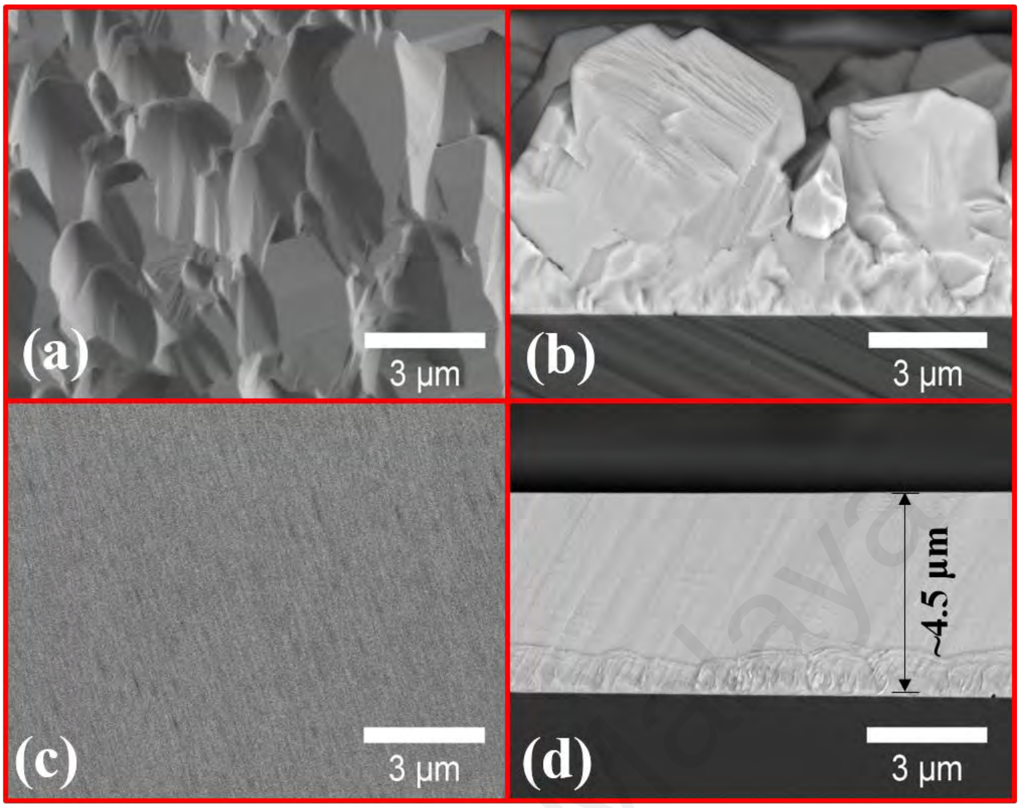


**Figure 4.1: FESEM images of the surface and cross-section of the samples (a-b) without (sample (B)) and (c-d) with nitridation procedure (sample (A)) prior to the growth of the subsequent Uid-GaN epilayer.**

Figure 4.1 depicts the FESEM surface and cross-sectional images of the resulting outcome with (sample (A)) and without a nitridation step (sample (B)). It should be noted, the GaN growth conditions were kept constant for both sample (A) and (B). From Figure 4.1 (c-d), it clearly observed that the use of a pre-optimized nitridation procedure would help facilitate the growth orientation towards the desired direction (11-22) (sample (A)). However, if the nitridation procedure was to be skipped (sample (B)), the results indicate immense island-like protrusions were formed as in Figure 4.1 (a-b). It was presumed by many that the nitridation procedure helps to change/tilt the surface of the sapphire from m-plane (10-10) towards semi-polar (11-22) (Won et al., 2014).

HR-TEM images in Figure 4.2 shows the origins of the tilting process governs by the nitridation procedure. From the image it can be observed that there is an existence of nano-sized protrusions on the surface of the sapphire substrates prior to the thick semi-polar (11-22) GaN epilayer. Such protrusions have changed the surface orientation from (10-10) m-plane towards (11-22) semi-polar. This in turn facilitates the growth orientation along semi-polar (11-22) GaN.

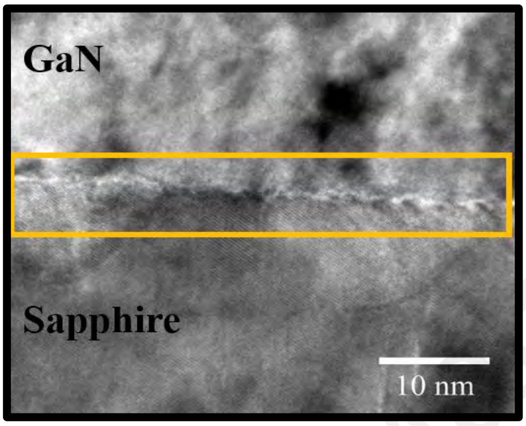


**Figure 4.2: TEM image of the sapphire and GaN interface revealing the nano-sized protrusions upon implementing the nitridation procedure.**

If the nitridation procedure was taken out, non-polar (10-10) GaN nuclei would be formed on the m-plane sapphire during the GaN epilayer growth commencement due to its low surface energy formation (Frentrup et al., 2011; Won et al., 2014). The [10-10] GaN epilayer would be predominantly grown if the growth conditions of the GaN favors such orientation. However, since the growth conditions favors the growth conditions of semi-polar (11-22) GaN, then various planes such as (11-22), (10-13) and (10-10) will be simultaneously exhibited. Despite that, imbedding the nitridation procedure prior to the growth of the subsequent GaN epilayer would change the surface polarity of the surface progressively with time, from (10-10) m-plane towards (11-22). As the surface of the sapphire was exposed to $NH_3$ at elevated temperatures, the probability of N atoms to adhere towards the surface is high. This would allow substitution of the oxygen (O) atoms in the sapphire ($Al_2O_3$) matrix on the vicinity of the surface with N atoms forming nano-sized oxynitride protrusion with slanted facets consists of AlN/AlON composites

(Vennégués et al., 2010; Wang et al., 2017). The existence of AlN/AlON step-wise structure is also known to effectively relieve the lattice mismatch between the subsequent epilayer growth and the sapphire favoring the semi-polar (11-22) GaN growth orientation (Vennégués & Beaumont, 1999). It should be noted that even with nitridation procedure being implemented, the properties of the resulting GaN epilayer would also rely on the growth conditions of such epilayer, as few studies have also shown the use of dissimilar nitridation step would yield acceptable quality of the subsequent GaN epilayer (Won et al., 2014). In addition, other parameters such as growth temperature, pressure, and carrier gases as well as the methods of epitaxial growth (MOCVD, MBE, etc.) plays a big role in determining such resulting outcome (Lahourcade et al., 2007; Stellmach et al., 2012). The outcome of the nitridation procedure here is based on the growth conditions implemented in this work specifically. Due to that, the exact same nitridation procedure would be maintain for the rest of the work with various subsequent growth conditions of the semi-polar (11-22) oriented epilayers.

## 4.2 Unintentionally doped semi-polar (11-22) GaN (Uid-GaN)

In this part of the work, upon obtaining the preferred nitridation conditions, the 1 step growth technique was first implemented to obtain the optimum growth conditions of semi-polar (11-22) GaN. Since various growth conditions could be implemented which would constitute dissimilar epilayer properties, hence obtaining the optimum growth conditions of the epilayers via the 1-step approach is crucial prior to additional growth steps for crystal quality enhancement. Studies have shown, with proper nitridation procedure and V/III ratio for the GaN epilayer growth, single crystal (11-22) oriented GaN would be predominantly grown whilst other planes of orientation being significantly suppressed (Sun et al., 2009b; Won et al., 2014). As the nitridation was optimized, the tuning of the V/III ratio should be of concern, via TMG flux variation or $NH_3$ flux variation.

### 4.2.1 The growth condition involved

Optimization of the semi-polar (11-22) Uid-GaN epilayers were further conducted to obtain the optimum growth conditions by varying the ammonia ($NH_3$) flux with a fixed trimethylgallium (TMG) flow rate. Three samples were grown with 0.4, 0.7 and 1.0 standard liter per minute (slm) of $NH_3$ variation with constant TMG flow of 60 standard cubic centimeters per minute (sccm) designated as UG-1, UG-2 and UG-3 respectively. This would yield the V/III ratio of 66, 115, and 165 in the same order. To avoid additional influence towards the growth, temperature and pressure of the reactor were kept at 1050°C and 13.3 kPa for all three samples. Growth conditions is as depicted in Figure 4.3: (a) the substrate was first annealed for 10 minutes in hydrogen ($H_2$) ambience at 1125°C (to clear of any contaminations on the substrates), (b) followed by the nitridation procedure as described previously and finally (c) the Uid-GaN growth for 30 minutes to yield 4.5 μm thickness. It should be noted that within this part of the optimization, no buffer nor nucleation layer were grown prior to the Uid-GaN. All the pre-growth procedures such as $H_2$ cleaning and nitridation procedures were also kept constant. This was done to ensure absence of additional influence on the Uid-GaN epilayers crystal and morphological qualities, prioritizing the growth conditions of the Uid-GaN only.

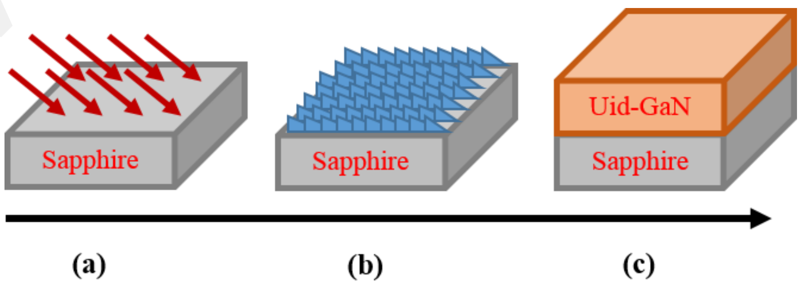


**Figure 4.3: Growth conditions of semi-polar (11-22) Uid-GaN starting form (a) $H_2$ clean, (b) nitridation and (c) 4.5m thick Uid GaN.**

### 4.2.2 Impact of V/III Ratio on the Crystal Quality of Uid-GaN

As mentioned in the previous chapter, the crystal quality analysis was conducted via the use of HR-XRD including $2\theta/\omega$ scan, rocking curve as well as reciprocal space mapping. Since numerous studies have reported that even with an optimized nitridation procedure, the probability of obtaining polycrystalline samples is high as the growth conditions were varied at different growth condition/environment (Dinh et al., 2015; Mogilatenko et al., 2014). Hence, acquiring the crystal orientation information is crucial and via the $2\theta/\omega$ scans such matter can be revealed. Figure 4.4 portrays the $2\theta/\omega$ scan of all three samples of UG-1, UG-2 and UG-3 (refer to Table 3.1). From the spectrum, two dominant peaks can be observed which corresponds to the sapphire substrate as well as the semi-polar (11-22) GaN epilayer. Absence of other peaks which corresponds to m-plane (10-10) and semi-polar (10-13) signifies the achievement of single crystal semi-polar (11-22) GaN epilayer (Ploch et al., 2010). However, in order to further analyze the quality of the epilayer, x-ray rocking curve (XRC) symmetric (on-axis) and asymmetric (off-axis) measurement was implemented.

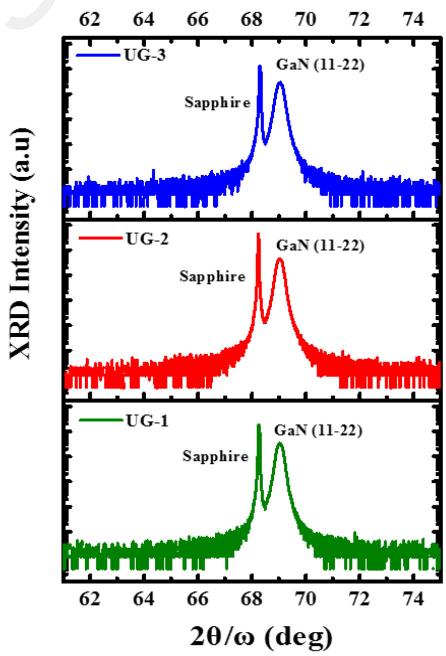


**Figure 4.4: HR-XRD, $2\theta/\omega$ scans of all three samples with different $NH_3$ flux.**

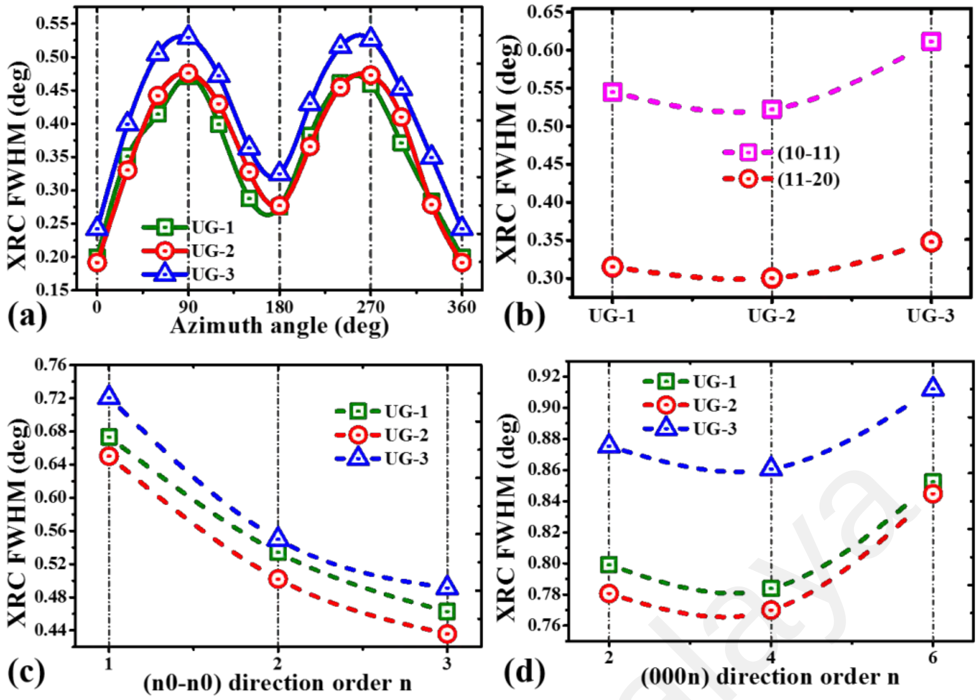


**Figure 4.5: XRC FWHMs of UG-1, UG-2 and UG-3 via (a) on-axis configuration and (b) off-axis configuration along (10-11) and (11-20), (c) the (n0-n0) series and (d) the (000n) series.**

Figure 4.5(a) corresponds to the on-axis XRC by which a plot of the FWHMs as a function of the azimuthal angle with 30° intervals for the whole 360° rotation. As mentioned in the previous chapter, the on-axis XRC measurement would enable the analysis of the anisotropic property of the epilayers. From the figure, UG-2 portrayed the lowest FWHM along [-1-123] and [1-100] around 0.19° (684 arcsec) and 0.47° (1692 arcsec) respectively, followed closely by UG-1. UG-3 however, exhibits rather higher FWHMs along both direction around 0.24° (864 arcsec) and 0.53° (1908 arcsec) respectively, signifying the worst anisotropic property with overall lowest crystal quality. Semi-polar GaN is known to exhibit such anisotropic property due to the lattice mismatch between the GaN epilayer and sapphire substrate resulting in the XRC FWHM along [1-100] being significantly broader than along [-1-123] (Xu et al., 2012; Zhao et al., 2016). Such broadening in the on-axis XRC FWHMs is presumed to be attributed from various factors which includes the GaN lattice distortion resulting in the generation of numerous types of stacking faults, and dislocations (Kriouche et al., 2010; Zhao et al., 2016). In general, a reduced anisotropy in the XRC FWHMs along both [-1-123] and [1-100] should correlate directly with the crystal enhancement with lower defects densities.

In order to reveal further details of the crystal properties related defects such as basal plane stacking faults (BSFs), prismatic stacking faults (PSFs), partial and/or perfect dislocations, off-axis XRCs were implemented. As mentioned in the previous chapter, semi-polar GaN suffers greatly from the generation of defects such as BSFs as well as other lower density types of dislocations (Dasilva et al., 2010). The off-axis measurement is highly sensitive towards the presence of BSFs in contrast to the on-axis XRCs (Moram & Vickers, 2009; Sun et al., 2009a; Sun et al., 2009b). The first series of the off-axis XRC measurement was conducted along (10-11) and (11-20) planes as depicted in Figure 4.5(b). As mentioned in the previous chapter, the diffraction planes of (10-11) and (11-20) are highly sensitive towards the existence of perfect dislocations and PSFs (Moram et al., 2009) igniting the fact that UG -2 exhibit lowest density compared with UG-1 and UG-3. Furthermore the off-axis (n0-n0) XRCs was also measured as presence of the commonly existing BSFs would greatly broadened the FWHMs (Moram et al., 2009; Vennéguès et al., 2007). Figure 4.5(c) presents the (n0-n0) XRC FWHMs along the m-plane direction with n = 1, 2, and 3 for all samples. From the figure, it can be observed that UG-2 exerts the lowest FWHM broadening in all (10-10) and (20-20) planes compared with UG-1 and UG-3 suggesting lower presence of BSF type $I_1$ and type $I_2$ respectively (McLaurin et al., 2008; Moram & Vickers, 2009). Partial and/or perfect dislocations with Burgers vectors having a c-axis component also portrayed similar trend in FWHMs reduction for UG-1 and UG-2, as depicted in Figure 4.5(d) (000n) series measurement (Sun et al., 2009b; Vennéguès et al., 2007). However, UG-3 showed immense broadening within the (000n) series signifying highly abundant presence of partial and/or perfect dislocations as compared with UG-1 and UG-2.

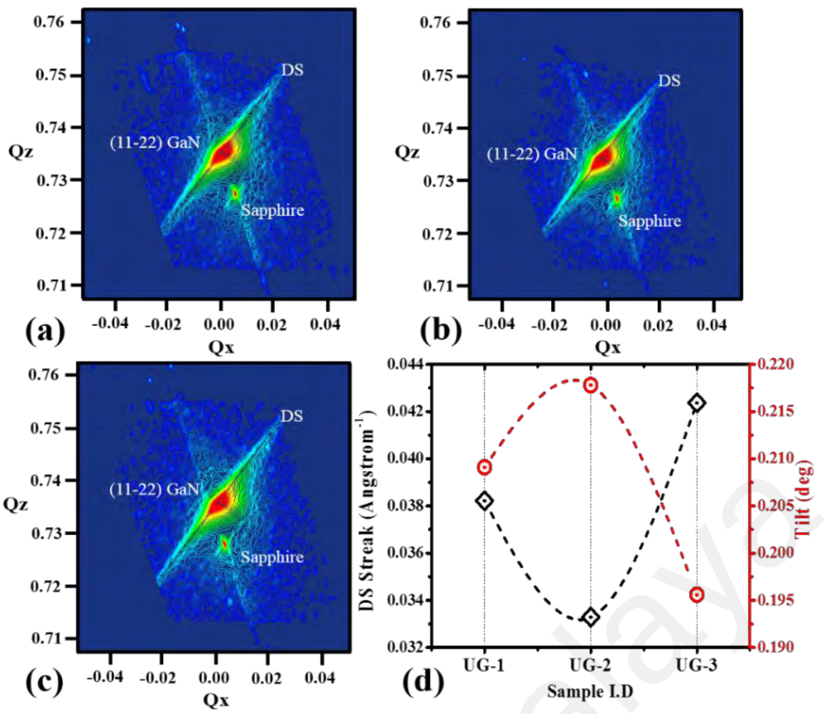


**Figure 4.6: XRD reciprocal space maps along [-1-123] of (a) UG-1, (b) UG-2 and (c) UG-3, and (d) the DS streak and tilt plot of the samples.**

Further analysis via RSM was conducted along the [-1-123] direction as shown in Figure 4.6. The RSM along [-1-123] have been reported to help further evaluate in detail the relaxation state of the epilayers and few defects estimation (Farrell et al., 2012; Young et al., 2010). From the figure, the main concern would surround the diffuse scattering (DS) streak elongated around the main GaN peak as well as the tilt between the sapphire and GaN peak. The DS streak exhibited by UG-2 was recorded to be the lowest compared with UG-1 and UG-3 with UG-2 possessing the highest tilt. UG-3 however, exhibit the longest DS streak elongation with lowest tilt. The DS streak elongation and tilts are as shown in Figure 4.6(d). Studies have shown that the DS streak corresponds to the existence of prismatic stacking faults (PSFs) whilst the tilt between the sapphire and GaN corresponds to the relaxation of the epilayers due to presence of misfit dislocations (MDs) (Farrell et al., 2012; Young et al., 2010). From the RSM analysis, it can be deduced that the use of excessive $NH_3$ flux during the growth of the Uid-GaN would promote the generation of PSFs. Low to intermediate $NH_3$ flux on the other hand exhibit slight differences in the PSFs presence. However, the tilt difference suggest higher relaxation state of the epilayers which might resulted from the presence of MDs with moderate $NH_3$ flux. It is known that the presence of MDs would help facilitate the relaxation of the epilayers (Smirnov et al., 2016; Tyagi et al., 2009).

### 4.2.3 Morphological Analysis of Uid-GaN with Optimized V/II ratio

Since the crystal analysis still exhibit low crystal quality as compared with other reported works (Sun et al., 2009b; Zhao et al., 2016), morphological properties should not deviate much from the common properties. Figure 4.7 depict the 2D and 3D AFM images of UG-2 at 10×10 μm and 0.5×0.5 μm scale with its respective line profiles. From Figure 4.7(a), the typical semi-polar morphological property is realized whereby the existence of highly undulated surface which constitutes towards the arrowhead-like features or also known as the fork-like ridges (Wernicke et al., 2008) as highlighted in red arrowhead-lines. The stacking/overlapping of the high density of the arrowheads causes the formation of deep elongated valleys as highlighted in blue circles. The average line profile extracted from the image exhibits the average peak to valley wherein the highest peak situated ~ 30 nm whilst the lowest valley at ~ -5 nm. Furthermore, the high densities of the arrowhead feature along with the heightened/deepened undulations gives rise to the considerably high surface root mean square (RMS) roughness of ~ 7.55 nm. It is well known, that semi-polar (11-22) GaN tends to portray such features in its surface morphology as a consequence of the defect propagations (Wu et al., 2017; Xu et al., 2012). Presumptions have been made as to higher density of such undulations would be in direct correlation with higher density of defects propagating within the epilayer towards its surface (Wu et al., 2017). Studies have also showed that such features are in direct correlation with the anisotropic growth direction in semi-polar (11-22) GaN (Ploch et al., 2012).

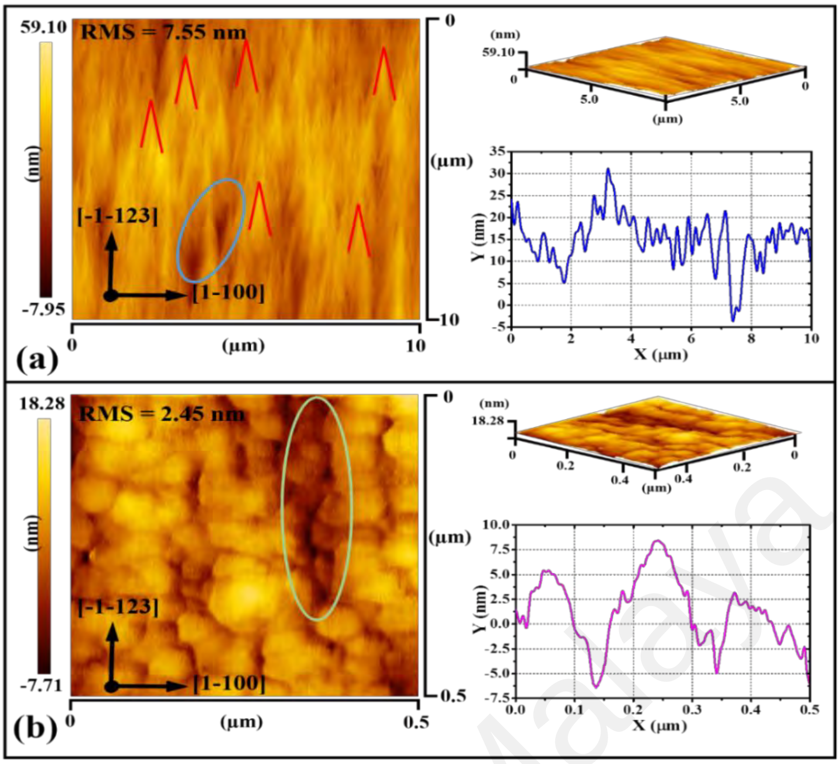


**Figure 4.7: (a) 10×10 μm and (b) 0.5×0.5 μm AFM images of UG-2 with its respective 3D image as well as the average line profile of the image.**

To unveil the origins of such features lower scan size of the AFM imaging was conducted as shown in Figure 4.7(b). From the figure, it can be deduced that the surface comprises of the commonly known atomic-sized terrace-step whereby in semi-polar GaN, such features exists mainly due the tilt formed prior to the epilayer growth (Strittmatter et al., 2011). It can be observed that a highly irregular terrace sizes and arrangements were exerted. The extracted average line profile reveals that the arrangement of terraces was rather random. Additionally, the terrace sizes are also randomly distributed revealing high density of large terraces inducing the elongated valley formations as highlighted in green circles. The peak-to-valley height/depth from the line profile is recorded to be ~ 8.5 nm and ~ -6.5 nm. Such arrangement/distribution along with the heightened peak-to-valley of the terrace-steps constitutes the formation of the aforementioned undulated arrowhead-like features. Previous works have shown that with a homogenously distributed terrace structures, the undulated arrowhead features was seen to be suppressed as a result of higher crystal quality (Baker et al., 2006). Further details on the matter will be discussed in the latter chapters.

The results indicate that an optimum $NH_3$ flux (0.7 slm) plays a huge role in attaining an optimum growth condition which leads to a better crystal. Higher $NH_3$ (1.0 slm) would endure abundance of N atoms which promotes N rich conditions wherein the growth of semi-polar (11-22) GaN, Ga rich conditions are more favored (Chèze et al., 2013). However, if the $NH_3$ flux falls below the threshold value of 0.7 slm, the growth of the epilayer is slightly disturbed as the available N atoms remains too low for Ga atoms to form the GaN structure. This leads to a slightly poorer crystal formation (UG-1)with increased defects generation (Sun et al., 2008).

### 4.3 Uid-GaN with AlN Nucleation Layer (NL)

As the growth of semi-polar (11-22) Uid-GaN epilayer was successfully achieved via the 1-step growth technique, acquiring a method of reducing the defects existence whilst enhancing the crystal quality is deemed necessary. The first step taken into consideration for such purpose includes an insertion of a thin AlN NL prior to the growth of the thick Uid-GaN epilayer. Such approach would help reducing the lattice mismatch between the sapphire substrate and the subsequent GaN epilayer (Dadgar et al., 2011). If successful growth of the Uid-GaN epilayer with an insertion of a thin AlN NL is to be realized, the growth optimization of the AlN NL is crucial.

#### 4.3.1 The Growth Conditions involved

In this work, the pre-optimization of the AlN NL was realized by varying the aluminum source flux which is the trimethylaluminum (TMA) with constant $NH_3$ flux of 2.3 slm, temperature of 1050°C, and pressure of 13.3kPa. The variation of the TMA was 50, 75, and 98.5 sccm which would yield the V/III ratio of 2527, 1684 and 1282, namely NL-1, NL-2 and NL-3 respectively. Figure 4.8 depicts the growth conditions of the samples, (a) substrate cleaning in $H_2$ ambience, (b) nitridation procedure, (c) growth of thin AlN NL and (d) growth of Uid-GaN epilayer.

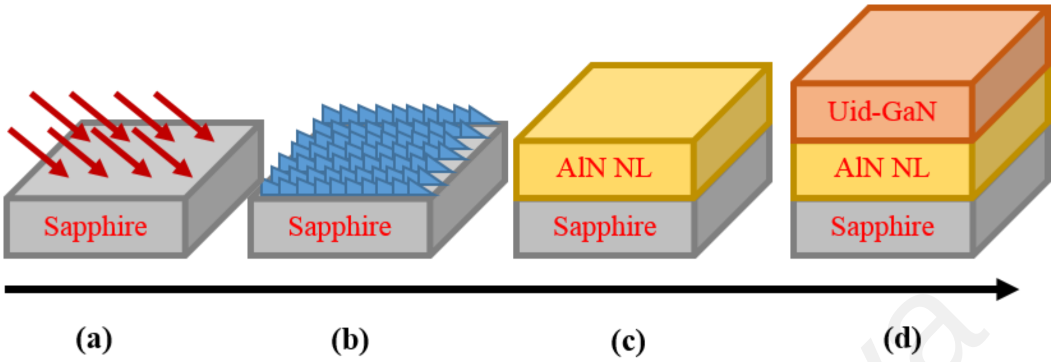


**Figure 4.8: Growth steps involved in the insertion/optimization of the AlN NL prior to the Uid-GaN epilayer.**

### 4.3.2 Crystal quality of the Uid-GaN impacted by the AlN NL

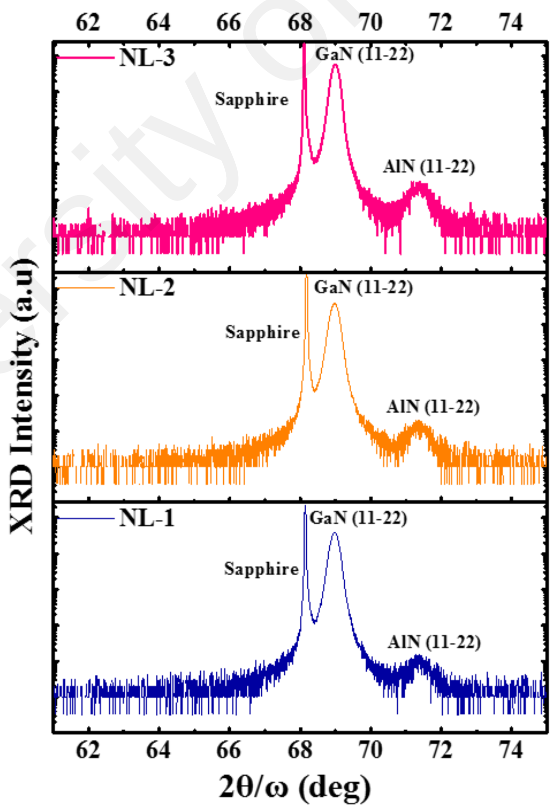


**Figure 4.9: HR-XRD, $2\theta/\omega$ scans of the Uid-GaN epilayers with various AlN NL optimizations**

$2\theta/\omega$ scan of the three AlN NL optimization is as shown in Figure 4.9. From the figure an additional peak is present for all sample indicating the presence of the thin AlN NL. Further additional peaks other than the sapphire and the GaN was observed absent illuminating no crystal evolution towards a polycrystalline crystallinity. All three samples exhibit predominant semi-polar (11-22) GaN and AlN peaks illuminating single crystallinity is achieved even upon the utilization of significantly dissimilar TMA flux within the AlN NL

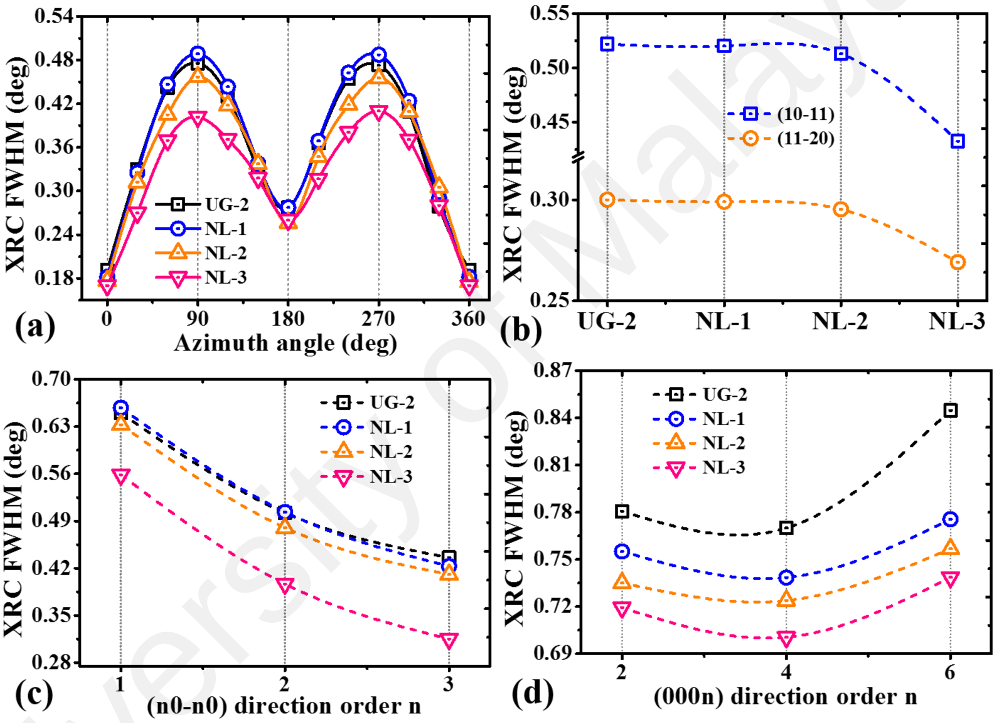


**Figure 4.10: XRC FWHMs of NL-1, NL-2, NL-3 as compared with UG-2 via (a) on-axis configuration and (b) off-axis configuration along (10-11) and (11-20), (c) the (n0-n0) series as a function of n and (d) the (000n) series as a function of n.**

Similar to the Uid-GaN optimization, on-axis XRC was implemented for crystal quality analysis as well as the anisotropic properties. Figure 4.10(a) presents the azimuthal dependence m-shaped FWHMs for all three NLs. From the figure, it can be deduced that the use of significantly high TMA flux (NL-3) yielded the lowest anisotropy with XRC FWHMs along [-1-123] and [1-100] was observed to be around 0.17° (612 arcsec) and 0.40° (1440 arcsec) respectively. However, low (NL-1) and intermediate (NL-2) TMA flux yielded similar anisotropy behavior exhibiting FWHMs along [-1-123] and [1-100] around 0.18° (648 arcsec) and 0.48° (1728 arcsec) respectively. Furthermore, comparison with the previous UG-2 reveals the immense reduction of the anisotropy exhibited by NL-3 whilst NL-2 portrayed a slight reduction along [1-100] compared to UG-2. Only NL-1 exhibited a small increase in the anisotropy as the FWHM along [1-100] was slightly higher than UG-2. The on-axis XRC analysis suggest that with an optimum growth of an AlN NL, a reduction in anisotropy of the subsequent GaN epilayer would be achieved.

Off axis XRCs analysis reveals similar trends as the on axis suggesting better crystal quality exerted by NL-3 as compared with NL-1 and NL-2 as shown in Figure 4.10(b-d). The diffraction planes along the (10-11) and (11-20) portrayed similar FWHMs for NL-1 and NL-2 with significantly low FWHM for NL-3. This illuminate's lower presence of PSFs with the use of higher TMA flux as compared with lower TMA flux during the NL growth. The (n0-n0) diffraction directions as in Figure 4.10 (c) also shows that the use of highest TMA flux would endure the lowest presence of BSFs of both type $I_1$ and $I_2$ as the XRC FWHMs for NL-3 exhibited the lowest values as compared with NL-1 and NL-2. However, slight variations were observed in the (000n) directions as in Figure 4.10(d) whereby NL-1 and NL-2 exhibited rather large differences in the FWHMs broadening. Such occurrence indicates variant partial and/or perfect dislocation existence between all three samples. On the other hand, further comparison with UG-2 elucidates significant reduction of the BSFs and PSFs upon the insertion of an optimized AlN NL with higher TMA flux (NL-3). Conversely, the use of low-to-intermediate TMA flux (NL-1 and NL-2) did not show any significant narrowing of the XRC FWHM along (10-11) and (11-20) as well as the (n0-n0) series igniting low to none reduction of the BSFs and PSFs presence. However, the (000n) series portrayed a slight dissimilar trend wherein even with the highest V/III ratio of 2527 (NL-1), considerable narrowing in the XRC FWHMs were recorded followed by NL-2 and finally NL-3. The trend suggests the reduction of partial and/or perfect dislocation having a c-axis component was attained with the insertion of the AlN NL. Furthermore, the increment in the TMA flux would endure higher degree of narrowing in the FWHM of the (000n) series igniting lowest presence of partial and/or perfect dislocation with a c-axis component.

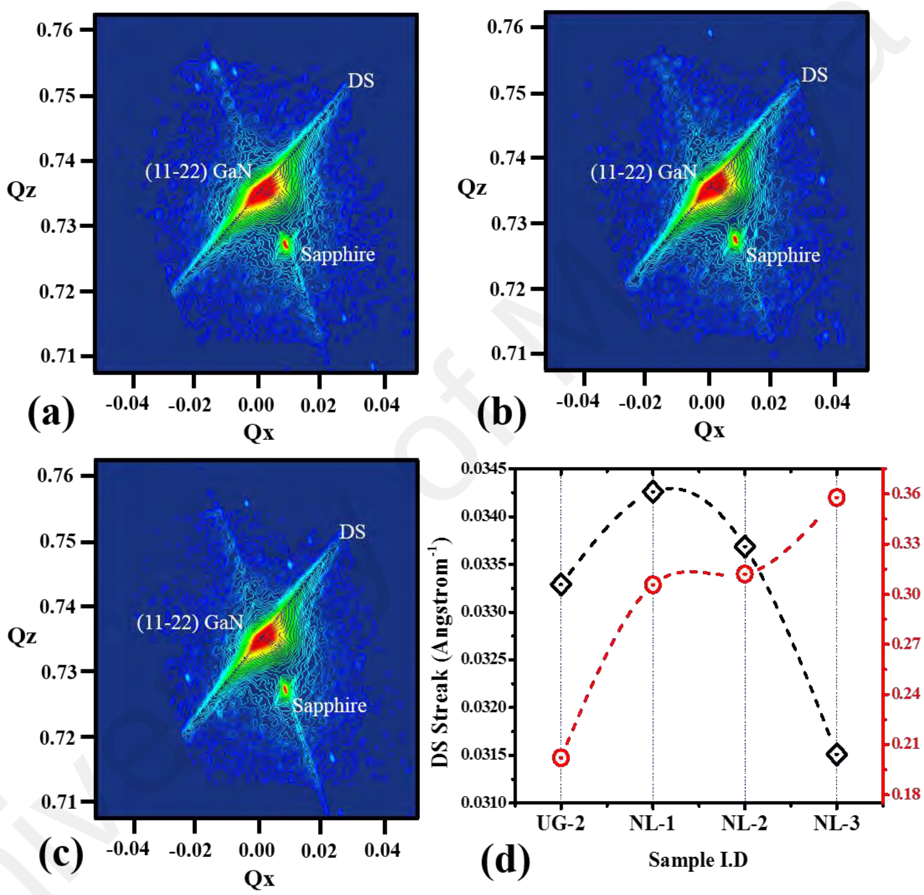


**Figure 4.11: XRD reciprocal space maps along [-1-123] of (a) NL-1, (b) NL-2, (c) NL-3, and (d) the DS streak and tilts plots for all NL optimizations including the previous Uid-GaN optimization (UG-2).**

Additionally, on axis RSMs measurement along [-1-123] supports further the XRC measurements as shown in Figure 4.11 with the DS streak elongation and tilt between the sapphire and GaN plotted in Figure 4.11 (d). The DS streak for NL-1 portrayed the longest elongation followed closely by NL-2 and finally NL-3 suggesting PSF abundance in low

TMA flux. After increasing the TMA flux to 75 sccm (NL-2), the DS streaks slightly shrinks indicating lower PSFs formation and further increasing the TMA flux to the highest available (NL-3) reduced the PSFs generation significantly. The tilt however showed progressive increment with increasing TMA flux. Comparison of the DS streaks and tilts with the previous UG-2 was further analyzed in the corresponding plot as in Figure 4.11 (d). The DS streak was further elongated from UG-2 to NL-1 and slightly elongated in NL-2, whilst significantly suppressed in NL-3. The tilt however, portrayed a sudden increase in NL-1 from UG-2 and further higher degree of tilt was recorded upon comparing NL-3 to UG-2. Such phenomenon indicates higher degree of relaxation was realized with the insertion of AlN NL. Additionally, the RSMs follows the XRCs trend illuminating better crystallinity was achieved with the use of higher TMA flux (NL-3).

### 4.3.3 Morphological analysis of the Uid-GaN with Pre-Optimized AlN NL

Similar to the previous optimization of the Uid-GaN, surface morphology analysis of NL-3 via AFM was conducted to reveal the surface property of the Uid-GaN epilayer with the presence of an optimized AlN NL. Figure 4.12 (a) presents the 2D and 3D 10×10 μm AFM scan of the surface revealing similar features with the previous UG-2 with few slight differences. Analysis interpreted from the image reveals slight decrement in the density of the arrowhead-like features as labeled with the red arrowhead lines. The intense dark regions corresponding to the deep elongated valley formations observed in the previous UG-2 have been lowered in height (as highlighted in blue circles). Details of the features taken from the average line profile of the AFM illuminates that the peak to valley heights/depths was ~28 nm which exhibited ~7 nm reduction as compared with the previous UG-2. This results in the lowering of the undulation-induced arrowheads homogeneously distributed along the surface. Such occurrence constitutes the lowering of the surface RMS roughness to 6.05 nm as oppose to 7.55 nm exhibited by the UG-2.

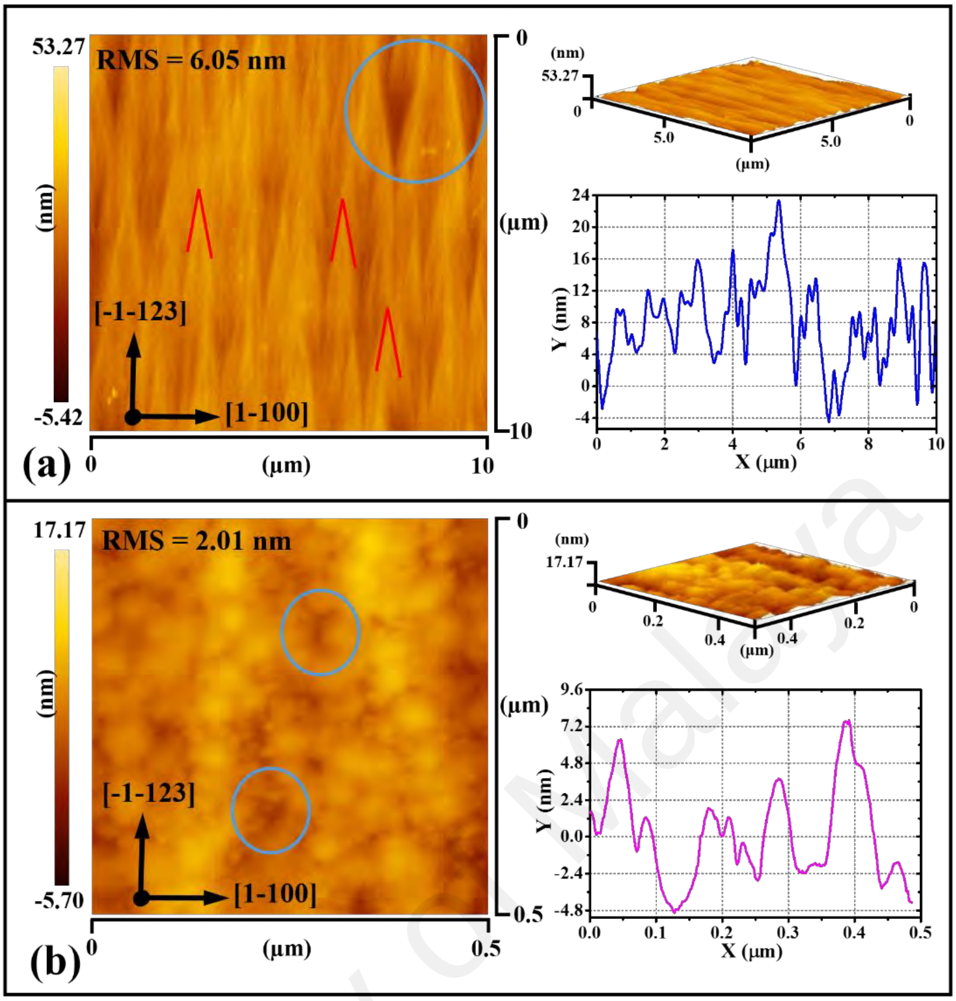


**Figure 4.12: (a) 10×10 µm and (b) 0.5×0.5 µm AFM images of NL-3 with its respective 3D image as well as the average line profile of the image.**

Figure 4.12(b) depicts the 2D and 3D 0.5×0.5 µm AFM scans which further supports the higher scans deducing lower surface RMS roughness of 2.01 nm compared to 2.46 nm possessed by the UG-2. The average line profile also detects the reduced terrace-steps sizes with lower peak to valley height/depth. Arrangement of the terrace-steps was also seen more homogeneously distributed with the presence of the optimized AlN NL. The occurrence of such rearrangement in terrace-steps would be correlated with the larger scan sizes AFMs where it constitutes better surface morphology with lower density of undulations as well as the arrowhead-like features.

The analysis indicates that the insertion of an AlN NL would significantly impact the subsequent Uid-GaN epilayer in crystal and morphological properties. Similar to the nitridation process, the AlN/AlON protrusions generated would facilitate a reduction of the lattice mismatch between the sapphire and GaN epilayer as AlN exhibit closer lattice similarities with $Al_2O_3$ compared with GaN (Dadgar et al., 2011; Lahourcade et al., 2007; Wang et al., 2017). Further, complementing the AlN nano-sized protrusions with the thin AlN NL would be further beneficial where lower defect generation could be realized (Davidsson et al., 2005). It is known that the additional AlN NL would also form an interface between the AlN and GaN epilayer. This interface would benefit the subsequent GaN epilayer as a defect reduction technique where generation of MDs might occur which aids the elimination of few defects and dislocations (Dadgar et al., 2011).

However, consideration of the AlN growth conditions needs to be taken as studies have shown the possibilities of twinned-growth formation of the AlN due to different causes (Mogilatenko et al., 2014; Sun et al., 2009b). The growth in a vertical MOCVD systems have shown the use of significantly higher V/III ratios would aid in suppressing the twinned-grain formations resulting in the dominance of (11-22) orientation (Mogilatenko et al., 2014). Henceforth, none of the grown samples were below the V/III ratio of 1000 (NG-1 = 2200, NG-2 = 1570). Even so, there exists a threshold value of how high the V/III can be raised without crystal deterioration. As all the TMA variations did not exhibit mixed oriented growth of (10-13) or (10-10), it would seem that the V/III ratio of ~1282 would be highest by which the subsequent GaN epilayer crystal quality was not deteriorated. Further lowering the TMA flux to 70 or 50 sccm (for higher V/III ratio) would prove to disintegrate the crystal enhancement exhibiting larger anisotropy as well as defects generations. If the AlN NL possess better quality, then the subsequent GaN epilayer will be structurally enhanced (Sun et al., 2009b).

# CHAPTER 5: IMPLEMENTING DEFECT REDUCTION TECHNIQUES

As the optimization of the Uid-GaN with and without AlN NL epilayers were completed, further employing additional technique for surface and crystal quality enhancement is deemed necessary as it is still well below the acceptable quality for any device application. In this part of the chapter, phase II of the work is discussed wherein the implementation of in-situ single and multiple ammonia gas pre-treatment is realized prior to the growth of the thick Uid-GaN epilayer. Finally, an insertion of strained periodic alternating multilayers prior to the growth of the Uid-GaN epilayer is further implemented and compared with the earlier in-situ defect reduction techniques. This chapter will discuss the why and how such techniques were implemented as well as the resulting outcome towards the crystal and morphological qualities of the subsequent Uid-GaN epilayers.

## 5.1 Single Ammonia ($NH_3$) inter-treatment

The first part of Phase II involves implementing a pre-treatment of a thin GaN epilayer surface post-growth of the AlN NL prior to the Uid-GaN growth. The pre-treatment step includes the use of ammonia gas ($NH_3$) with a controlled flow density. In principle, the presence of $NH_3$ during the growth interruption would induce an etching phenomenon around a lower bounded energy dislocation site. Such occurrence should facilitate the enhancement of the crystal quality as well as morphological property. However, the parameters used during the $NH_3$ treatment should be optimized for realization of such purposes.

### 5.1.1 The Growth Conditions Involved

Similar to the previous chapter, the growth of the pre-optimized Uid-GaN and AlN NL is maintained with the use of same temperature (1050 °C), pressure (13.3 kPa) and MO source flux (TMG = 60 sccm and TMA = 98.5 sccm). All the growth conditions were kept constant with variations only with the treatment time of 60, 180 and 360 seconds designated as ST-1, ST-2, and ST-3. Figure 5.1 depicts the schematic illustration of steps involved during the growth. (a) Substrate cleaning in $H_2$ ambience, (b) nitridation procedure, (c) growth of AlN NL, (d) growth of thin GaN layer (~20 nm) prior to the $NH_3$ treatment, and (e) Uid-GaN deposition. It should be noted that since all the growth conditions were kept constant except for the $NH_3$ treatment, hence all the resulting outcome is directly impacted by the treatment time.

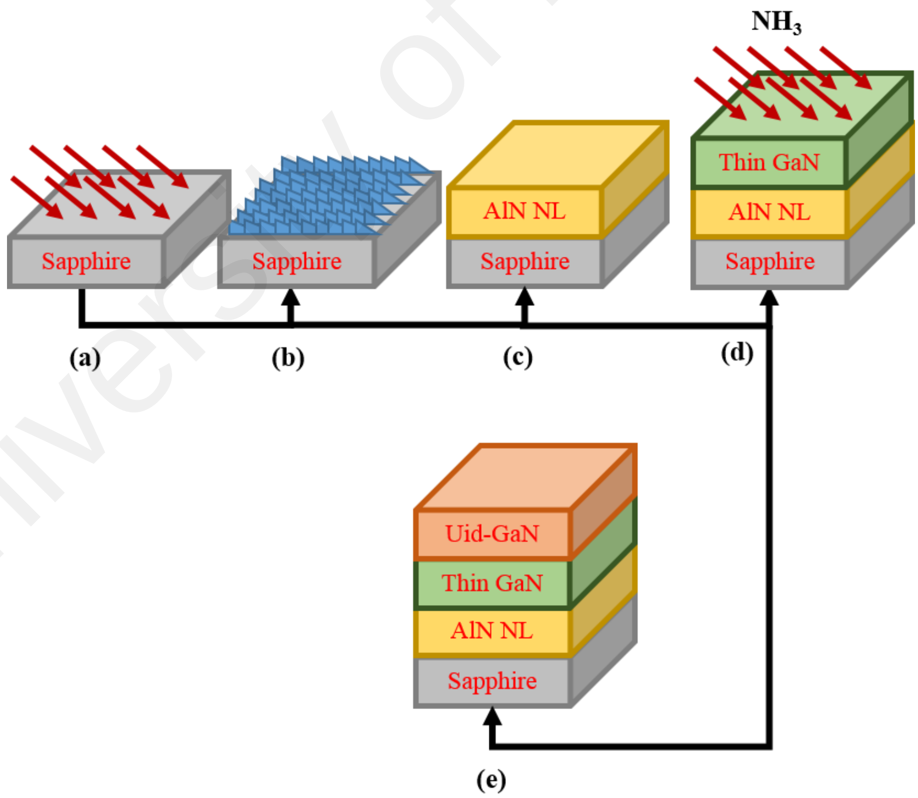


**Figure 5.1: Growth steps involved during the growth of Uid-GaN with an in-situ single ammonia treatment.**

### 5.1.2 Impact of $NH_3$ treatment on the Crystal quality of the Uid-GaN

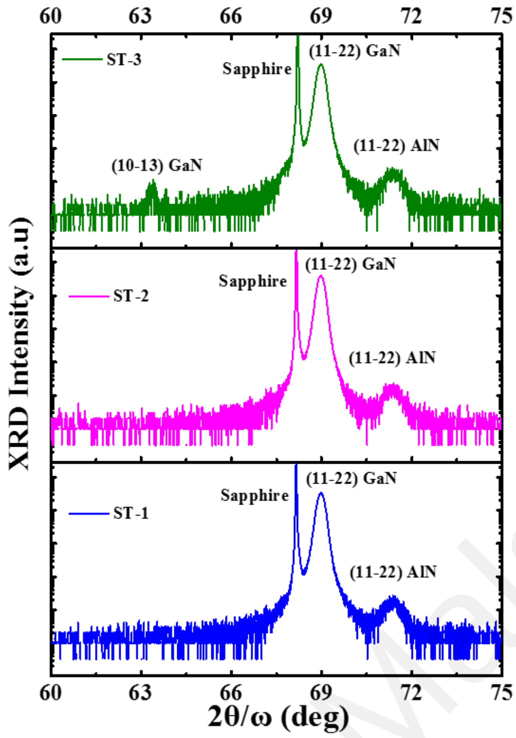


**Figure 5.2: HR-XRD, $2\theta/\omega$ scans of the Uid-GaN epilayers with various single ammonia treatment optimizations**

Since all the procedure implemented including nitridation, AlN NL growth, and Uid-GaN growth was kept constant, the crystal quality is solely impacted by the $NH_3$ treatment wherein short to long treatment time would be the cause of crystal quality variation. Figure 5.2 presents the $2\theta/\omega$ scans sample ST-1, ST-2 and ST-3. It is obvious, that no crystal orientation deviation occurred either at short or intermediate duration of $NH_3$ treatments (ST-1 and ST-2). It was recorded that the predominant peaks corresponding to the (11-22) GaN and AlN along with the sapphire peak were clearly present. However, upon realizing the longer duration of treatment to 360 seconds, a small peak which corresponds to the (10-13) semi-polar orientation immerges, indicating crystal degradation. The $2\theta/\omega$ scan indicates that the use of excessive $NH_3$ treatment with a lengthy duration of 360 seconds would revert back the dominance of the (11-22) growth orientation. This in turn, promotes a polycrystalline GaN orientations which might be resulted from a twinned-growth condition (Dinh et al., 2015). Such occurrence might be due to the over-exposure of the initial GaN layer with the reactive $NH_3$ gases at elevated temperature, inducing excessive etching of the surface resulting in a 3D growth prior to the subsequent Uid-GaN growth (Song et al., 2013). In order to reveal such matter, further analysis was conducted to determine the crystal quality enhancement/degradation of such techniques towards the subsequent Uid-GaN epilayer.

Similar to previous chapters, on-axis XRC was first observed to analyze the anisotropic behavior of the Uid-GaN epilayers with various $NH_3$ treatment durations with comparisons against UG-2 and NL-3 as shown in Figure 5.3 (a). From the figure it can be seen that ST-2 possess the lowest FWHMs along both [-1-123] and [1-100] of 0.207° (745 arcsec) and 0.530° (1908 arcsec), respectively, followed closely by ST-1. ST-3 on the other hand exhibited the highest anisotropy with FWHM broadenings along [-1-123] and [1-100] of 0.240° (864 arcsec) and 0.587° (2113 arcsec), respectively. The results indicates that an intermediate duration of the $NH_3$ single treatment would endure better anisotropic property compared with short and long treatment duration. However, either shorter or longer durations of $NH_3$ treatment exhibit any enhanced anisotropic properties as compared to UG-2. Only ST-2 exhibited close anisotropy with UG-2. Further comparison with NL-3 showed even greater anisotropic properties for all $NH_3$ treatment samples. FWHMs along both [-1-123] and [1-100] showed immense broadening of all $NH_3$ treatment samples as depicted in Figure 5.3 (a). NL-3 still exhibit superior FHWM narrowing in both directions indicating that the use of such treatment would not enhance but worsened the anisotropy. This is presumed to be caused by the increased defect generation/propagation post-treatment prior to the Uid-GaN epilayer. In order to confirm such occurrence, off-axis XRCs was implemented.

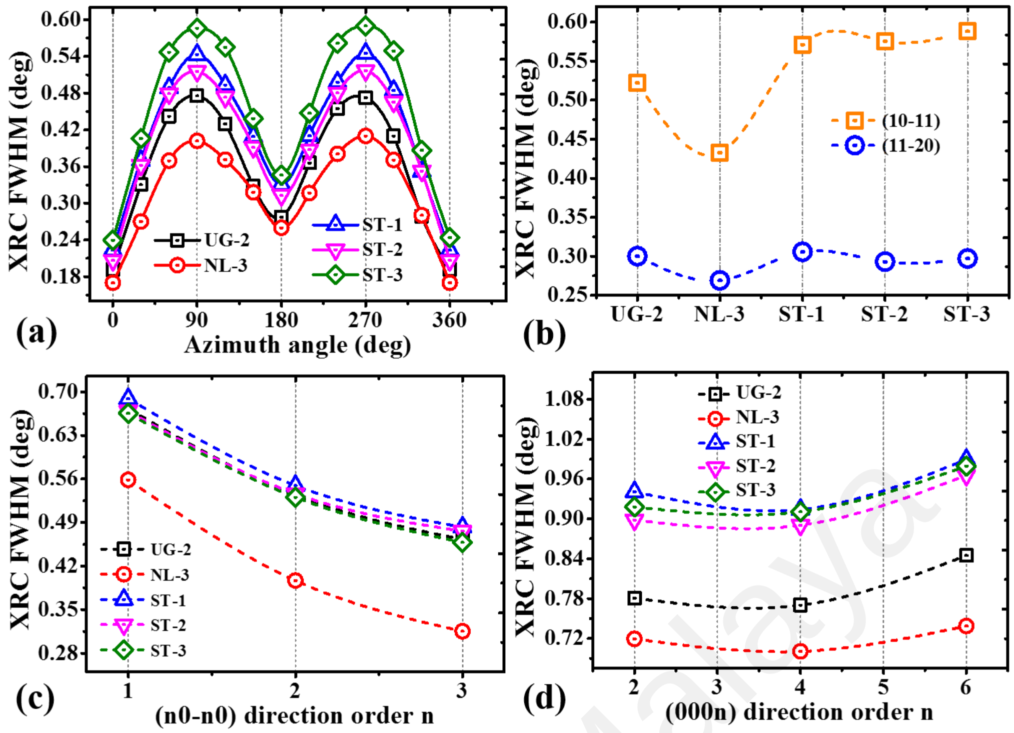


**Figure 5.3: XRC FWHMs of all single ammonia treatments with comparison with the previous optimized UG-2 and NL-3 via (a) on-axis configuration and (b) off-axis configuration along (10-11) and (11-20), (c) the (n0-n0) series and (d) the (000n) series.**

Figure 5.3(b-d) presents the off-axis XRCs for all $NH_3$ treatment samples including UG-2 and NL-3. The off-axis measurements reveals similar trends with the on-axis XRC. However, few variations can be observed from the (n0-n0) directions. From Figure 5.3(b), all three $NH_3$ treatments exhibits similar FWHMs along (10-11) and (11-20) with slight reductions upon increasing the treatment time from 60s to 180s and 360s. Despite such reduction, none of them showed lower FWHM broadenings compared with NL-3. This indicates higher existence of perfect dislocations and PSFs as the Uid-GaN epilayer undergone the single $NH_3$ treatment. The XRCs along (n0-n0) direction on the other hand, yet still unable to surpass the NL-3 FWHM exhibit similar values to the UG-2 as seen in Figure 5.3(c). Such trend reveals the occurrence of BSFs regeneration within the Uid-GaN epilayer post-treatment. Partial and/or perfect dislocations having a c-axis component was also seen to increase with the $NH_3$ treatment wherein the XRC FWHMs in the (000n) series was immensely broadened as compared to NL-3 and UG-2 as in

Figure 5.3(d). All the off-axis XRC suggests crystal quality degradation with $NH_3$ treatment implemented post nucleation layer growth prior to the Uid-GaN epilayer growth.

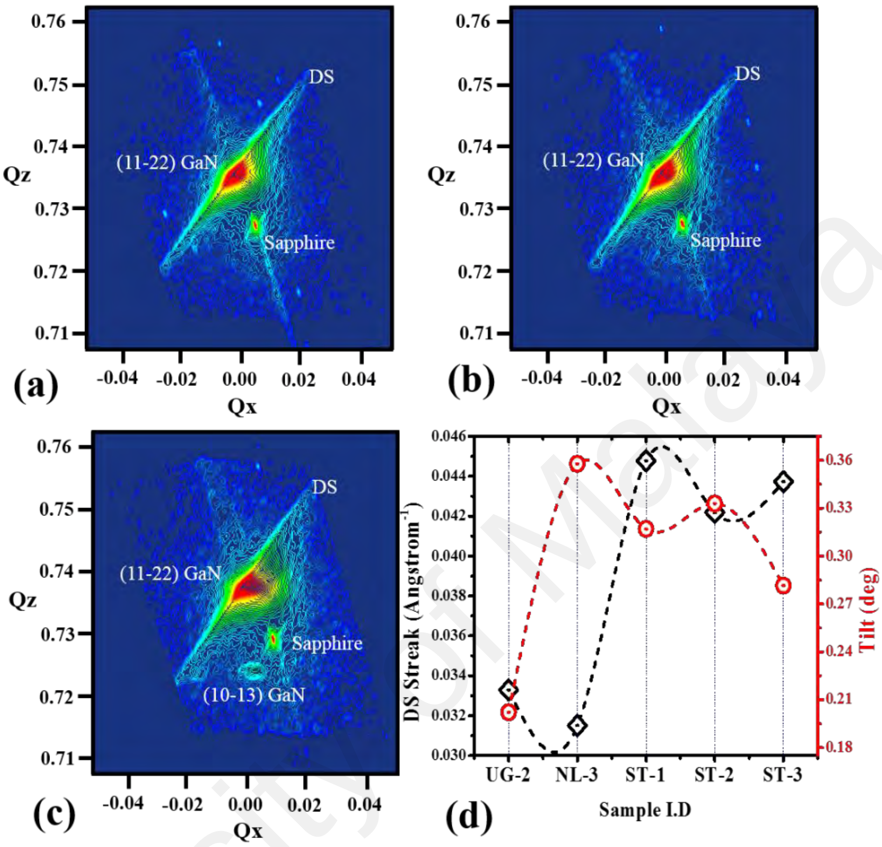


**Figure 5.4: XRD reciprocal space maps along [-1-123] of (a) ST-1, (b) ST-2, (c) ST-3 and (d) the DS streak and tilt plot of all ST samples in comparison with UG-2 and NL-3.**

Further confirming the results is illuminated in the RSMs measurement along the [-1-123] as shown in Figure 5.4. The RSM reveals slight differences between ST-1 and ST-2 where the DS streak in ST-2 is shorter and ST-1 exhibited a slightly elongated DS streak as plotted in Figure 5.4(d). ST-3 however, possess the longest DS elongation igniting the crystal degradation with increased PSFs presences. Furthermore, the sapphire (10-13) peak immerges in ST-3 further supporting the XRD, which suggest a deterioration with formation of polycrystalline oriented Uid-GaN epilayer was grown due to the elongated duration of the $NH_3$ treatment.  In addition, the tilt between the sapphire peak and (11-

22) GaN was highest for ST-2 and lowest in ST-3 suggesting the intermediate flow of $NH_3$ during the treatment would exert the higher degree of relaxation compared with the short and long durations. Further comparison with UG-2 and NL-3 reveals significantly elongated DS streaks exhibited by all ST samples. However, the tilt exhibited by ST samples were enhanced compared with UG-2, yet still lower than NL-3. The RSM supports the XRC analysis whereby the trend parallels signifying crystal deterioration of the samples upon the use of the single ammonia treatment technique.

### 5.1.3 Surface Morphology of Uid-GaN with Pre-Optimized $NH_3$ treatment

Even though the crystal quality of the samples remains too low compared with samples without the $NH_3$ treatments, morphological analysis still remains necessary as the $NH_3$ treatment might have significant impact on the surface morphology as few studies have reported on such phenomenon (Song et al., 2013). Figure 5.5(a) presents the 10×10 μm 2D and 3D AFM images of ST-2 as it possesses the highest crystal quality among the ST samples. Significant densities of striations could be observed resembling the aforementioned arrowhead-like features as in NL-3 and UG-2. Despite that, the width of the arrowhead features has significantly narrowed as labeled with the red arrowhead lines. 3D image further confirms such phenomenon indicating an evolution of the surface morphology. Since narrowing of the width occurred, the density of such features evidently increased within the same scale (compared with UG-2 and NL-3 10×10 μm scan size). The narrowing of the arrowhead-features resulted in the shortening of the undulation distances constituting a compact undulated arrowhead-features. Such phenomenon leads to the formation of narrow elongated valleys (as highlighted in blue circles) inducing the lowering of the peak-to-valley heights/depth. Based on the average line profile, the highest peak was ~18.43 nm and ~1.45 nm for the lowest valley resulting in significantly lower surface roughness as compared to UG-2 and NL-3. The measured surface RMS roughness was seen to reduce to ~ 5.92 nm. Even so, the low RMS roughness cannot be directly correlated with the crystal quality. This might be attributed to the enhanced dislocations propagations or generations of new dislocations upon the growth of the subsequent GaN epilayer as observed in the XRCs.

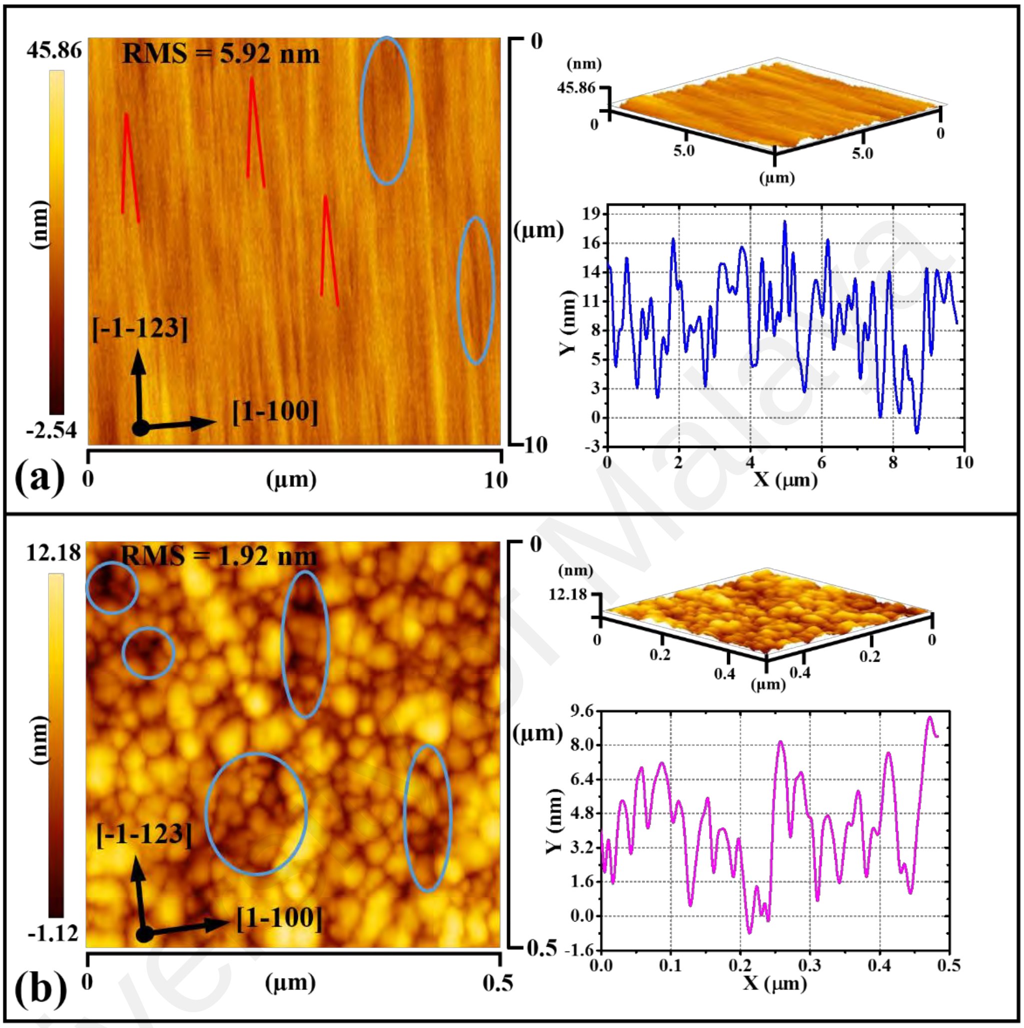


**Figure 5.5: (a) 10×10 µm and (b) 0.5×0.5 µm AFM images of ST-2 with its respective 3D image as well as the average line profile of the image.**

Lower AFM scan size of 0.5×0.5µm was also implemented to determine the arrangement of the terrace-steps as shown in Figure 5.5 (b). It can be deduced from the figure that the use of the single $NH_3$ treatment would significantly alter the terrace-steps sizes and arrangement. The terrace size distribution was observed to favor smaller terrace-sizes compared with larger terrace sizes. Compared with the previous UG-2 and NL-3, the terrace-steps arrangements were significantly transitioned where the terrace arrangement portrayed a more compact arrangement due to the homogeneously distributed smaller terrace-sizes. Consequently, only few narrow-deep valleys were present compared with the broad-deep valleys exhibited by UG-2 and NL-3. Such occurrence causes the narrowing of the arrowhead-like features inducing lower RMS roughness.

Based on previous studies, the use of $NH_3$ as an approach to reduce defects densities would be beneficial. However, it is clearly observed that from this work such presumptions might be overstated, or certain parameters used could differ as the defect densities were not significantly reduced. It is known that such approach utilizes the $NH_3$ for etching purposes due to the high reactivity of the $NH_3$ precursors at elevated temperatures with GaN, specifically near dislocation sites with lower thermal instability (Hsu et al., 2011; Song et al., 2013; Weyher et al., 2009). The etched surface would then induce a disfigured dislocation site which would not further continue to the subsequent Uid-GaN epilayer (Weyher et al., 2009). Despite that, such etching might not have occurred optimally with the conditions provided above with only deterioration of the crystal quality was observed. Even with short or long durations of $NH_3$ treatment time crystal quality remains low. However, the $NH_3$ treatment showed significant improvement of the surface elucidating favorable conditions of the $NH_3$ towards the arrowhead-like features. Even so, the lower AFM scan sizes reveals a sharp narrow-deep valley elongation was formed. This supports the crystal quality analysis where it is presumed that with single $NH_3$ treatment, the defects densities were significantly enhanced to a higher degree of existence. Furthermore, the longer duration of the $NH_3$ treatment time, further crystal degradation with twinned-grain growth orientations would be realized.

## 5.2 Multiple Ammonia ($NH_3$) inter-treatment

As the single treatment approach did exhibit significant morphological evolution without crystal enhancement, it would be beneficial to address the issues simultaneously. This might be achievable via altering the treatment parameters such as incorporating alternating treatments with thin GaN layers as appose to the single treatment. In this part of the work, the use of multiple $NH_3$ inter-treatments is demonstrated with its impact on crystal and morphological qualities elucidated.

### 5.2.1 The Growth Conditions involved

The second part of Phase II utilizes the single treatment with $NH_3$ parameter with slight differences whereby the use of single and long duration of the treatment was replaced by a multiple $NH_3$ treatment (MT) step. All the rest of the growth conditions such as nitridation, AlN NL and Uid-GaN were maintained as before with temperature of 1050 °C, pressure of 13.3 kPa and MO source flux (TMG = 60 sccm and TMA = 98.5 sccm). The multiple $NH_3$ treatment consists of short duration of $NH_3$ flux of 6.0s (with flux of 1 slm), alternated with thin GaN growth (same growth conditions as the Uid-GaN epilayer with shorter time) for various periods of alternations. The growth conditions are as in Figure 5.6: (a) substrate cleaning in $H_2$ ambience, (b) nitridation procedure, (c) growth of AlN NL, (d) multiple $NH_3$ treatment, and (e) Uid-GaN deposition. The variation of the number of $NH_3$ treatments consists of 20, 40 and 60 alternates designated as MT-1, MT-2 and MT-3.

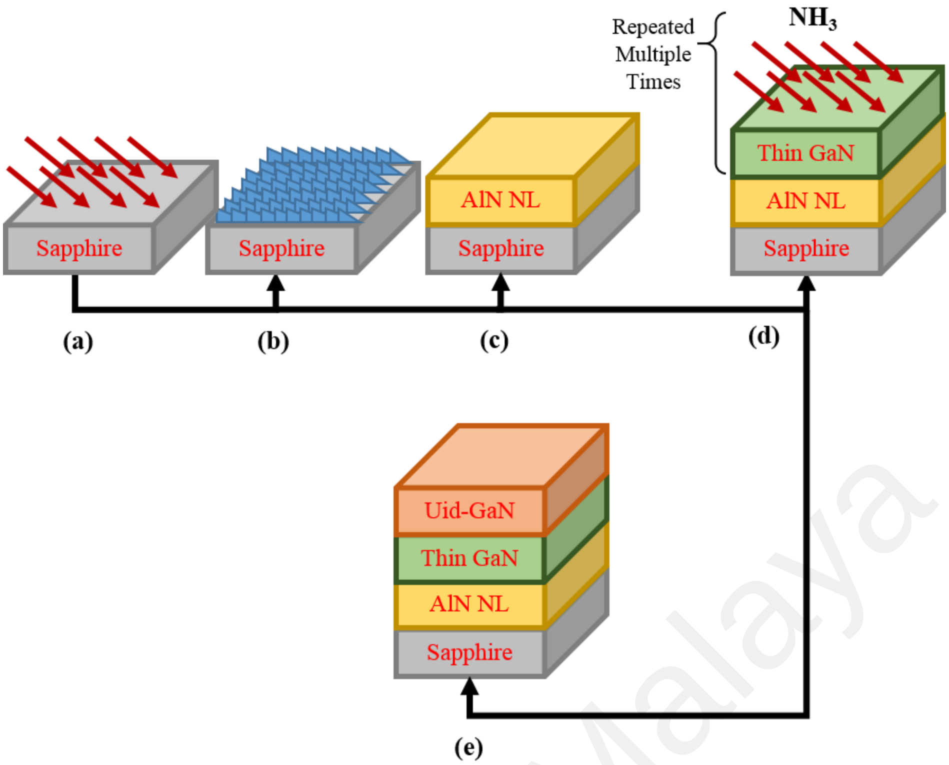


**Figure 5.6: Growth steps involved during the growth of Uid-GaN with an in-situ multiple ammonia treatment.**



### 5.2.2 Impact of $NH_3$ Treatment on the Crystal Quality of the Uid-GaN

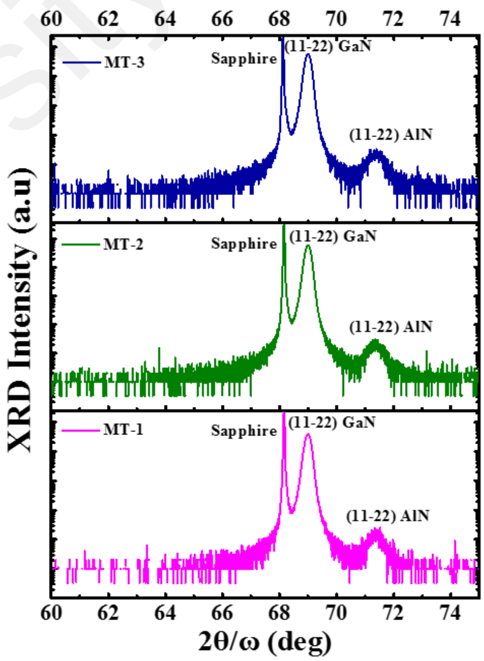


**Figure 5.7: HR-XRD, 2*θ*/*ω* scans of the Uid-GaN epilayers with various inter-multiple ammonia treatment optimizations**

Each steps of the growth since the beginning utilizes $2\theta/\omega$ scans to first identify the growth orientation as to avoid deviating from the desired (11-22) semi-polar GaN orientation as the extensive use of the $NH_3$ treatments conducted previously exhibit significant alteration in the crystal orientation. Figure 5.7 depicts the $2\theta/\omega$ scans which confirms no alteration in the growth direction occurred for all alternations of 20, 40, and 40, (MT-1, MT-2 and MT-3 respectively). Only presence of the sapphire, semi-polar (11-22) GaN and AlN were present with no trace of the (10-13) semi-polar GaN orientation. The scans indicate that by altering the $NH_3$ treatment approach, deviation of the crystal growth direction can be avoided.

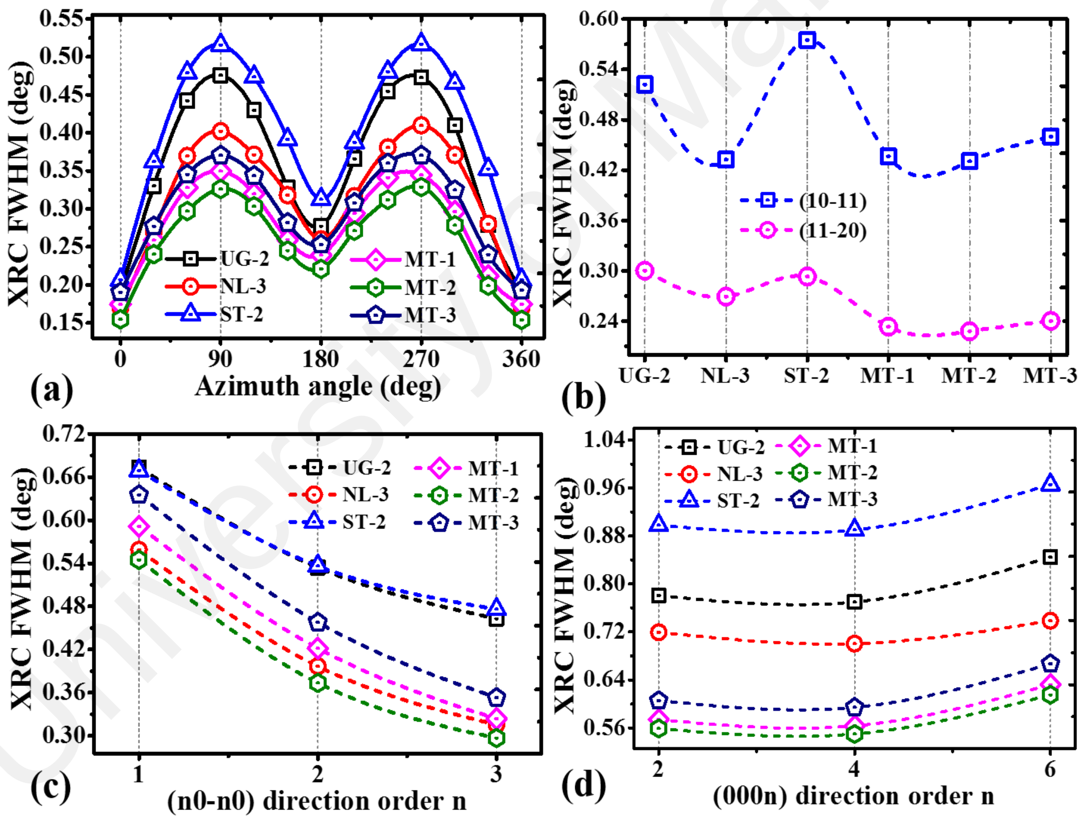


**Figure 5.8: XRC FWHMs of all inter-multiple ammonia treatments with comparison with the previous optimized UG-2, NL-3 and ST-2 via (a) on-axis configuration, (b) off-axis configuration along (10-11) and (11-20), (c) the (n0-n0) series and (d) the (000n) series.**

Anisotropic properties of the samples with comparison with previous samples UG-2, NL-3 and ST-2 were further evaluated via on-axis XRC similar to previous chapters is as shown in Figure 5.8(a). The lowest anisotropic property of the Uid-GaN epilayer was observed for MT-2 (40 alternates) compared with MT-1 and MT-3. The XRC FWHMs for MT-2 along [-1-123] and [1-100] was found to be around 0.15° (540 arcsec) and 0.33° (1188 arcsec) respectively. MT-3 exhibit the least reduction of anisotropic property followed by MT-1. Such progressive reduction indicates an optimum multiple treatment parameter can be realized with intermediate alternates compared with lower (20 alternates) or higher alternates (60 alternates). Compared with ST-2, all MT samples exhibits significant reduction in the anisotropy indicating enhanced crystallinity compared with the single yet longer treatment time. In addition, the multiple treatments also exhibit anisotropic properties enhancement significantly compared with UG-2 and NL-3, wherein the single treatment did not show any anisotropic improvement. The m-shaped azimuthal dependence spectrum suggests that the multiple $NH_3$ treatments would indeed help inducing better overall crystal quality.

Detailed analysis via off-axis XRCs is depicted in Figure 5.8(b-d) with UG-2 and NL-3 values included. Figure 5.8(a) depicts the XRC FWHMs for both (10-11) and (11-20) diffraction planes wherein MT-2 exerting the lowest FWHM broadening followed closely by MT-1 and MT-3. This suggest lower PSFs and perfect dislocation presence in MT-2 compared with MT-1 and MT-3. Despite that, comparison with NL-3 and UG-2 showed immense reduction along both direction for MT-2 revealing the multiple NH3 treatment would aid in reducing the PSFs and perfect dislocations. The BSFs qualitative estimation however, portrayed a different trend as depicted in the (n0-n0) series as in Figure 5.8(c). All the MT samples exhibit enhancement compared with UG-2 and ST-2. Yet still unable to progressively reduce the BSFs illuminating the fact that the multiple $NH_3$ treatments could not overcome the BSFs propagation greatly either with lower or higher number of alternates. Only MT-2 exhibit a slight reduction of the FWHM of compared with NL-3 whilst MT-1 and MT-3 both exhibit broader FWHMs than NL-3. The (000n) series as in Figure 5.8(d) on the other hand presents significant narrowing in the FWHMs for all MT samples compared with NL-3 with MT-2 portraying the lowest FWHMs. The off-axis analysis suggest certain defects propagations would be lowered with the use of the multiple $NH_3$ treatment including PSFs, partial and/or perfect dislocation having a c-axis component. Furthermore, a direct comparison of all the MT samples with ST-2 reveals that by applying short duration of $NH_3$ treatments alternating with thin GaN interlayers as oppose to single-long duration of $NH_3$ treatment would significantly aids certain defect propagation reduction. It would seem that the XRC FWHM broadenings were significantly lower in the MT samples compared with the ST samples.

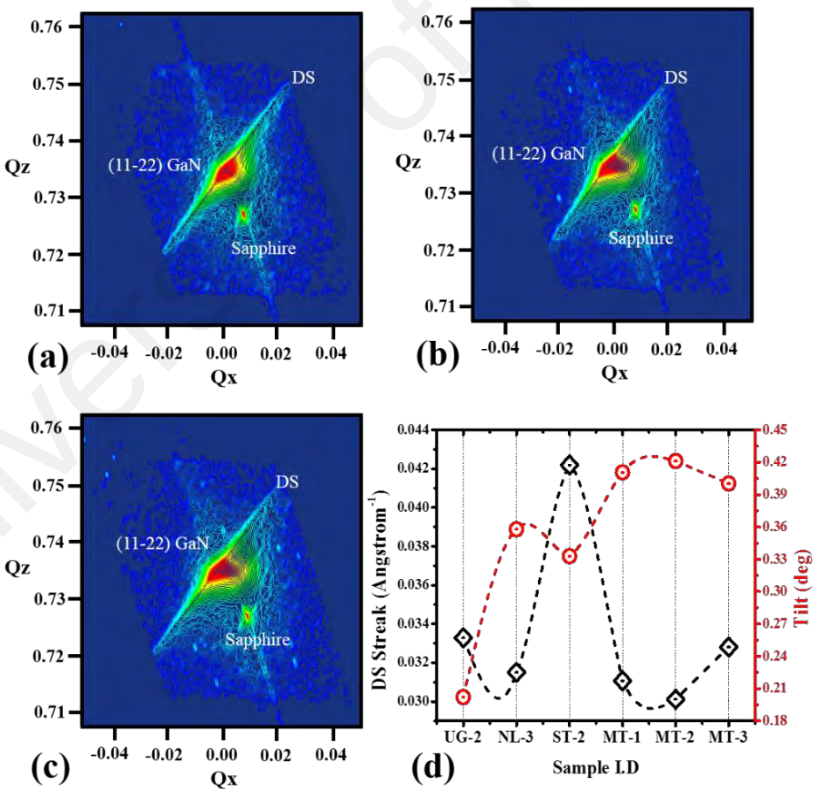


**Figure 5.9: XRD reciprocal space maps along [-1-123] of (a) MT-1, (b) MT-2, (c) MT-3 and (d) the DS streak and tilt plot for all MT samples compared with previous UG-2, NL-3 and ST-2.**

RSM measurement conducted along [-1-123] is as presented in Figure 5.9. From the RSMs it is safe to presume that the XRC analysis is accurate whereby the DS streak for MT-3 was observed to be the most elongated followed closely by MT-1 and finally MT-2. The Qx offsets were also in good agreement wherein MT-2 exhibit the most offset compared with MT-3 and MT-1. This signifies the use of an intermediate alternates of multiple $NH_3$ treatment possess the optimum conditions to render a better crystal quality. Comparison of the DS streak with ST-2 amplifies the enhancement exhibited by the multiple treatment samples compared with the single treatment approach. All MT samples exhibited significant shrinkage in the DS streak elongation compared with ST-2. The recorded reduction of DS streak exhibited by MT-2 was around ~30% compared with ST-2 which ignites lower PSFs presence. Furthermore, the tilt comparison also exerted similar trend where all MT samples possess higher tilt compared with ST-2, elucidating higher relaxation state even upon comparison with UG-2 and NL-3. The alternating multiple treatment approach have shown considerable crystal improvement compared with single treatment approach.

### 5.2.3 Surface Morphology of Uid-GaN with Optimized $NH_3$ Treatment

Due to the enhance crystal quality observed in the XRCs analysis for MT-2 morphological analysis was further implemented to determine whether the multiple treatment would also enhance the surface properties. Figure 5.10(a) depicts the 2D and 3D 10×10 μm AFM images of MT-2. From the figure, the arrowhead-like features observed as before in NL-3 and UG-2 was amplified and widened (as highlighted in red arrowhead lines) giving rise to lower number of arrowheads. Considerable widening of the arrowhead features induces the formation of the elongated deep valleys (as highlighted in blue circles) which significantly increased the surface RMS roughness to 13.57 nm.

Average line profile reveals a heightened peak (~28 nm) and deepened valley of the undulations (~ -4 nm). The intensity of the undulation for each arrowhead portrayed significant inhomogeneity which contributes to the increased surface roughness. The implementation of the MT approach has shown to drastically reduce the density of the arrowhead features with the expense of the heightened undulations and broader arrowhead widths.

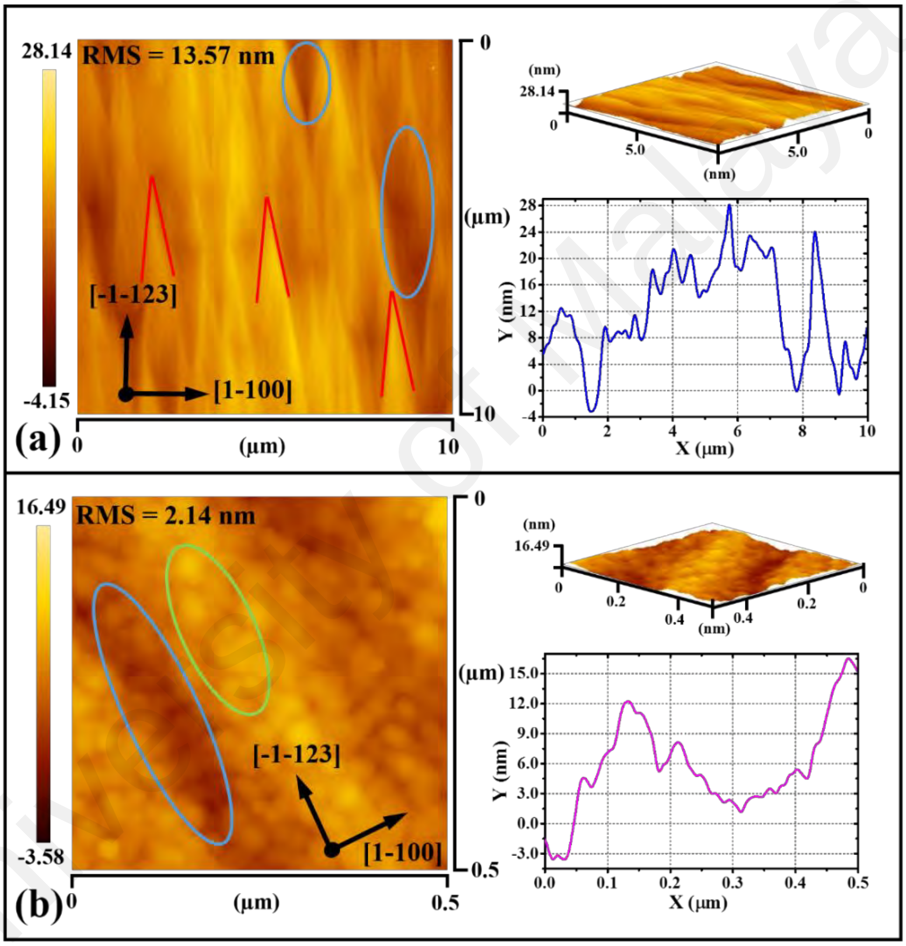


**Figure 5.10: (a) 10×10 μm and (b) 0.5×0.5 μm AFM images of MT-2 with its respective 3D image as well as the average line profile of the image.**

Furthermore, the lower scan sizes of 0.5×0.5 μm AFM images also portrayed surface evolution as presented in Figure 5.10(b). The terrace-steps arrangement showed critical deterioration wherein smaller terrace sizes were distributed along the valley depths (as highlighted in blue circles) whilst larger terrace-step sizes were finely distributed along the heightened peaks (as highlighted in green circles). It is known that the reactivity of $NH_3$ with GaN at elevated temperature (>1000C) during the treatment would cause a phenomenon (Hsu et al., 2011; Song et al., 2013) where the formation of numerous voids occurred leading to immense valley existence. Average line profile reveals a heightened peak-to-valley of roughly ~20.0 nm with distance of ~160.0 nm. Such profile contributes towards the formation of significantly widened arrowhead-like features as depicted in the higher scan sizes.

The results obtained indicates that the use of the multiple $NH_3$ treatments would aid in the reduction of certain defects such partial and/or perfect dislocations as well as PSFs as compared with the single $NH_3$ treatments. However, when overcoming the BSFs, such approach still might not be favorable. It was reported by Hsu et al., 2011 that the use of $NH_3$ treatment prior to the subsequent GaN growth would facilitate the formation of etched facets which would be merged by the lateral growth step. Similar to the single $NH_3$ treatments, such etching process would occur at the lowest thermally unstable dislocation sites (Hsu et al., 2011). It is presumed that with additional alternating $NH_3$ treatments, additional dislocation sites were further deformed/disturbed inducing better crystal quality (Weyher et al., 2009). However, if excessive treatments occurred, such phenomenon would cause detrimental effects towards the crystal rather than enhancing it. Despite that, the multiple $NH_3$ treatment approach causes surface roughening of the Uid-GaN to higher degree mainly owing to the selective deformation of dislocations. This leads to the prevention of the epilayer coalescence prior to the Uid-GaN epilayer. In light of that, further optimizations favoring certain parameters of the multiple $NH_3$ approach should be altered for both crystal (including all defects types' reduction) and morphological property enhancement.

## 5.3 Insertion of AlN/GaN Inter-multilayers (I-MLs)

In this part of the work, the use of alternating periodic inter-multilayers (I-MLs) consists of AlN and GaN was implemented as the third defect reduction technique after the single and multiple $NH_3$ treatments. As both of the previous defect reduction technique showed their potential in tackling either the surface or the crystal quality, it is crucial to address both parameters within one single technique. Motivated by all the previous optimization, a combination of the previous technique was conducted wherein the use of alternating periodic inter-multilayers was observed with optimization of the pairing numbers from 20 to 200 pairs of I-MLs.

### 5.3.1 The Growth Conditions Involved

The growth conditions of the I-MLs utilizes the same pre-optimized AlN and GaN growth conditions for the nucleation layer as well as the Uid-GaN epilayer. However, the AlN and GaN alternates' growth duration within the I-ML was altered to yield significantly lower thickness of 4.5 nm and 20 nm respectively. The rest of the parameters were kept constant with temperature of 1050 °C, pressure of 13.3 kPa, TMG = 60 sccm and TMA = 98.5 sccm. The steps involved are depicted in Figure 5.11: (a) substrate cleaning, (b) nitridation procedure, (c) growth of AlN NL, (d) insertion of AlN/GaN I-MLs with variations of pairs, (e) Uid-GaN growth. As the previous multiple $NH_3$ treatments showed dissimilar structural enhancement with different alternates, hence it would be crucial to determine whether such variations would play a role in the I-ML approach. The pairing numbers of the I-MLs were varied from 20, 40, 60, 80, 100, 150, and 200 pairs designated as I-ML-1, I-ML-2, I-ML-3, I-ML-4, I-ML-5, and I-ML-6, respectively, with each AlN and GaN thin epilayers maintained the same exact growth conditions to eliminate any additional factors impacting the subsequent Uid-GaN properties.

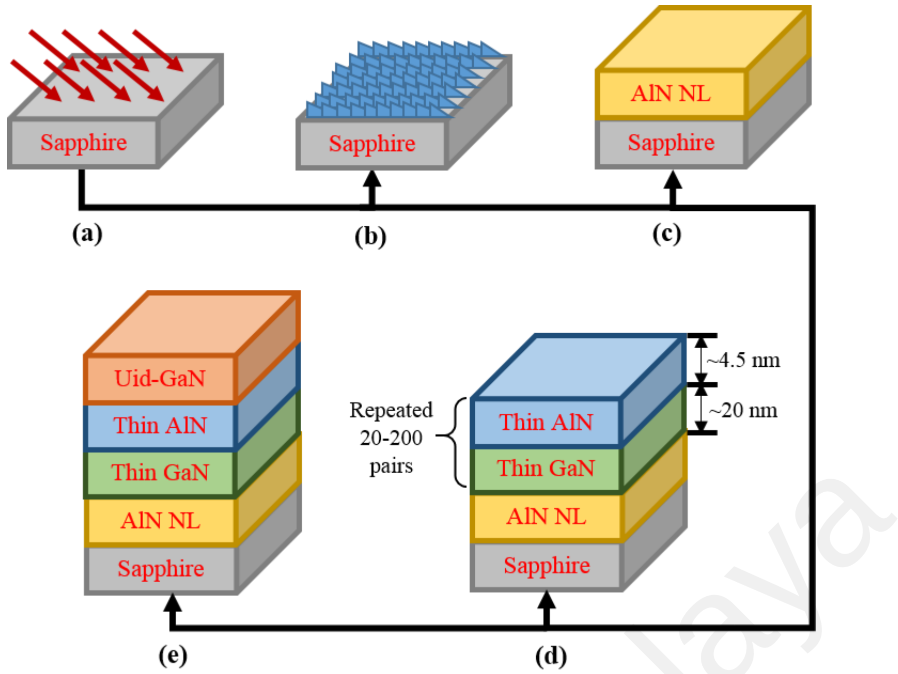


**Figure 5.11: Growth steps involved during the growth of Uid-GaN with the insertion of inter-multilayers consist of AlN/GaN.**

### 5.3.2 Impact of I-MLs on the Crystal Quality of the Uid-GaN

$2\theta/\omega$ scans of all the I-MLs showed slight variations in the satellite fringes between I-ML-1 until I-ML-6. Figure 5.12 depicts the $2\theta/\omega$ scans where all I-MLs exhibits the same existence of sapphire, GaN and AlN peaks. However, few I-MLs exhibit quite intense satellite fringes which correspond to the presence of the AlN/GaN epilayers. Intensity of the fringes were further related to the abrupt interfacial quality as well as the higher number of pairs. From the figure I-ML-6 exerts the most intense satellite peaks of GaN and AlN presumed to be in correlation with the higher number of AlN/GaN pairs whilst I-ML-5 and below exhibit lower intensities of the fringes. I-ML-1and -2 on the other hand exhibit low to none satellite fringes suggesting an occurrence of either growth disruption or interfacial inhomogeneity within the inter-multilayer growth. It cannot be presumed that the growth of the I-MLs were unsuccessful when the high number of I-MLs showed significance indication of the AlN/GaN presence. Hence further analysis was conducted with the use of FESEM imaging of the cross-section for clarifications which will be discussed later in the chapter.

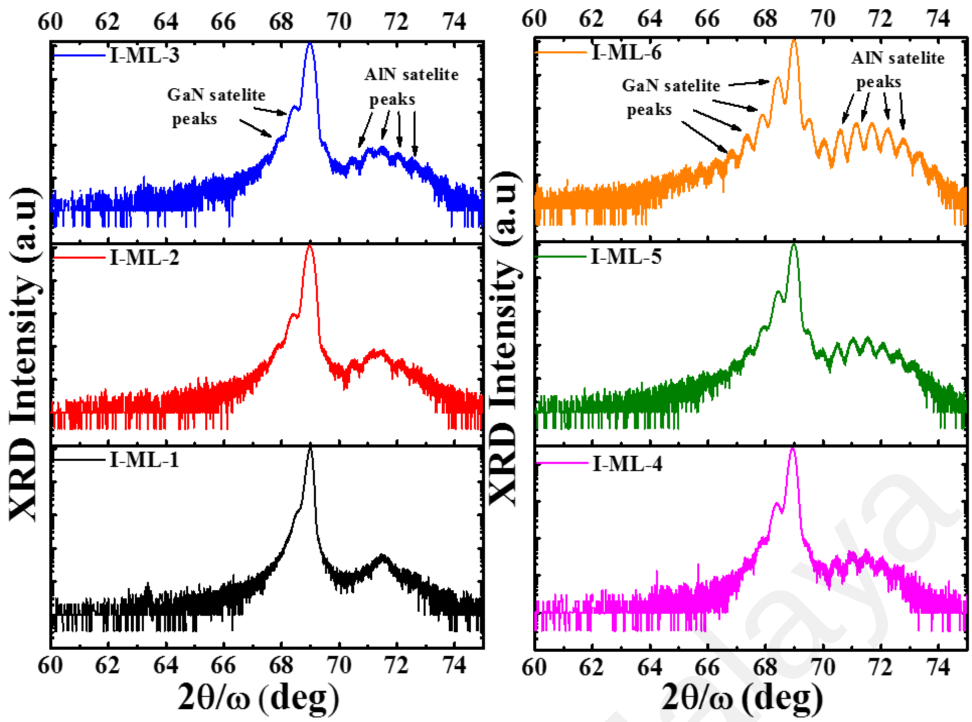


**Figure 5.12: HR-XRD, $2\theta/\omega$ scans of the Uid-GaN epilayers with various pairings of AlN/GaN inter-multilayers optimizations.**

Since the growth of the Uid-GaN with the insertion of the I-MLs were successful, even though the difference of interfacial abruptness occurred at lower number of pairs, on- and off-axis XRCs analysis of the I-ML samples were conducted first to determine any enhancement or degradation of the crystal should occur. Figure 5.13(a) represents the on-axis XRCs plot with steps intervals of its azimuthal angle. From the figure, a clear trend of reduced anisotropy can be observed as the number of AlN/GaN pairs were increased. I-ML-6 possess the lowest XRC FWHMs broadening in both [-1-123] and [1-100] direction of 0.11° (396 arcsec) and 0.21° (756 arcsec) whilst I-ML-1 exhibit the broadest XRC FWHMs in both directions. This indicates better overall crystal properties was attained with I-ML-6 compared with I-ML-1 as presumed earlier. However, the degree of reduction was dissimilar between the I-MLs. Only slight reduction was observed between I-ML-1 and I-ML-2 whilst I-ML-3 and above portrayed larger degree of reduced anisotropy. The result seems to coincide with the $2\theta/\omega$ scans indicating better structural properties was achieved with I-ML-6.

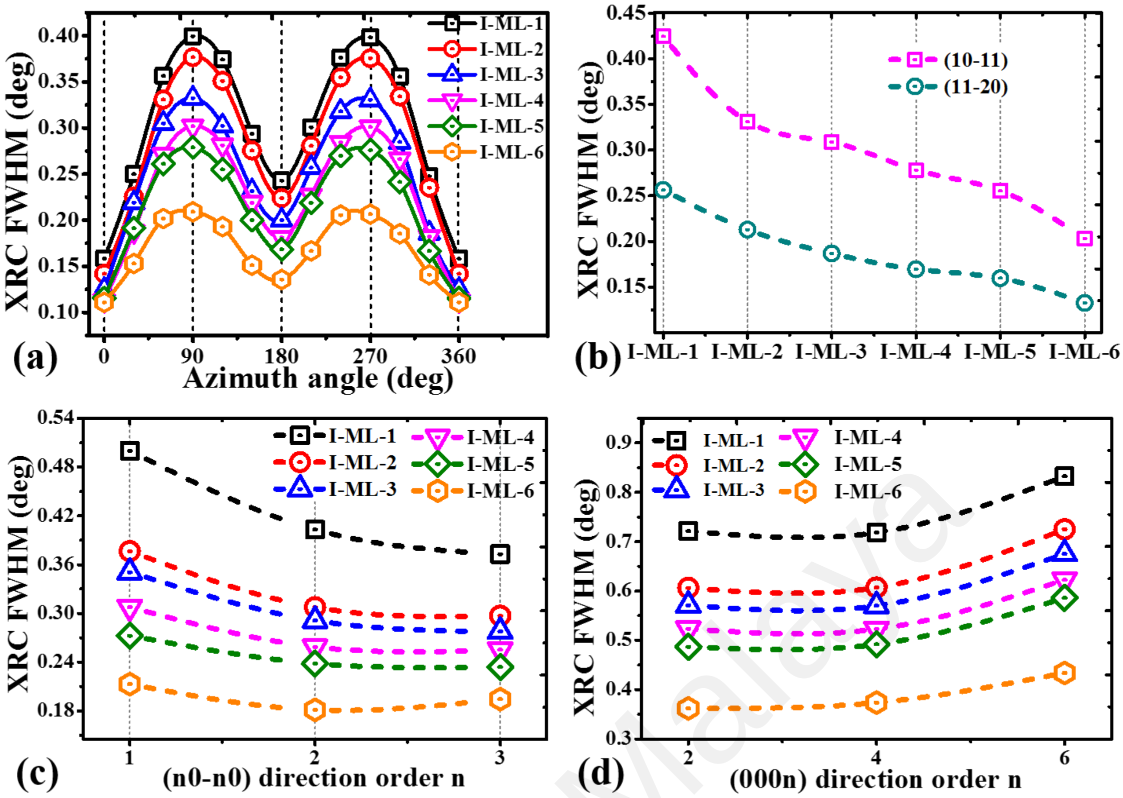


**Figure 5.13: XRC FWHMs of all inter-multilayers via (a) on-axis configuration, (b) off-axis configuration along (10-11) and (11-20), (c) the (n0-n0) series and (d) the (000n) series.**

Since the occurrence of remarkable reduction in the anisotropy, similar trend should be observed for the off-axis XRCs. Figure 5.13(b) represents the off-axis XRC FWHMs of both (10-11) and (11-20) diffraction planes revealing the estimation of PSFs and perfect dislocations density. From the figure, the trend in (10-11) portrayed significant narrowing of the XRC FWHMs of I-ML-2 from I-ML-1 with a linear decrement of the FWHMs towards ML-6. Conversely, the XRC FWHMs for the (11-20) diffraction planes showed a different trend wherein moving across the spectrum from I-ML-1 to I-ML-6, only a linear reduction in the FWHMs were observed. The spectrum suggests variants in the density of PSFs and perfect dislocations in which the inter-multilayers period increment of 20 pairs to 40 pairs yield better reduction in PSFs compared to perfect dislocations. The (n0-n0) series as depicted in Figure 5.13(c), portrayed similar trend to the (10-11) diffraction plane whereby there exist a progressive narrowing in the XRC

FWHMs from I-ML-1 to I-ML-2 whilst going up the period of the AlN/GaN towards I-ML-6 exhibit a linear trend in FWHM narrowing. The spectrum suggests higher degree of BSFs both type $I_1$ and $I_2$ reduction from 20 to 40 pairs compared with the subsequent additional pairs. Similarly, the (000n) series exhibit the same trend as (n0-n0) series wherein the transition of I-ML-1 to I-ML-2 showed the most drastic reduction in the FWHMs as shown in Figure 5.13(d). The trend also suggests higher degree of reduction of partial and perfect dislocations having Burgers vectors of c-axis component. Despite all mentioned above, I-ML-6 exhibited the most remarkable crystal quality due to having the lowest FWHMs broadening in all the off-axis XRCs. It can be presumed that the higher number of the I-MLs would aid in the reduction of various defects such as PSFs, BSFs, partial and/or perfect dislocations.

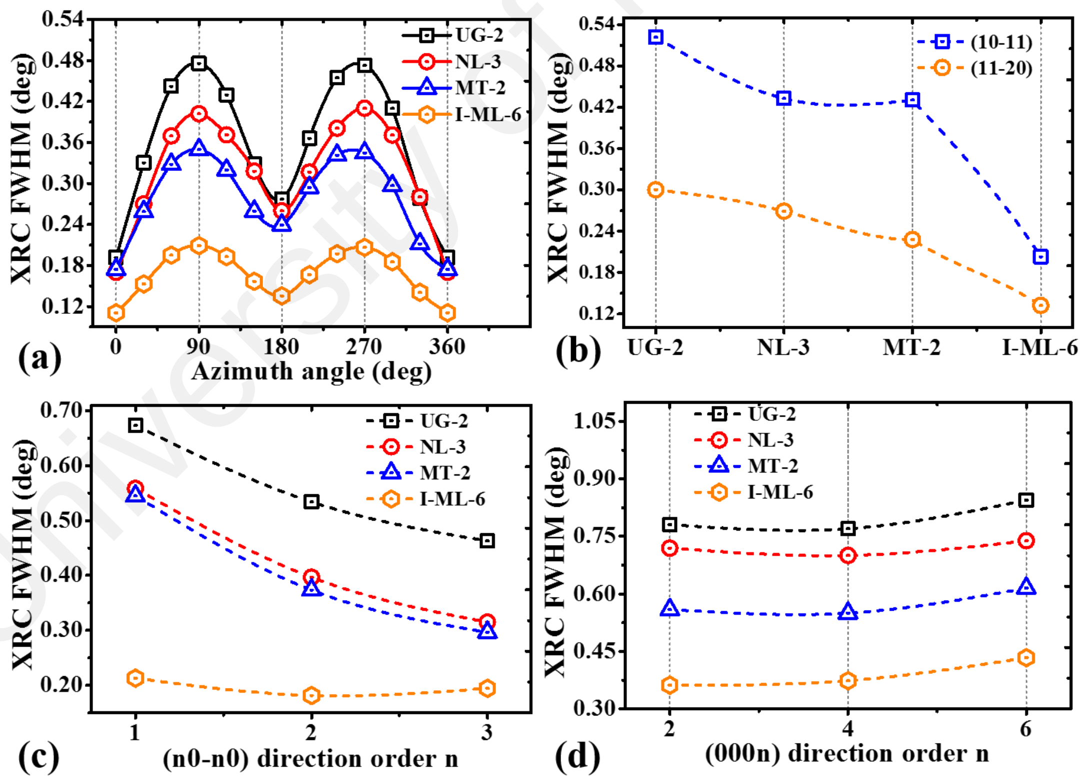


**Figure 5.14: XRC FWHMs of I-ML-6 as compared with the previous optimizations UG-2, NL-3, and MT-2 via (a) on-axis configuration, (b) off-axis configuration along (10-11) and (11-20), (c) the (n0-n0) series and (d) the (000n) series.**

Further comparison with the previously optimized samples UG-2, NL-3, and MT-2 showed remarkable anisotropic reduction was achieved with the use of 200 periods of AlN/GaN I-MLs as shown in Figure 5.14(a). The reduction in FWHM broadening of I-ML-6 along [-1-123] compared with UG-2 was roughly ~42% and compared with NL-3 and MT-2 was around ~ 32% (as NL-3 and MT-2 possess similar XRC FWHM along [-1-123]). However, for [1-100] the reduction was higher when compared with UG-2, NL-3 and MT-2 at roughly ~58%, 50% and 42%, respectively. This reveals that the inter-multilayers insertion has successfully improved the anisotropic properties in an exceptional degree compared with the 1-step (UG-2) and 2-step (NL-3) growth techniques. The I-ML approach with 200 pairs of AlN/GaN was also observed to surpass the anisotropic reduction capability of the MT approach. Such reduction signifies the capabilities of the numerous alternating AlN/GaN I-MLs for overall crystal enhancement. The off-axis XRCs comparison with the previous pre-optimized samples UG-2, NL-3 and MT-2 is as depicted in Figure 5.14(b-d)). From the (10-11) diffraction FWHMs, remarkable reduction was observed of around ~62% for I-ML-6 compared with UG-2, and 53% compared with NL-3 and MT-2 (as NL-3 and MT-2 possess similar FHWM along [1-100]). The (n0-n0) series also portrayed similar percentage of reduction of a minimum ~51% igniting the potential of the I-ML (200 pairs) in reducing the BSFs as compared with the MT approach. Additionally, the (000n) series portrayed a minimum reduction of ~36% for I-ML-6 compared with MT-2 revealing higher degree of reduction in the PSFs and/or partial dislocations having c-axis component. Such high percentage of reduction reveals that the insertion of the inter-multilayers would successfully reduce the overall defects densities.

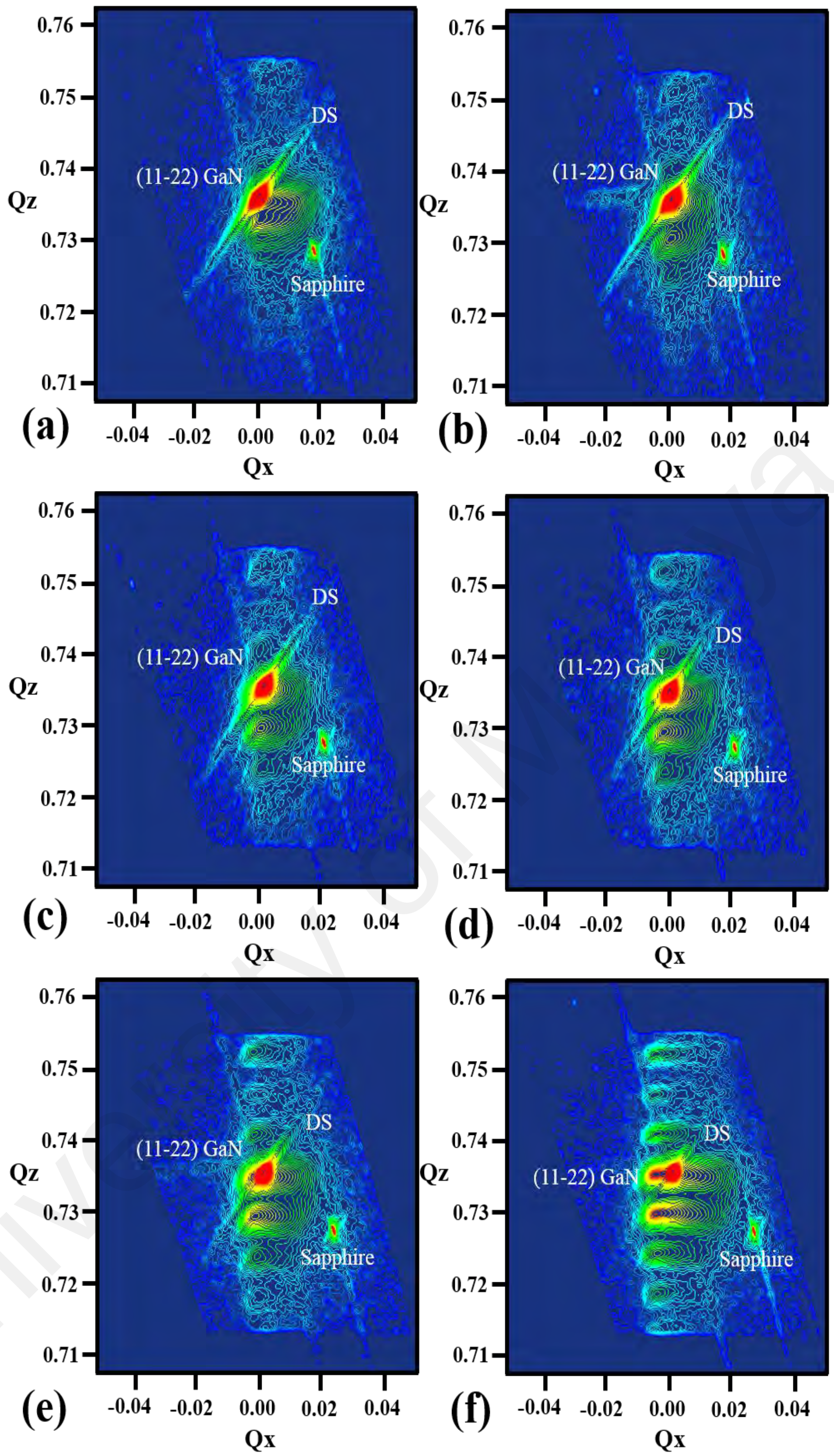


**Figure 5.15: XRD reciprocal space maps along [-1-123] of (a) I-ML1, (b) I-ML-2, (c) I-ML-3, (d) I-ML-4, (e) I-ML-4, (f) I-ML-5 and (g) I-ML-6.**

Additionally, RSM measurements along [-1-123] as depicted in Figure 5.15 with respect to the extracted DS streaks and tilts as in Figure 5.16(a) further supports the XRCs analysis. From the figures, it can be observed that there is a variant in the DS elongation streak from I-ML-1 to I-ML-6. I-ML-1, -2 and -3 exhibited similar features with variation of the DS elongation from 0.0350, 0.0320 and 0.0296 Å$^{-1}$ whilst the tilt progressively increased from 0.6636° to 0.8536° to 1.0337°.  As the I-MLs increased to 80 and 100 pairs, a clear emergence of satellite fringes was observed indicating higher number of AlN/GaN pairs, with I-ML-6 exhibiting the most and clear satellite fringes. The DS streak from I-ML-4 to I-ML-5 portrayed smaller reduction of the DS elongation whilst I-ML-6 exhibited significantly low to none DS elongation of roughly ~0.0109 Å$^{-1}$. The Qx offset with I-ML-6 was also seen the highest at 1.5824° signifying immense macroscopic tilts in the epilayer as a result from the higher number of AlN/GaN pairs inducing higher density of MDs to facilitate the relaxation of the epilayers (Tyagi et al., 2009). Further comparison with the previous optimizations (UG-2, NL-3, ST-2 and MT-2) as shown in Figure 5.16(b) indicates immense reduction in the DS streak of a minimum ~65% and tilt increment of ~ 90%. The results suggest exceptional degree of relaxation in the epilayer with remarkable reduction in the PSFs upon the use of significantly higher number of AlN/GaN I-ML pairs (200 pairs).

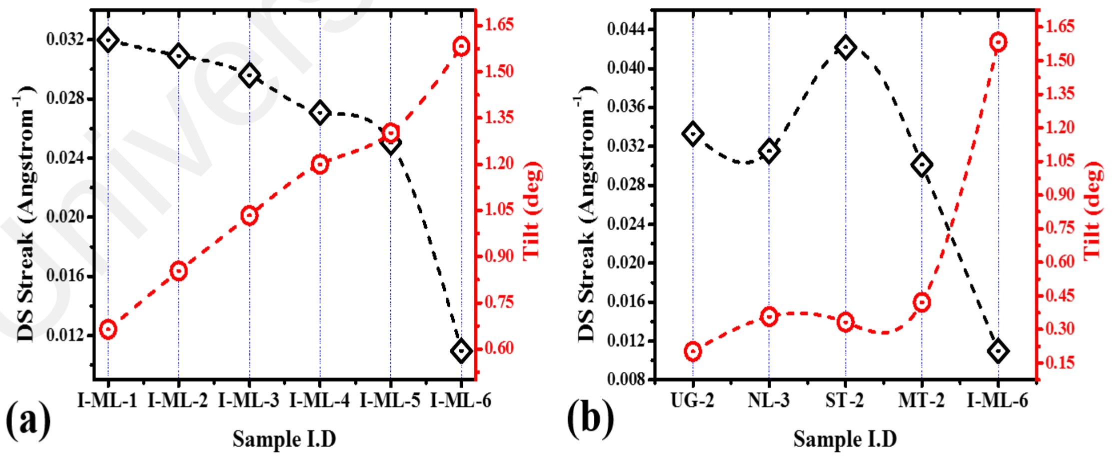


**Figure 5.16: DS streak and tilt plots from the RSM measurement for (a) all I-MLs and (b) I-ML-6 as compared with previous optimization.**

### 5.3.3 Morphological Analysis of the Uid-GaN with I-MLs

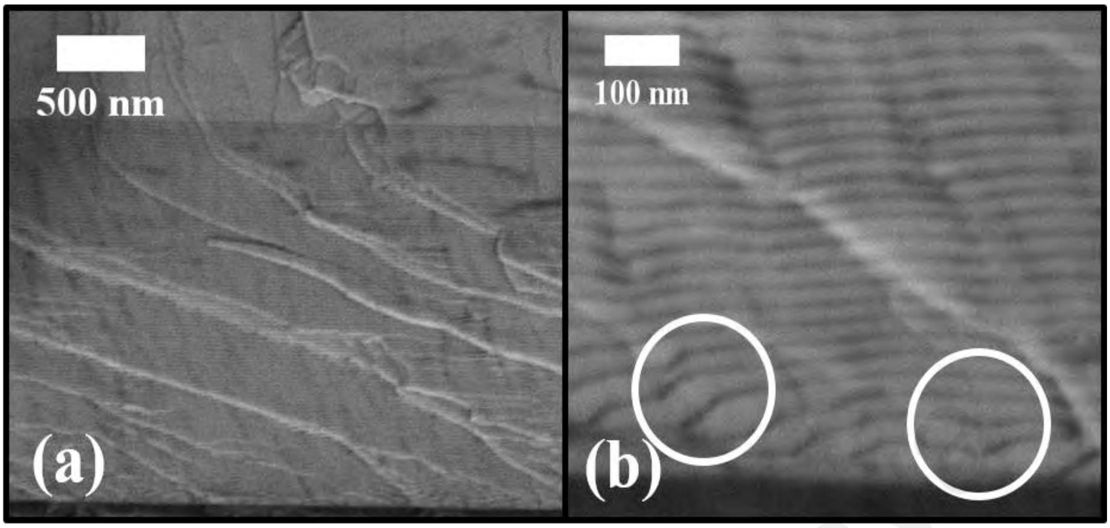


**Figure 5.17: FESEM cross-sectional image (a) low magnification and (b) higher magnifications of the inter-multilayers interfacial differences between lower number of pairings and higher number of pairings from I-ML-6.**

Figure 5.17 depicts the cross-section of the I-MLs for the lower number of I-ML pairs. From the figure, it can be deduced that the I-MLs were successfully grown even from the beginning of I-ML-1 where the brighter contrast represents the GaN whilst the darker region corresponds to the AlN. However, the interfacial abruptness was seen to be in a wavy manner as highlighted in white circles in Figure 5.17(b) suggesting a 3-demensional growth occurred in the early stages of the I-MLs which might be resulted from the numerous defects generation. However, slight improvement was observed as higher numbers of AlN/GaN was grown (40 pairs) and further progressive enhancement in the I-MLs interfaces was seen upon increased number of pairs (60 pairs). Such phenomenon would continue to occur until the highest number of AlN/GaN pairs (200 pairs) was grown. It should be noted that the growth conditions of the AlN/GaN from the first pair up to the 200$^{th}$ pair were grown under the exact same conditions; hence, the growth mode variation between the preliminary I-MLs and its later pairs implies a secluded phenomenon occurred within the heterointerface.

Surface properties evaluation via AFM was conducted for all the I-MLs as presented in Figure 5.18 and Figure 5.19 to observe the impact of each I-ML pairs. Figure 5.18 depicts the 10×10 μm AFM images of I-ML-1 until I-ML-6 with its corresponding average line profiles. Since more than 2 samples were measured, it is only accurate to view the images via its respective scales (image contrast scale to the left of each image) as they possess different scaling (where each image exhibit dissimilar contrast scale). For example, Figure 5.18(a) and (b) depicts different scaling contrast of 72.35 nm and 53.21 nm at maximum whilst -14.12 nm and 9.35 nm at minimum. This reveals dissimilar maximum/minimum height/valley values with respect to its corresponding contrast scale, for different images and just by analyzing the image (via contrast color only) would not be deemed the most accurate analysis. Hence, analysis via its respective average line profiles would be more preferable as it corresponds directly to its respective image.

It can be observed from Figure 5.18 that there exists a surface evolution from I-ML-1 until I-ML-6. I-ML-1 was significantly plagued by the arrowhead-like features as indicated by the red arrowhead lines. Such feature is quite similar to the previous MT-2 wherein the arrowhead density contributes to considerably high surface RMS roughness of ~ 16.24 nm (close to the value of MT-2). The average line profile of the image displayed an immense peak-to-valley height of ~54 nm with dissimilar arrowhead-width overlapping each other constituting intense undulations Such undulations results in the formation of deep-widened valleys (as highlighted in green circles in the image).

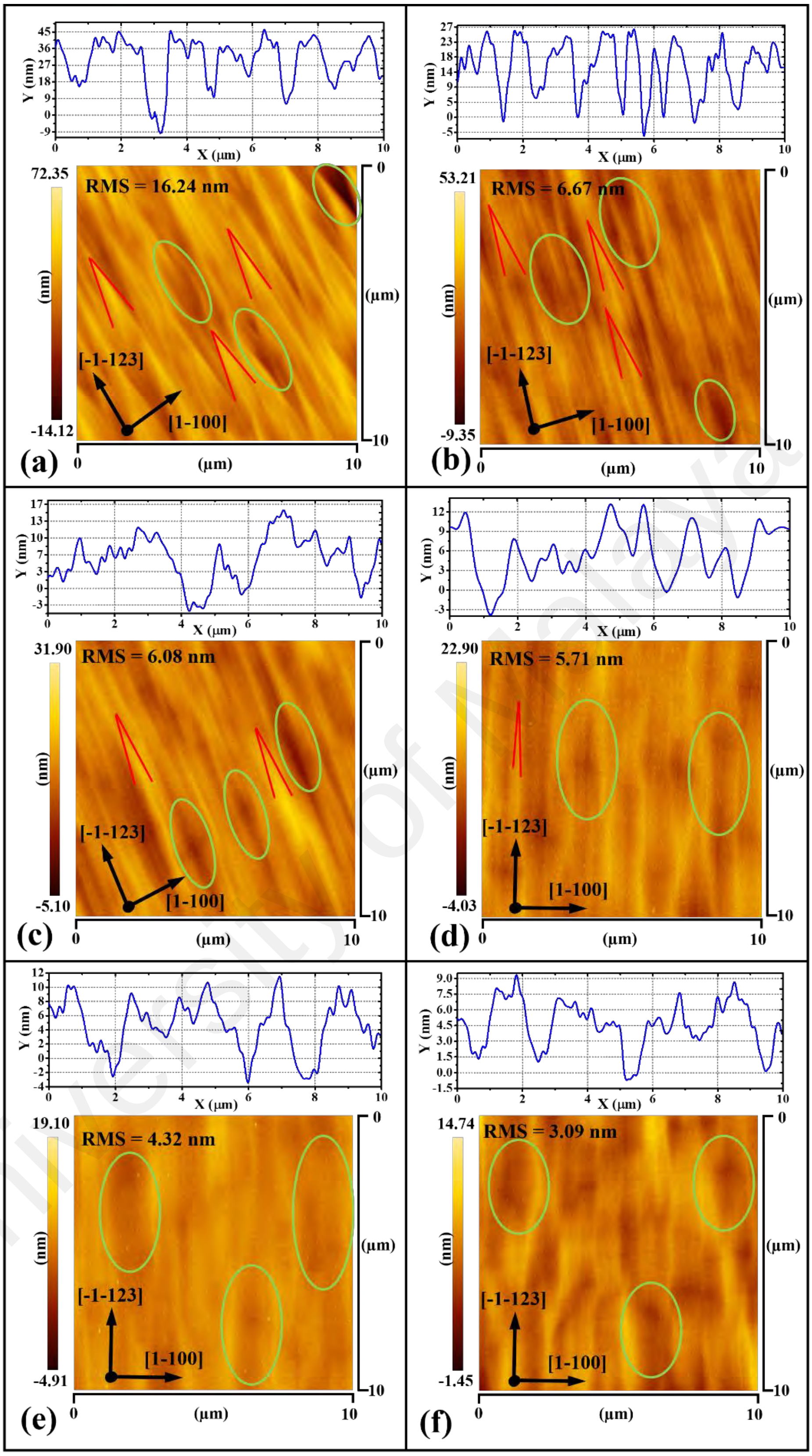


**Figure 5.18: 10×10 μm AFM images as well as the average line profile of (a) I-ML-1, (b) I-ML-2, (c) I-ML-3, (d) I-ML-4, (e) I-ML-5 and (f) I-ML-6.**

In contrast, as the pairing of the AlN/GaN I-ML was increased up to 40, the surface property changed entirely with presence of large arrowhead-features being absent leaving only traces of narrower arrowheads. Average line profile of the image further confirms that the arrowheads present were only in the range of not more than ~1.0 μm in width. The undulations were also receded where the highest peak-to-valley observable did not exceed more than 30 nm in height giving rise to the formation of shallower valleys (as highlighted in green circles in the image).

On the other hand, I-ML-3 rendered a fairly even surface image only few small protruding arrowhead-like features exist. Long-sharp striations were still present on the surface as depicted in the average line profile of the image. In addition, the surface have evolved from highly compact to sparsely distributed peak-to-valley which aids the smoothening of the surface yielding only 6.08 nm in RMS roughness. Further increasing the AlN/GaN pairs up to 80 and subsequently 100 pairs yielded similar properties by which the surface rendered a somewhat uniform sparsely distributed striations constituting the reduced undulations as highlighted in green circles. Such occurrence facilitates the linear reduction in the surface RMS roughness from 5.71 nm (I-ML-4) to 4.32 nm (I-ML-5). Finally, with the insertion of 200 pairs I-MLs, the morphological properties was remarkably enhanced with absence of the arrowhead-like features. This is mainly due to the least undulations exhibited by I-ML-6 where the average line profile recorded the highest peak-to-valley of ~ 9.0 nm. Such phenomenon constitutes in the remarkable reduction in the surface RMS roughness of 3.40 nm.

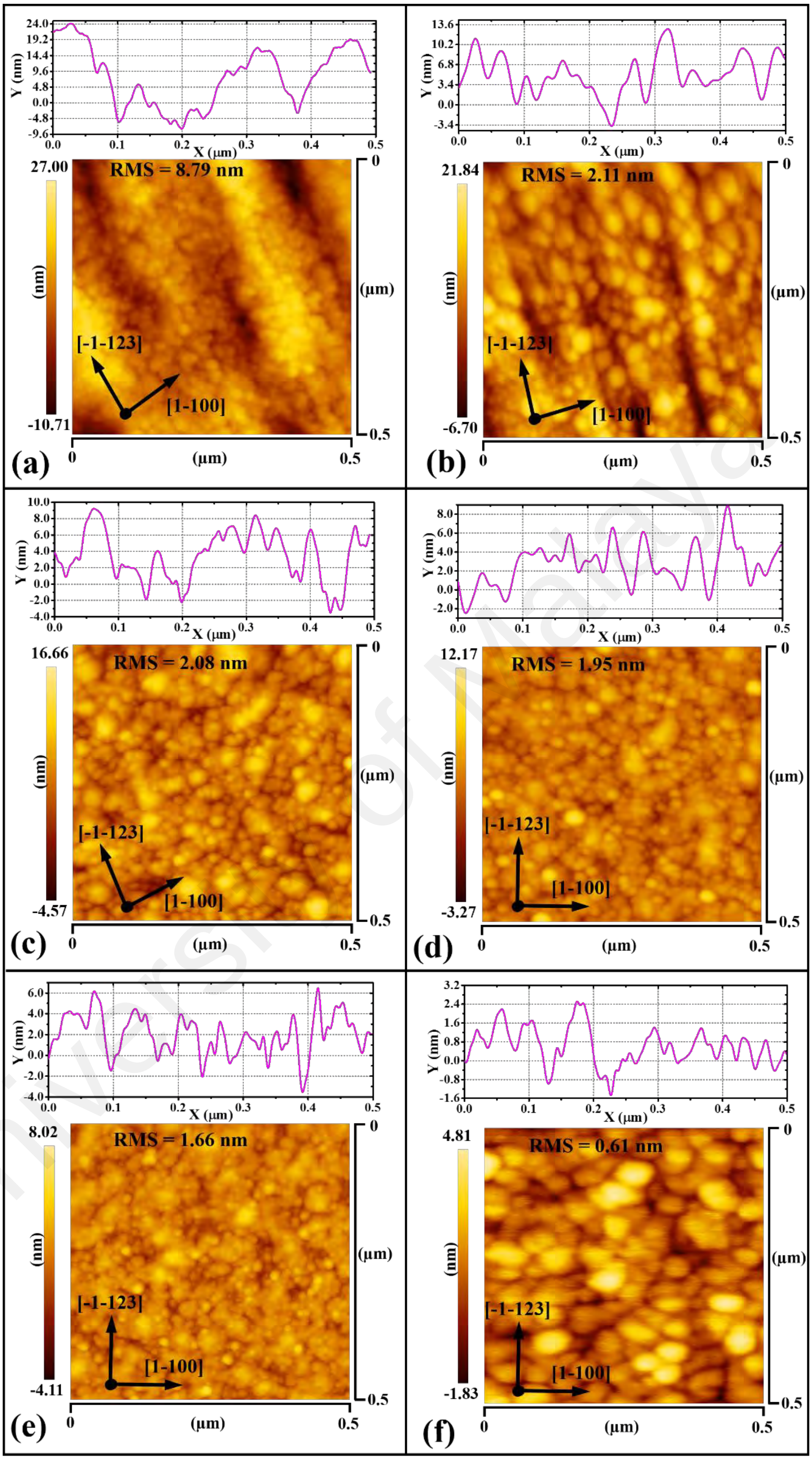


**Figure 5.19: 0.5×0.5 μm AFM images as well as the average line profile of (a) I-ML-1, (b) I-ML-2, (c) I-ML-3, (d) I-ML-4, (e) I-ML-5 and (f) I-ML-6.**

Further clarifications on the matter were analyzed with the 0.5×0.5 μm AFM scans as shown in Figure 5.19. It can be observed from the figures that the use of I-ML prior to the growth of the Uid-GaN would facilitate terrace-steps rearrangements/deformations to better or worse conditions depending on the parameters used (number of pairs). I-ML-1 portrayed a highly irregular terrace arrangement with significant deep-wide valley formations. This would be the main causality of the high number of the arrowhead-like features in the larger scan size. Even though the terrace arrangement was still unorderly arranged in I-ML-2, the valley depth and width were observed to recede. I-ML-3 and so forth portrayed a linear trend in enhancing the terrace-steps arrangement. Despite that, as the I-ML reached 200 pairs, the terrace has evolved and arranged itself in a uniformly manner. The terrace-steps arrangement and distribution are mainly due to the presence of either random or homogeneously distributed average terrace sizes. Lower number of I-ML pairs (20-40 pairs) would yield random terrace sizes which contributes to non-uniform distribution as well as arrangement leading to deep widen valley formations. Intermediate I-MLs (60-100 pairs) exhibit progressively enhanced terrace-sizes resulting in better arrangement and distribution. Higher I-MLs (100-200 pairs) would then aid the terrace sizes formation to an average larger size as compared with the rest. The main consequences of the terrace sizes formation and its arrangement would be described as follows: (i) if the average terrace sizes are random (small and larger sizes were present), then the arrangement would also be random, rendering spaces for void formations which leads to deep/wide valley formation. (ii) If the average terrace sizes were uniformly distributed, then the arrangement would be homogeneously distributed (closely packed rather than sparse), avoiding the formation of numerous voids leading to absence of deep/wide valley formations

A correlation between the impact of the I-ML pairs numbers to the Uid-GaN surface properties can be rendered with the growth steps within the I-MLs itself. As observed in the FESEM cross-section images, since the growth of the first few pairs of the I-MLs suffered from forming a continuously abrupt heterointerface between the AlN and GaN, the resulting deformed epilayers would lead to the undesired surface of the Uid-GaN epilayer. However, going up with I-ML pair numbers would yield an abrupt continuous heterointerface leading to a better surface morphology of the Uid-GaN epilayer. Clarification on the matter is elucidated further in the HR-TEM imaging.

### 5.3.4 TEM Imaging of Defect Reduction Phenomenon

As the crystal and surface morphology was enhanced with higher pairing numbers, hence it is presumed that a defect reduction phenomenon did indeed occurred. Further evaluation on the matter was conducted via a transmission electron microscope (TEM) as shown in Figure 5.20 and Figure 5.21. The TEM cross-sectional imaging was taken along [10-10] zone axis with g = (11-20) for sample I-ML-6. Low magnification bright field (BF) image taken within the region of sapphire/AlN NL/I-ML (earliest pairs) is as shown in Figure 5.20(a).



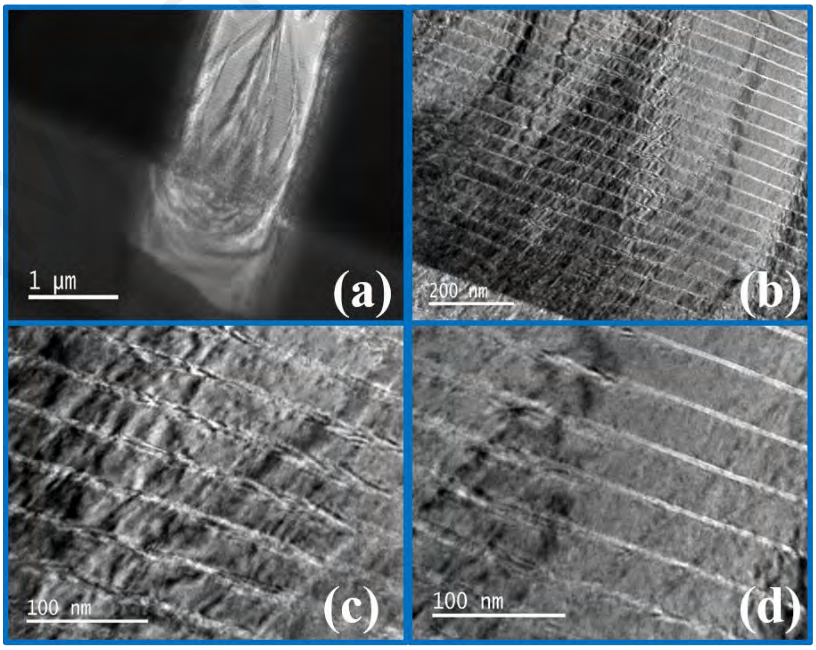


**Figure 5.20: TEM images of the sapphire/AlN NL/AlN/GaN inter-multilayers taken along the [10-10] zone axis with g = (11-20) (a) low magnification, (b) higher magnification, (c-d) high magnification of the defects interaction phenomenon.**

As shown in the figure, it can be observed that between the sapphire, AlN NL and the first few I-MLs were significantly plagued by the generation of various defects. The propagation of the defects continued without any significant resistance. Higher magnification as in Figure 5.20(b) illuminates the presence of wavy discontinuous lines corresponding to the non-abrupt heterointerface of the first few I-MLs due to the presence of numerous defects. It is safe to presume that such occurrence led to the 3D growth of the I-MLs as observed in the FESEM cross-section images. The observable predominant defects were the BSFs of the type $I_1$ with its associated partial dislocations and prismatic stacking faults (PSFs). Furthermore, the subsequent growth of the I-MLs portrayed significant misdirection of the defects forming somewhat a unison propagation. Higher magnification reveals an occurrence of the BSFs termination and folding via its associated partial dislocations and PSFs, respectively. Since the unison propagation have accumulated the defects together such termination and folding would transpire reducing the defects density prior to entering the Uid-GaN epilayer. As depicted in Figure 5.21 the low magnification of the last I-ML pair and the Uid-GaN interface reveals forced looped propagation of the defects would take place, lowering the density of the defects within the Uid-GaN epilayer towards the end (surface of the Uid-GaN).

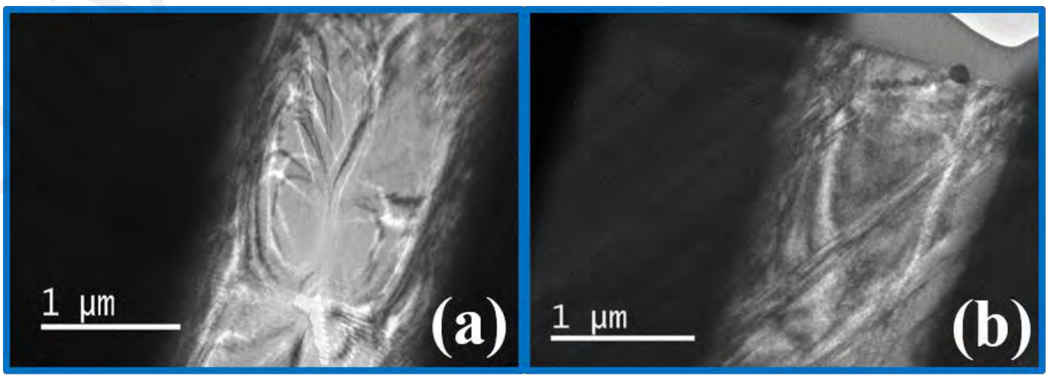


**Figure 5.21: TEM low magnification of the middle (a) (final AlN/GaN I-MLs) and (b) top (surface of Uid-GaN epilayer) interfaces.**

The mechanism involved within the I-MLs approach is as depicted in Figure 5.22 where 5 main phases occurred: Defects generation, defects propagation, defects accumulation, defect reduction (via termination and folding) and finally strain induced defect-loop phenomenon.

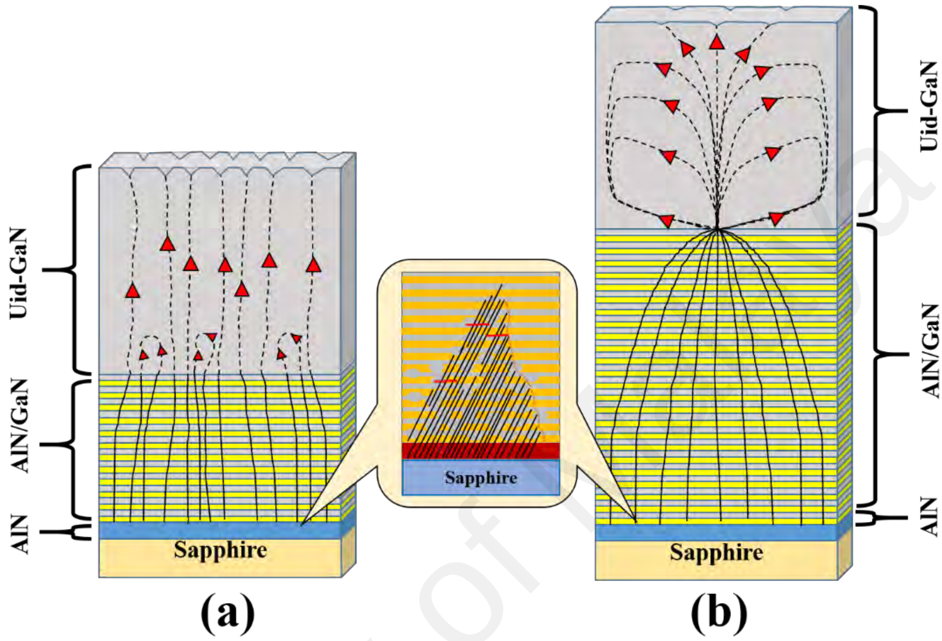


**Figure 5.22: Schematic illustration of the proposed mechanism in the defect reduction phenomenon via insertion of low-high pairing numbers of AlN/GaN I-MLs based on the experimental data.**

From the figure, the preliminary growth of the AlN NL post-nitridation would generate various and numerous defects as mentioned in the previous chapters. Pre-growth of the I-MLs (first 20 pairs) would allow the generated defects including BSFs, PSFs and partial dislocations to propagate through from the NL with detrimental effects towards the growth mode (inducing 3D growth of the I-MLs with non-abrupt interfaces). At the same time, due to dissimilar strain exerted by the alternating AlN and GaN, a forced accumulation occurred. Subsequent growth of the I-MLs (20-40pairs) further forces the defects to misdirect their original propagation path towards each other in a unison manner whilst being reduced in density. The defect reduction occurrence was the BSFs being forced terminated or folded by the existing PSFs and partial dislocation. Partial dislocation have been known in aiding the termination of its associated BSFs whilst PSFs facilitate the folding of the BSFs from one c-plane to another (Dasilva et al., 2010). Since folding of the BSFs occurred simultaneously with the termination, the strained I-MLs would cause an overlapping of the PDs causing only a united propagation of the defects towards the Uid-GaN epilayer. Due to the strain difference exerted by the Uid-GaN, the unison defects propagation were then separated whilst being bent towards each other and causing annihilation of the defects via what is called a closed loop effect (Wu et al., 2017). Even though few defects were not affected by such phenomenon, the density of such defects reaching the surface is considerably low.

This phenomenon would explain why there exists a dissimilarity in the surface morphology of the I-MLs with different pairing numbers. It can be deduced that with higher number of AlN/GaN pairs, higher numbers of related defects accumulation/termination/folding should occur prior to entering the Uid-GaN epilayer leading to higher crystal quality. Furthermore, if a comparison with the previous optimizations, the multiple $NH_3$ treatment MTs would not be able to conduct such phenomenon as the existence of strain alternating layer was absent. Additionally, if no defect reduction technique was implemented as in the optimization of the UG-2 and NL-3, the defects were enabled to continuously propagate through the entire Uid-GaN epilayer without any obstacle causing detrimental effects towards the surface properties. The surface morphological degradation would then cause device fabrication difficulties which constitutes inefficient device operations which will be further discussed in the next chapter.

# CHAPTER 6: UV-PHOTODECTOR OPTIMIZATION

Since the I-ML approach have successfully reduced the defects density to an exceptional degree, further utilization of the pre-optimization Uid-GaN template for the device fabrication is presented. Due to the advancement in the MSM UV-photodetectors structures as mentioned in the previous chapter, few structural customizations was taken into consideration by which a lightly doped n-type GaN was grown prior to a thin Uid-GaN buffer layer beneath the electrode contacts was realized. In this phase, the n-GaN epilayer was first optimized with variations of silane flux exhibiting dissimilar carrier concentration and mobility. The deemed suitable doping would then be applied on the I-ML-6 template as well as the NL-3 template for device performance comparison as both templates exhibit significant differences in crystal quality.

## 6.1 Disilane Variation for n-GaN optimization

### 6.1.1 The Growth Conditions Involved

Upon completion of the Uid-GaN template with the use of AlN/GaN multilayers, subsequently 4 variations of n-type GaN was grown with dissimilar disilane ($Si_2H_6$) flow. The growth of the n-GaN utilizes the same growth conditions as the Uid-GaN wherein the growth temperature was kept at 1050 °C, pressure of 13.3 kPa, TMG flow of 60 and $NH_3$ flow of 0.7 slm. The disilane flux however was varied from 5, 10, 15 and 20 sccm designated as NG-1, NG-2, NG-3 and NG-4 respectively, to evaluate the carrier concentration and mobility for suitable device application. The growth conditions is as depicted in Figure 6.1 where (a) $H_2$ cleaning, (b) nitridation procedure, (c) AlN NL growth, (d) 200 pairs of AlN/GaN I-ML growth, (e) Uid-GaN growth and finally (f) growth of n-GaN. The crystal and morphological quality was still analyzed as to ensure absence of deterioration in both properties.

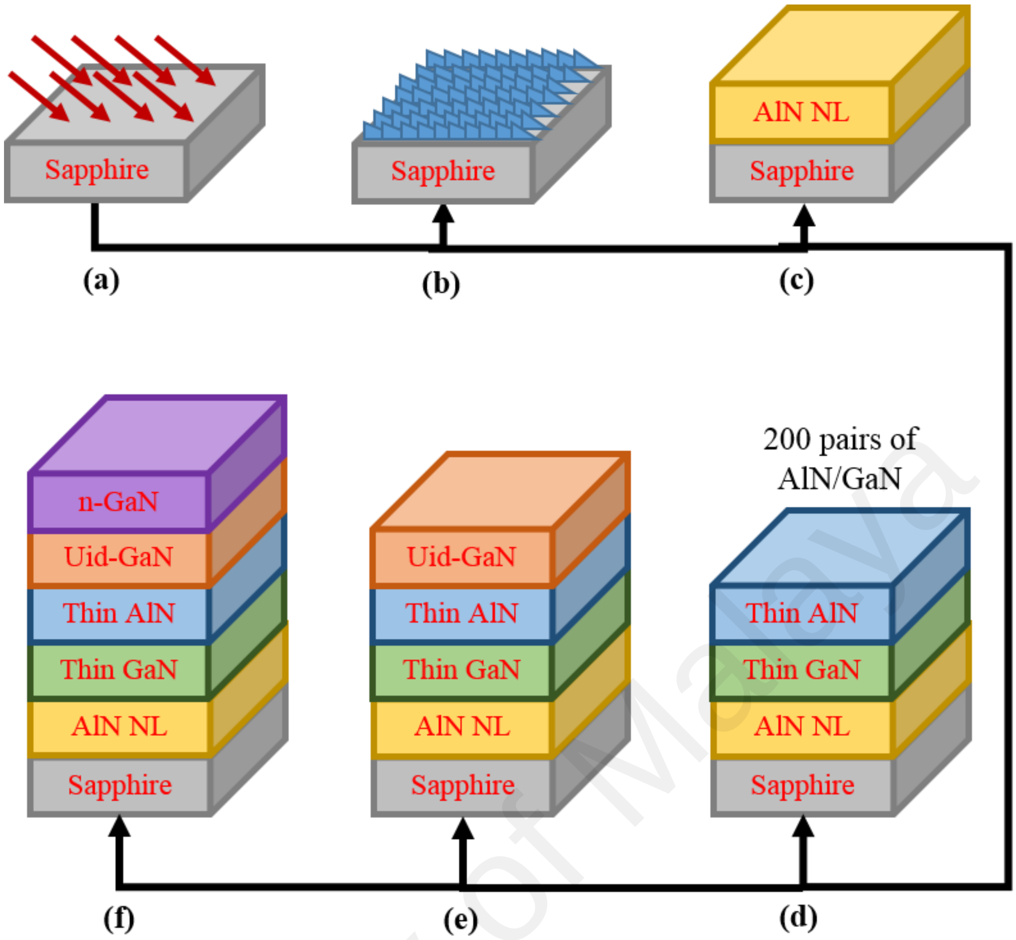


**Figure 6.1: Growth conditions related to the n-GaN optimizations.**

### 6.1.2 Impact of Dissimilar $Si_2H_6$ on the Crystal Quality of the n-GaN

The HR-XRD $2\theta/\omega$ scans of the n-GaN samples are as depicted in Figure 6.2. As mentioned in the previous chapters, it is vital to first ensure that the grown samples exhibit only single crystal (11-22) semi-polar GaN before proceeding with other characterizations. From the figure, it can deduce that even with the variations of the disilane flux of 5 up to 20 sccm, none portrayed a polycrystalline property. Despite that, all the scans exhibit significant intensity of satellite fringes corresponding to the AlN and GaN I-MLs, and since all the samples were grown on the same templates, such property displayed in the $2\theta/\omega$ scans would be reliable. Even so, nonclear visible dissimilarities could be deduced from the $2\theta/\omega$ scans between all the samples.

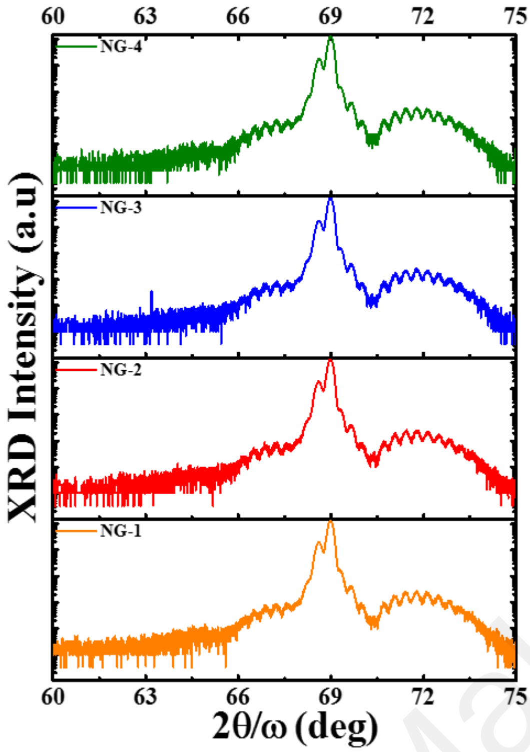


**Figure 6.2: HR-XRD, 2$\theta$/$\omega$ scans of the n-GaN epilayers with various disilane flux variations.**

On-axis XRC was further analyzed similar to the previous chapters with azimuthal variations over 360° as shown in Figure 6.3(a). It was seen from the figure, that all four samples exhibited similar m-shaped azimuthal dependence spectrum with only slight variations. Comparisons between the n-GaN samples are first discussed whereby amongst the 4 samples, NG-1 exhibited the least FWHMs broadening along both [-1-123] and [1-100] whilst NG-4 exhibited the highest FWHM broadening. This indicates a reduced anisotropy with 5 sccm of disilane flux compared with 20 sccm. 15 and 10 sccm on other hand portrayed similar anisotropy behavior. All the n-GaN samples portrayed similar trend with I-ML-6 with slight variations along [1-100]. Only NG-1 exhibit lower FWHMs along [1-100] compared with I-ML-6 indicating slight anisotropic reduction upon increasing the disilane flux linearly from 5 to 15 sccm. However, as the disilane flux was elevated to 20 sccm from 10 sccm, the FWHM was increased linearly along both [-1-123] and [1-100] as compared with I-ML-6. This indicates anisotropic deterioration of the pre-acquired anisotropy property exhibited by I-ML-6.

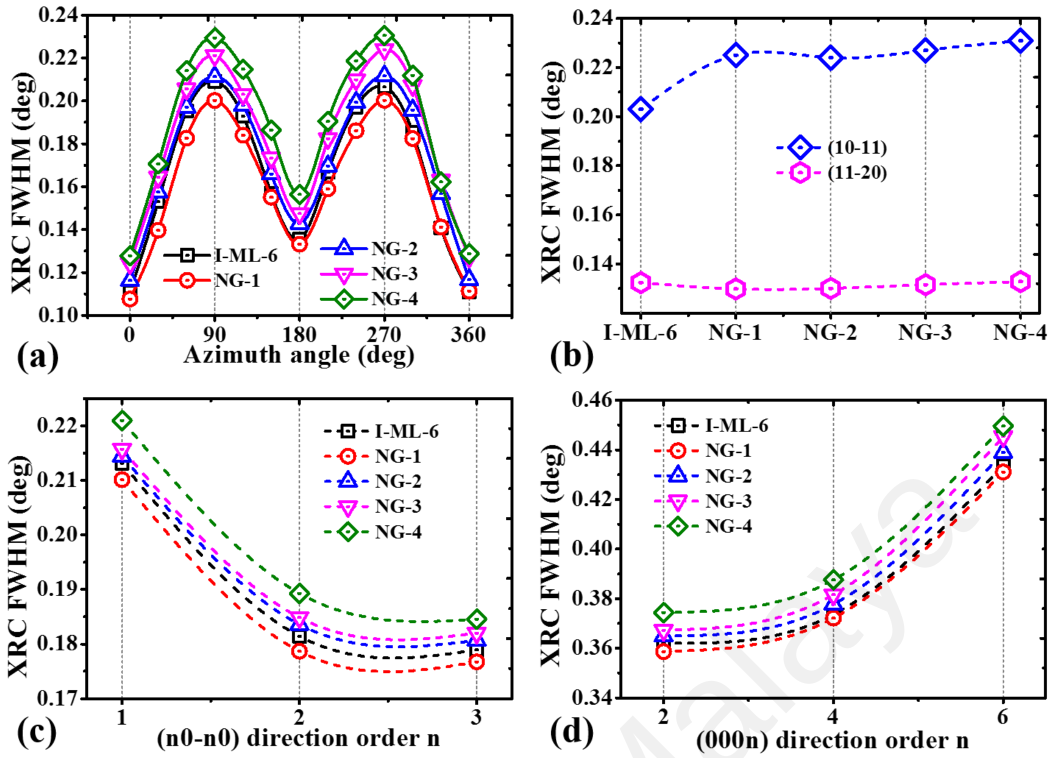


**Figure 6.3: XRC FWHMs of all n-GaN variations as compared with the previous I-ML-6 template via (a) on-axis configuration, (b) off-axis configuration along (10-11) and (11-20), (c) the (n0-n0) series and (d) the (000n) series.**

Further evaluation on the matter was assessed via the off-axis XRCs as depicted in Figure 6.3(b-d). As shown in Figure 6.3(b), the FWHMs of (10-11) and (11-22) for all n-GaN samples with comparison against I-ML-6 displayed an unusual trend. In the (10-11) XRC diffraction, NG-1, NG-2 and NG-3 portrayed similar FWHMs broadening whilst NG-4 showed increased FWHM broadening. Furthermore, comparison with I-ML-6 reveals significant increment for all n-GaN samples indicating higher degree of perfect dislocations existence. The (11-20) XRC diffraction however, displayed slight reduction in the FWHMs with NG-1 exhibiting the lowest, portraying lower PSF densities. The off-axis (n0-n0) series however, displayed NG-1 exhibiting the least high FWHM narrowing compared with NG-2, -3, and -4 as well as I-ML-6 revealing slight reduction of the BSFs density with 5 sccm disilane flow. Conversely, NG-4 displayed significant FWHM broadening compared with others signifying increased BSF density both type $I_1$ and $I_2$. (000n) series on the other hand reveals nonsignificant differences between the n-GaN samples as well as the I-ML-6 except NG-4, indicating similar presence of partial and/or perfect dislocations having a c-axis component. Only with 20 sccm disilane flow exhibit slight increment in the XRC FWHM for the (000n) series indicating increased presence of partial and/or perfect dislocation.

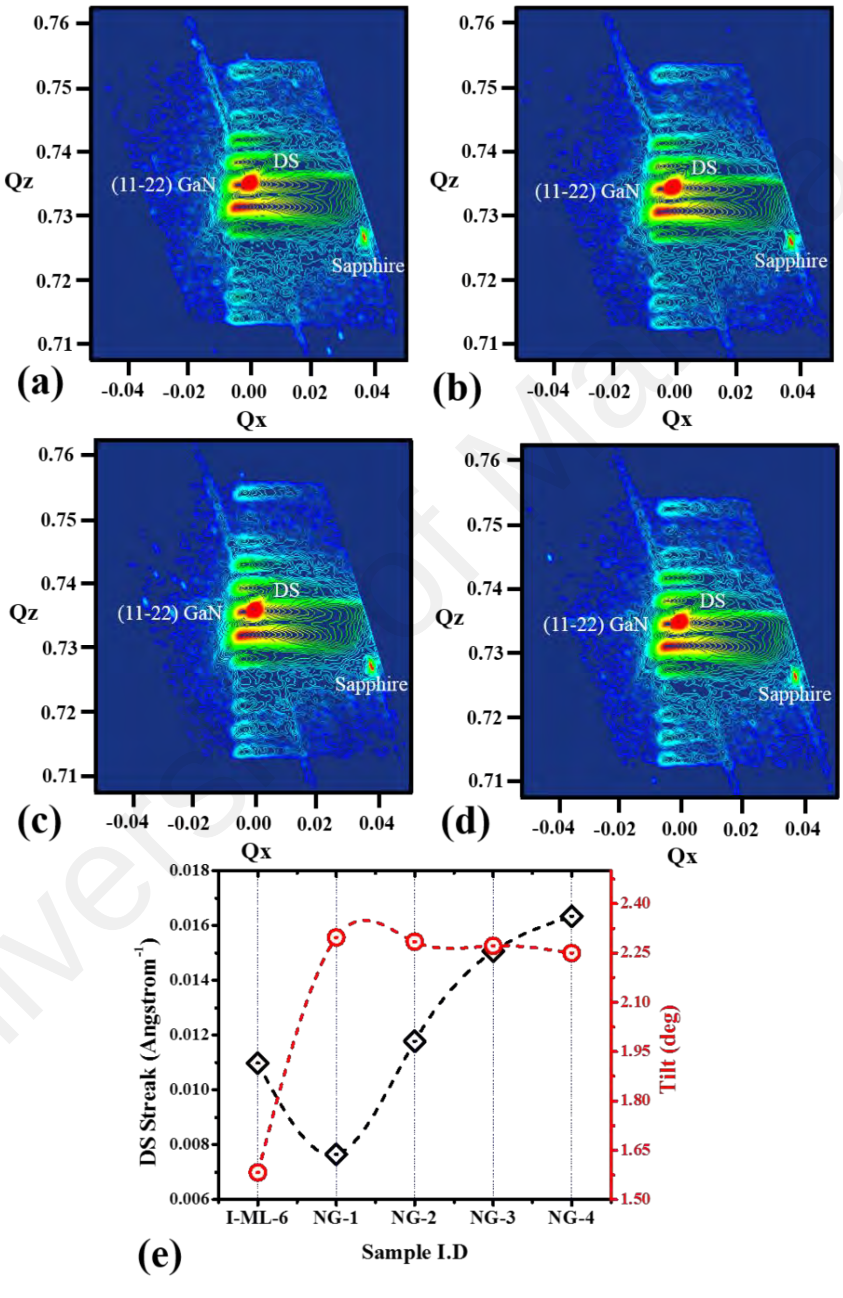


**Figure 6.4: XRD reciprocal space maps along [-1-123] of (a) NG-1, (b) NG-2, (c) NG-3, (d) NG-4 and (e) the DS streak and tilt plot of all NG samples with comparison to I-ML-6.**

RSM Measurements along [-1-123] as depicted in Figure 6.4 shows similar plots altogether. Only after detailed analysis of the GaN peak reveals slight differences as in Figure 6.4(e). The DS streak of 0.0089 Å-1 was observed being the lowest which correspond to NG-1 and highest elongation of 0.0135 Å-1 corresponds to NG-4. The tilt measurements however, portrayed slight variations of ~ 0.001° which fall within the measurement error (negligible) hence tilt indifferences are considered absent signifying similar state of relaxation as well as MD density. The analysis suggests that with low (5 sccm) disilane doping, the n-GaN epilayer would exert similar anisotropic behavior as the underlying Uid-GaN epilayer with slight enhancement. However, if excessive disilane flux (20 sccm) was utilized, significant crystal deterioration would be realized via increased defect densities including BSFs, PSFs, partial and perfect dislocations.

### 6.1.3 Morphological properties of Dissimilar $Si_2H_6$ flow

Morphological analysis was further conducted as to ensure surface properties were maintained without any deteriorations. Surface degradation would perturb the contacts deposition during the device fabrications. Figure 6.5 presents the 10×10 μm AFM images of all four n-GaN samples with its respective average line profiles. All the n-GaN samples portrayed similar undulated features with slightly dissimilar striation density. NG-1 exhibit short striation lengths corresponds to the fork-ridge features being still present with significantly low density and height, similar to the previous I-ML-6 surface features. The surface RMS roughness was slightly increased to 3.63 nm compared with I-ML-6 with similar peak-to-valley height of ~ 11 nm (from the average line profile) wherein I-ML-6 exhibited a peak-to-valley height of ~ 10 nm. As the disilane flow was increased to 10 sccm, NG-2 portrayed slight increase in the striations length. The average line profile suggests higher peak-to-valley height of ~ 16 nm which corresponds to the heightened undulations. Such phenomenon results in the increase of surface RMS roughness to ~ 5.19 nm. Furthermore, NG-3 and NG-4 portrayed significant elongation of the striations with absence of the short-length striated undulations. The difference between NG-3 and NG-4 can be observed within the density of the striations, and height of the peak-to-valley. NG-4 portrayed minor striation density with highest peak-to-valley height of ~21 nm, whilst NG-3 exert slightly higher density of striations with lower peak-to-valley height of ~15nm. In addition, NG-4 exhibited a widened valley width between two adjacent striated peaks compared with NG-3 as observed in their respective images as well as their corresponding average line profiles. The results indicate that the higher disilane flow endured considerable impact towards the morphological degradation which increased the undulation length and heights.

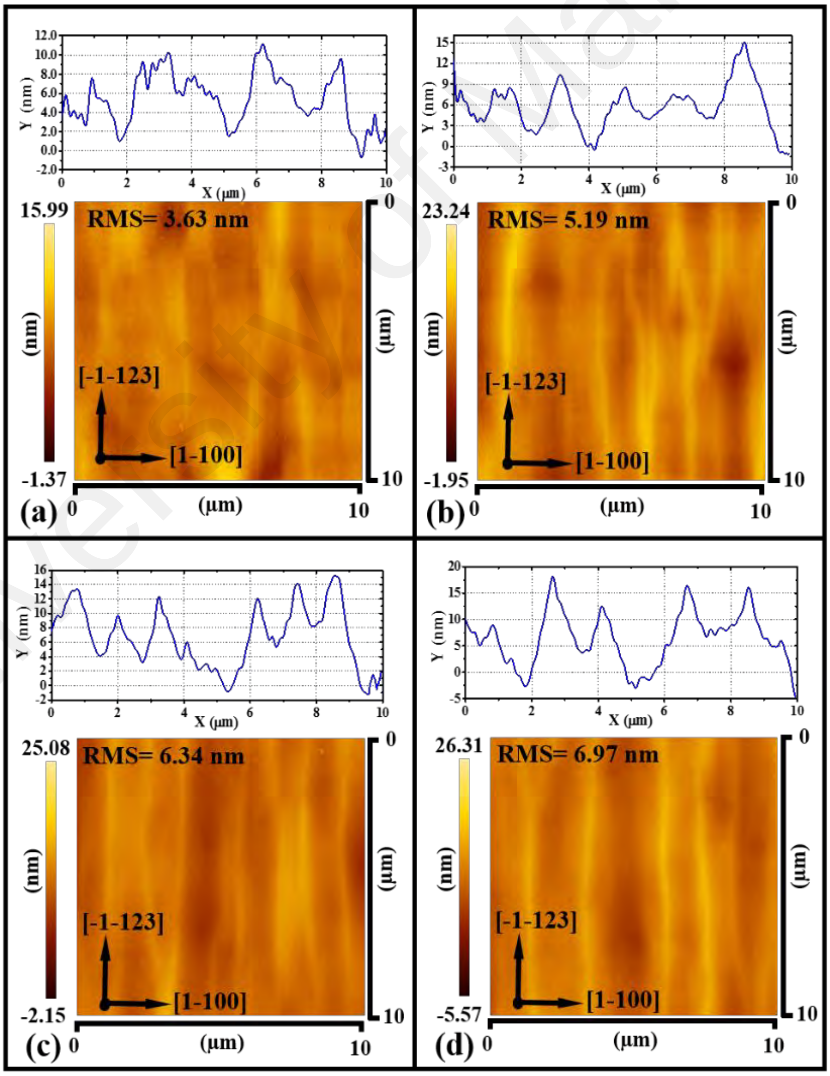


**Figure 6.5: 10×10µm AFM images as well as the average line profile of (a) NG-1, (b) NG-2, (c) NG-3 and (d) NG-4.**

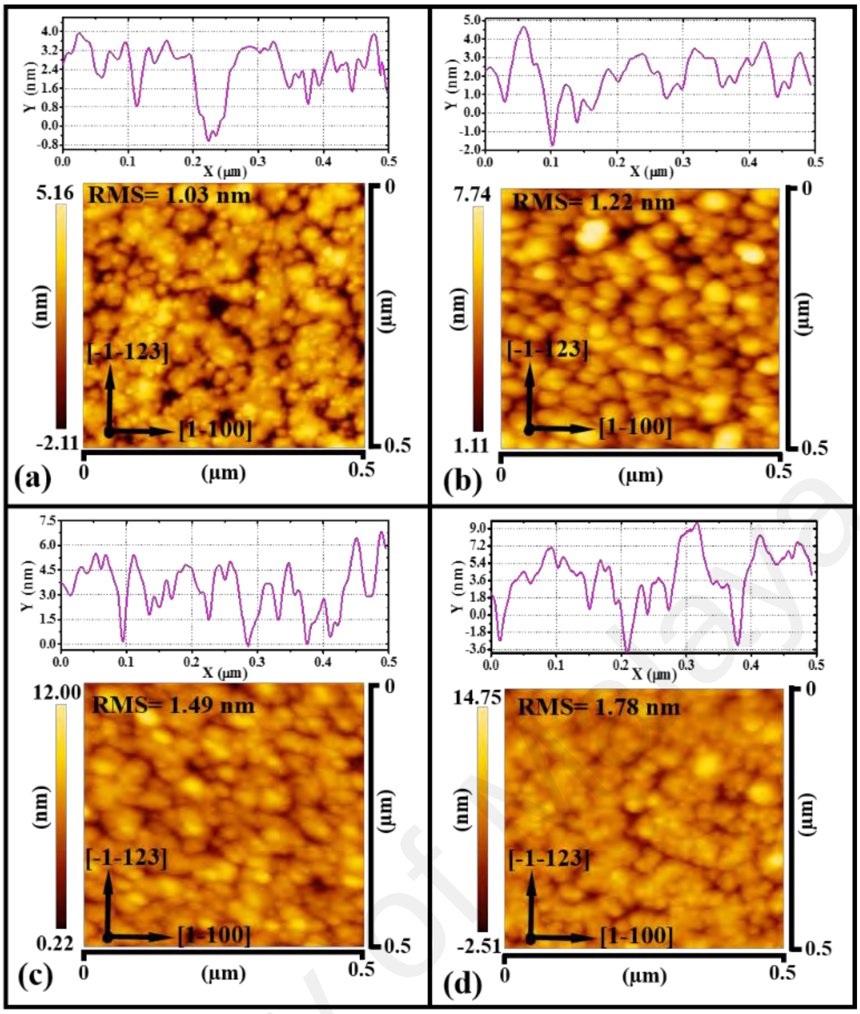


**Figure 6.6: 0.5×0.5μm AFM images with the corresponding average line profile of (a) NG-1, (b) NG-2, (c) NG-3 and (d) NG-4**

Since an occurrence of surface evolution in the larger scan sizes was evidently observed, lower scan sizes of 0.5×0.5 μm should portray similar behavior. Figure 6.6 depicts the 0.5×0.5 μm AFM images of all n-GaN samples revealing lower scale terrace-steps deviation with different disilane flux. NG-1 exhibited formations of various terrace sizes forming s highly irregular terrace arrangements with numerous voids present. However, the voids formed were shallow in depth as observed in the average line profiles indicating peak-to-valley of ~5nm. Furthermore, such voids are not interconnected with each other causing the absence of an elongated valley formations. Additionally, higher disilane flux of 10 sccm (NG-2) exhibited rearrangement of the terrace sizes with larger void sizes being formed. The terrace-steps configuration with the use of 15 sccm of disilane flux (NG-3) was further enhanced whereby the terrace sizes were predominantly average in sizes without the presence of outliers (significantly small or significantly large). The void existence was also slightly diminished compared with NG-1 and NG-2. However, a heightened peak was observed igniting higher terrace heights were formed resulting the heightened peak-to-valley length of ~7 nm. Conversely, the use of higher disilane flux of 20 sccm (NG-4) have shown to exert an unusual terrace formation. The terrace-steps were abnormally distributed with presence of numerous terrace sizes which constitutes the generation of lengthy valleys (as highlighted) caused from significant difference in the terrace-steps heights. Despite all mentioned above, the surface morphology of the n-GaN grown on the I-ML-6 template have shown a correlation between the disilane flux towards maintaining the surface properties of the underlying Uid-GaN epilayer. If the disilane flux were excessively flowed, then the terrace-steps configuration would be perturbed resulting in higher undulated features in the microscale.

### 6.1.4 Impact of Dissimilar $Si_2H_6$ flow on the Electrical Properties

Detailed analysis on the matter required the use of a room temperature Hall Effect measurement to apprehend the electrical properties exhibited by the n-GaN samples variants. Figure 6.7 presents the carrier concentration plot with its corresponding carrier mobility. From the figure, it can be deduced that a linear increase in the carrier concentration with linear increase of the disilane flux. Such trend was well suspected as the increase in disilane flux would elevate the carrier concentration due to the presence of higher number of Si atoms enabled to adhere and dope the GaN epilayer. However, the carrier mobility portrayed similar trend in linear increment until 15 sccm of disilane flux. Further elevating the disilane flux to 20 sccm has proven to degrade the carrier mobility as observed from the figure.

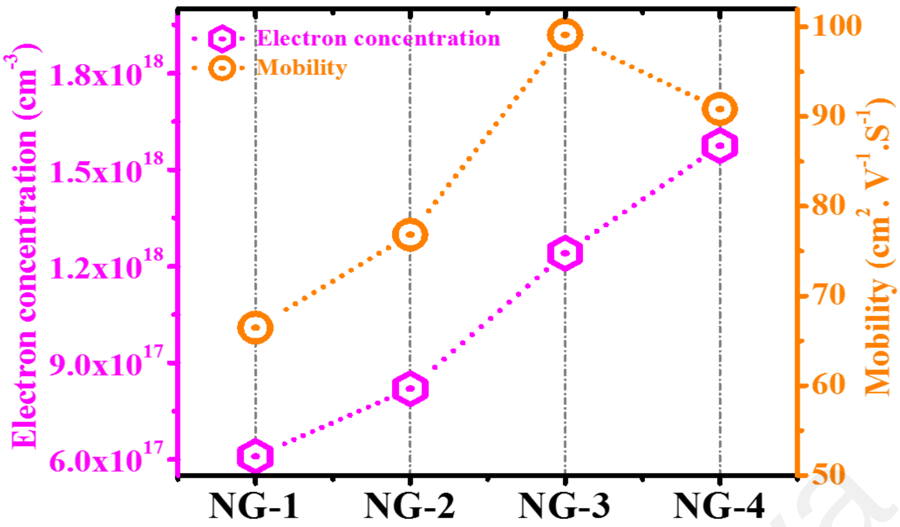


**Figure 6.7: Hall measurement of the n-GaN samples revealing its respective carrier concentrations and mobilities.**

Studies have reported on the principles regarding the different/fluctuations of the crystal and surface property as well as the electrical property of n-GaN epilayer in correlations to the dissimilar Si-doping mechanism due to different Si-doping source such as silane (Dai et al., 2017), disilane (Cantu et al., 2003) or in some cases tetraethylesilane (TESi) (Jo et al., 2017). It is known that the carrier concentrations of n-GaN epilayer would depend highly on the Si-doping source (which in this case disilane). Higher disilane flux would endure higher carrier concentration with an exception of utilization of a different template. However, the carrier mobility would not exactly obey such phenomenon due the dependent of the Si-doping probability. Reports have shown that with excessive doping concentrations, would exhibit increased ionized impurity scattering centers due to the dominance Si substitution of Ga atoms during the growth promoting the formation of $SiN_x$ dislocation sites (Liu et al., 2019; Yang et al., 2016). Such occurrence would then facilitates the generation of ionized Si impurities scattering centers. The main cause of such phenomenon would be attributed to the numerous dopant related dangling bonds would exist along the dislocations, generating acceptor traps which formed the negatively charged scattering centers (Dai et al., 2017).

Further utilization of the pre-optimized n-GaN samples would be realized in the device fabrication. However, since highly doped n-GaN would degrade the Schottky barrier (by introducing surface states), the lightly doped n-GaN (5 sccm) would be utilized as it is also observed that with lower doping concentration yielded the best crystal and attaining the smoothest surface for better Schottky contacts.

### 6.2 Metal-semiconductor-metal UV-photodetector

Within the final stage of the study, in order to relate all the existing optimizations conducted, the device fabrication of a UV-photodetector was commenced. The device fabrication would prove the impact of crystal quality and surface morphology towards the device performance where the response and recovery as well as the EQE measurement was evaluated. Two devices were constructed with the use of different templates. An additional lightly doped n-GaN sample was grown on the semi-polar (11-22) GaN with pre-optimized AlN NL and with the presence of 200 pairs of AlN/GaN I-ML (I-ML-6) which will now be designated as S-PD-2. The other sample was fabricated on the previous Uid-GaN template with the pre-optimized NL without the presence any defect reduction technique (NL-3) which will now be designated as S-PD-1. After the lightly doped n-GaN layer growth, a thin weakly doped (Uid-GaN) epilayer was grown as a buffer layer prior to the contact deposition. It was seen by few, that the use of such staggered structure will facilitate better device performance as highly doped absorbing layer would yield poor Schottky contact (Decoster & Harari, 2013). Since both the device were fabricated on templates with significant crystal and surface quality dissimilarities, therefore, the performance evaluation would be a direct impact of such properties.

### 6.2.1 Epilayer Growth and Device Fabrication

In the device fabrication, the two dissimilar templates were regrown with the same growth conditions including nitridation procedure, NL insertion, Uid-GaN epilayer, as well as lightly doped n-GaN layer whilst S-PD-2 also includes the use of I-ML-6 (200 alternating AlN/GaN I-ML).

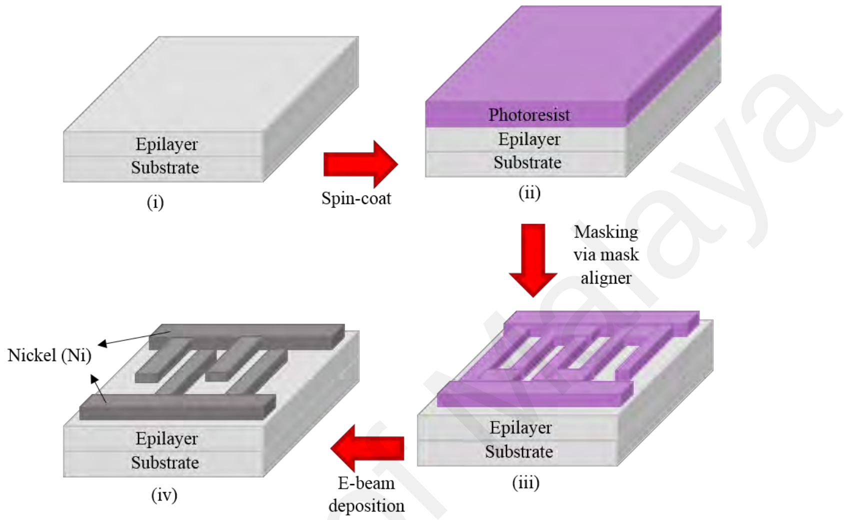


**Figure 6.8: Steps involved in the fabrication process of the devices.**

The device fabrication steps are as illustrated in Figure 6.8 where: (i) sample cleaning in acetone/propanol/DI water/$N_2$ drying and oven drying, (ii) photoresist deposition via spin-coater, (iii) lithography via mask aligner and removal of excess PR prior to optical microscope imaging (to ensure the performed masking was constructed correctly), (iv) contact deposition via e-beam and chemical lift-off of unwanted PR. The device fabrication was kept the same for both samples (S-PD-1 and S-PD-2) wherein the contact deposition was comprised of a Nickel (Ni) source. Additionally, both samples were simultaneously loaded within the e-beam chamber and contact deposition were conducted at the same time as the stage was large enough for more than one sample. This procedure ensures the exact same deposition conditions were attained as to avoid any additional factors contributing towards the device performance. Thickness and width of the metal contacts (fingers) were ~ 50 nm and ~ 60 nm respectively.

### 6.2.2 Device Performance Analysis of the Two Dissimilar Devices

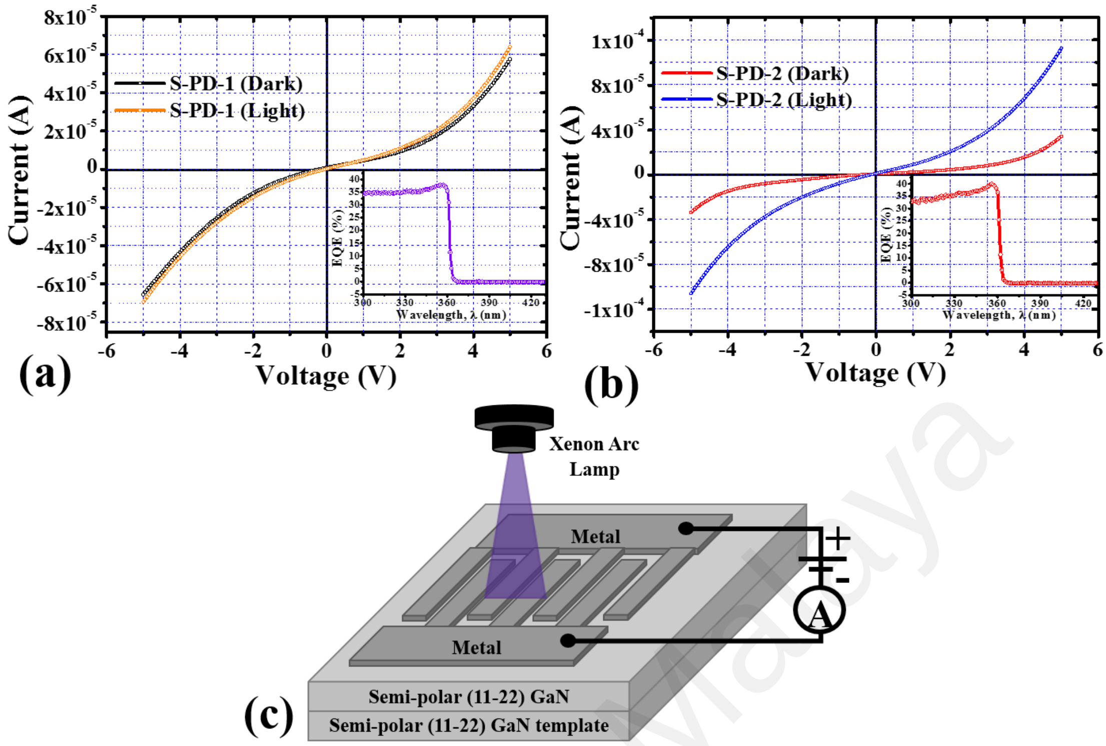


**Figure 6.9: I-V characteristics of (a) S-PD-1, (b) S-PD-2 and (c) the schematic setup of the measurement.**

As mentioned in the literature, the performance of a UV-photodetector can be evaluated via several techniques. The simplest approach would be the use of the common current-voltage (I-V) measurement. The measurement utilizes a dark chamber which comprises of UV-lamp source with shutter for light illumination measurement as depicted in the schematic setup of the measurement Figure 6.9(c). In the first part of the measurement, the dark current of the devices were measured at room temperature with bias voltage range of -5V to 5V. Figure 6.9(a-b) depicts the dark current measurement of S-PD-1 and S-PD-2 respectively, where both devices portrayed the Schottky nature of the devices (Velazquez et al., 2016). The inset showed the EQE percentage of both detectors with significant visible rejection of >360nm and minimum peak EQE of 38% at 358nm excitation. Note that the EQE values for both detectors showed similar behavior as both detector comprises of the same material composition, plane orientation (similar polarization) as well as contact electrode, hence similar EQE should be attained. Both devices exhibit a symmetric trend in the I-V characteristics at positive and negative biases which elucidates the properties of the symmetric contact electrode (Ni). If an asymmetric contact electrode was utilized, an asymmetric I-V curve would be yielded wherein the curve of the negative region would have dissimilar characteristics as the positive region (Jain et al., 2018).

At room temperature, the measured dark currents ($I_d$) for both S-PD-1 and S-PD-2 were 9.5 µA and 4.6 µA at bias voltage of 2V. S-PD-1 exhibited higher dark current which could be attributed from the higher defect state as compared with S-PD-2. As illumination occurs, the junction gives rise to the photocurrent as shown in Figure 6.9. S-PD-2 yielded significantly higher photocurrent ($I_{ph}$) compared with S-PD-1. The $I_{ph}$ was then further compared with its respective $I_d$ where S-PD-1 exhibit a very small indifferences between the $I_d$ and $I_{ph}$. S-PD-2 however, exhibited a large gap between the $I_{ph}$ and $I_d$. The small difference in the current under light and dark conditions has been reported to occur due to the tunneling of electrons from the GaN epilayer to the metal region which is caused by the defect states existence within the epilayer (Chang et al., 2008; Gundimeda et al., 2017; Jain et al., 2018). Such phenomenon will contribute to higher dark current and compromises the device performance. In some cases, higher dark current would also be affected by the Schottky barrier height ($\Phi$), wherein dissimilar metal contacts were utilized giving variations of $\Phi$ (Jain et al., 2018; Velazquez et al., 2016). However, in this work, as the same metal contact was used. Therefore, the only contributing factor towards the dissimilarities regarding the device performance would more likely be due to the defect states.

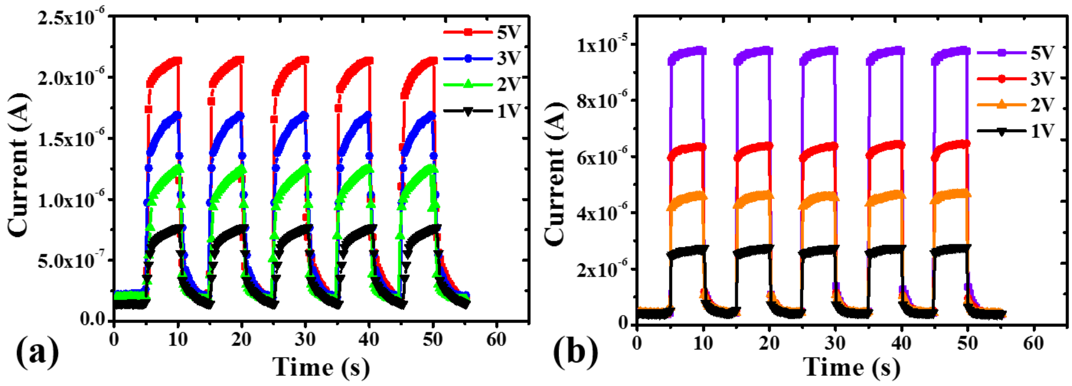


**Figure 6.10: Temporal response with different bias of (a) S-PD-1 and (b) S-PD-2.**

Further evaluation of the device was conducted by periodically opening (ON) and closing the UV lamp source shutter whilst measuring the $I_{ph}$. Figure 6.10 depicts the voltage-dependent photoresponse of the detectors under UV illuminations with different bias (1V-5V). S-PD-2 exhibited enhanced stability as well as repeatability over time. As illumination occurs, a rise in the $I_{ph}$ was observed whilst rapidly approaching the saturation value. The maximum $I_{ph}$ at bias of 1V was around 27 μA and drastic increase of the $I_{ph}$ was observed at bias of 5V around 98 μA. The remarkable enhanced photocurrent would be attributed to the charge generation over recombination which leads to higher number of charge carriers with increased bias (Gundimeda et al., 2017). Additionally, the higher voltage bias aids the photo excited carriers collection towards the metal region further increasing the photocurrent (Chen et al., 2014).

On the other hand, S-PD-1 portrayed an unusual spectrum where a gradual increase in the $I_{ph}$ was observed over time. As the illumination was OFF, the photocurrent exhibited similar trend wherein the recovery of the photocurrent towards the minimum value was gradually decreasing over time. In addition, S-PD-1 exhibited substantially lower photo current for all applied bias. The difference in the maximum generated photocurrent was also halved as compared with S-PD-2. Even at 5V bias, the $I_{ph}$ generated was lower than 23 μA which was also attained with longer duration of illumination (5s). Studies have shown that the gradual increase of the photocurrent which results in the $I_{ph}$ curve is due to the delayed collection of the electron-hole pairs generated with distance apart from the metal fingers of the contacts (Guo et al., 2014; Hirsch, 1997).

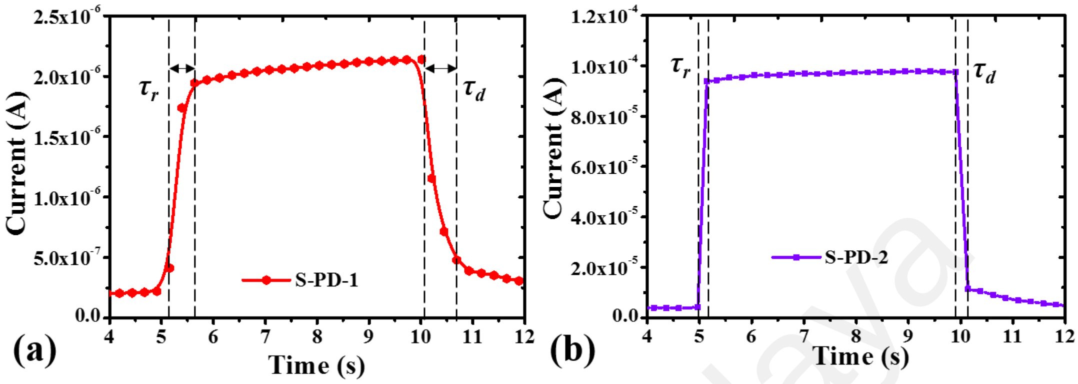


**Figure 6.11: The measured rise time ($\tau_r$) and fall/decay time ($\tau_d$) at 5V bias voltage for both (a) S-PD-1 and (b) S-PD-2.**

The temporal response of the device was further evaluated whilst measuring the response and recovery time. Figure 6.11 depicts the fitted photoresponse over time curve with respect to the experimental values to obtain the rise time ($\tau_r$) and decay time ($\tau_d$) for the detectors. The rise time and decay time of S-PD-2 was substantially shorter than S-PD-1 where $\tau_r$ and $\tau_d$ for S-PD-2 was ~ 170 and 241 ms whilst S-PD-1 exhibit $\tau_r$ and $\tau_d$ of ~ 480 and 914 ms respectively. The observable shorter response and recovery time of S-PD-2 indicates enhanced photoresponse is attained by S-PD-2 over its counterparts. The responsivity was further determined from the eq. (2.10) from the previous chapter and S-PD-1 yielded a responsivity of (117 mA/W) whilst s-PD-2 exhibit significant enhanced responsivity of (325 mA/W). The results of the device performance are well correlated with the previous optimizations. It can be observed that the higher crystalline quality of the epilayers attained by the I-ML insertion (200 pairings) have significantly boosted the device performance. Without the use of the I-MLs, the device performance deteriorated substantially.

**Table 6.1: Comparison with other MSM UV-photodetectors on polar (0002), non-polar (11-20) and (10-10) and semi-polar (11-22) GaN.**

| Type/Orientation | Metal contact | Responsivity (mA/W) | Rise/Fall time | Reference |
|---|---|---|---|---|
| non-polar (11-20) | Symmetric Gold (Au) | 340 | ~280 ms/~450 ms | (Gundimeda et al., 2017) |
| polar (0002) | Asymmetric Platinum Pt-Gold Au | 267 | - | (Jain et al., 2018) |
| non-polar (10-10) | Symmetric Gold (Au) | 407 | ~17.5 s/~35 s | (Mukundan et al., 2014) |
| semi-polar (11-22) | Symmetric Gold (Au) | 338 | ~25 s/~12.5 s | (Mukundan et al., 2014) |
| polycrystalline | Symmetric Nickel (Ni) | 7.31 | ~1.75 s/~1.87 s | (Zainal et al., 2020) |
| non-polar (11-20) | Symmetric Gold (Au) | 4.4 | ~1874 ms/3564 ms | (Mishra et al., 2018) |
| non-polar (11-20), nanostructure | Symmetric Gold (Au) | 25.9 | ~332 ms/~995 ms | (Mishra et al., 2018) |
| semi-polar (11-22) | Symmetric Nickel (Ni) | 325 | ~170 ms/~241 ms | This work |

Further comparison with other works with regards to semi-polar (11-22) oriented GaN-based MSM photodetectors were also conducted. The dark current of the S-PD-2 was comparable with previous report in semi-polar (11-22) GaN UV-photodetector (Mukundan et al., 2014). However, faster response time and recovery time was yielded by S-PD-2 of 170 ms and 241 ms respectively where the previous work reported the response time of 35 s and recovery time of 12.5 s (Mukundan et al., 2014). The S-PD-2 was also compared with recent non-polar GaN-based UV-photodetectors (Gundimeda et al., 2017; Mishra et al., 2018). Even with the use of symmetric Ni contacts, S-PD-2 exhibited remarkable enhancements especially the response and recovery time, over other non-polar UV photodetectors as reported by others.

It should be noted, that the results indicate successful integration of semi-polar (11-22) oriented GaN epilayers for MSM UV-photodetectors. However, with further optimizations of the device fabrications, the efficiencies of the device can be further enhanced. This would include the use of a current suppressing layer (buffer layer) with higher resistivity (Decoster & Harari, 2013; Xie et al., 2011) prior to the contact deposition or the contact electrode optimizations (utilizing additional metal such as gold) for enhanced Schottky junctions (Zainal et al., 2020). Integrating few additional buffer layers with higher resistivity prior to the electrode contacts deposition, or imbedding additional transition/absorbing/adaptation layers might also further reduce the dark current for enhanced device performance (Decoster & Harari, 2013). Furthermore, the growth of the epilayer conditions could also be implemented in the growth of different UV-photodetector structures such as the p-n or p-i-n photodetectors wherein the defect densities would impact the device performance significantly. Integration of the acquired high quality semi-polar (11-22) GaN epilayers with another device application can also be conducted for better device performance.

# CHAPTER 7: CONCLUSION AND FUTURE WORK

## 7.1 Conclusions

Semi-polar (11-22) GaN have been extensively studied in exploiting its remarkable advantages over its polar (c-plane) counterparts such as its reduced spontaneous and piezoelectric polarizations and increased doping capabilities. However, such exploitation was mainly focused on its advantages in the LED application rather than photosensing applications. Semi-polar (11-22) GaN based LEDs have shown remarkable device performance mainly owing to its exceptional advantages. Such remarkable properties, however, would only be beneficial upon acquiring acceptable crystallinity of the epilayers. Since enhanced semi-polar (11-22) epilayers were mainly attained with the use of advanced complex templates with pre-patterned $SiO_2$ masks or the use of highly expensive bulk semi-polar GaN substrates, the race in obtaining simpler cost-effective methods of producing high crystallinity epilayers via in-situ growth techniques have been numerously studied. Such occurrence is mainly owing to the high density of defects generation in semi-polar GaN orientation, such as BSFs, PSFs, partial and or perfect dislocations which propagates through the epilayers resulting in device performance degradation. This work demonstrates the importance of acquiring high crystallinity of the epilayers which constitutes better device performance. As the work was divided in few phases, mainly focusing on step-by-step approach for acquiring single-phase semi-polar (11-22) GaN epilayer, implying in-situ defect reduction techniques and fabrication of semi-polar (11-22) GaN-based UV-photodetector, the summary of the findings are also divided in few section.

The first part of the work signifies the importance of acquiring the single crystal semi-polar (11-22) GaN epilayer whilst eliminating other crystallographic planes such as (10-13) and (10-10). Since the growth of the semi-polar (11-22) GaN epilayer was conducted with the use of planar m-plane sapphire, few crucial steps must be addressed. The findings indicate the significance of substrate pre-treatment in ammonia ($NH_3$) ambience (or also known as nitridation procedure) at elevated temperature for considerable duration. Such procedure has shown to play a vital role in substituting oxygen atoms near the sapphire surface, forming nanosized protrusions which facilitates the tilting of the surface from m-plane (10-10) orientation to semi-polar (11-22) orientation. Absence of the nitridation procedure prior to the epilayer growth have resulted in mixed oriented epilayers inducing the three-dimensional growth mode, leading to highly poor crystallinity.

Upon acquiring the semi-polar (11-22) orientation, considerable attention needs to be paid within the growth conditions of the epilayer itself. The main concerns regarding the GaN epilayer growth in semi-polar orientation surrounds the Ga or N growth polarity of the resulting epilayer. For such condition, either the Ga source (TMG) or nitrogen source ($NH_3$) should be varied. In this work, the $NH_3$ was varied from 0.4 to 1.0 slm with the TMG fixed at 60 sccm. The result indicates significant variation in crystallinity with an intermediate $NH_3$ flux of 0.7 slm (V/III ratio of 115) exhibiting better crystal quality with lower presence of defects and dislocations as seen from the symmetric (on-axis) and asymmetric (off-axis) XRC measurements. The surface morphology of the higher crystallinity epilayer indicates considerable densities of the commonly known arrowhead like features (also known as the fork ridge features) as observed by AFM. In depth analysis of the surface at higher magnification reveals the distribution/arrangement of the atomic-sized terrace-steps features were considerably inhomogeneous. Voids between the terrace-steps induce the formation of elongated valleys which facilitates the lower magnification arrowhead-like features.

Further introducing the AlN nucleation layer proved to enhance the crystallinity of the subsequent Uid-GaN epilayer. However, controlling the growth conditions of the AlN NL was crucial as different conditions would deteriorate the crystallinity of the subsequent Uid-GaN epilayer. As the V/III ratio was reduced from 2527 to 1282, significant crystallinity evolution was recorded via the on-axis and off-axis XRC where the V/III ratio of 1282 (highest TMA flux of 98.5 sccm) yielded the least XRC FWHMs broadening, indicating enhanced crystal quality was attained. Defects and dislocations were significantly reduced and relaxation of the GaN epilayer was realized. Surface morphology was also enhanced wherein the densities of the arrowhead-like features receded with undulation heights significantly lowered to ~28 nm. Such occurrence was mainly owing to the better arrangement/distribution of the atomic-sized terrace-steps by which a reduction of the voids formation between the terraces induced lower density of elongated valley formations.

Introducing an in-situ single $NH_3$ etching procedure post NL growth prior to the thick Uid-GaN epilayer was seen to have deteriorate the crystal quality. The on-axis XRCs reveal significant broadenings in the FWHMs for either short or long duration of treatment time along both [-1-123] and [1-100]. Additionally, the considerably longer treatment time of 360 seconds yielded the worst crystallinity wherein a mixed orientation of the growth direction was recorded. $2\theta/\omega$ scans reveals the appearance of the (10-13) peak which ignites the growth orientation deviation from the single crystal (11-22) orientation. Off-axis XRCs further reveals an amplified broadening in the FWHMs, for all treatment time indicating enhanced defect and dislocation generation, rather than reduction. Morphological analysis reveals that the single $NH_3$ treatment amplified the densities of the arrowhead-like features. The width of the arrowheads was significantly lowered, inducing significant increase in the numbers of arrowheads within a small area. Further evaluation of the surface at higher magnification scans indicates deepened void formations near the terrace-steps with highly irregular terrace size distributions. The single $NH_3$ treatment was shown to disintegrate the crystalline quality of the subsequent

Uid-GaN epilayer resulting in the increase of arrowhead-like features as compared with the previous optimizations with the use of the $NH_3$ treatment.

Altering the parameters of the $NH_3$ treatment from single to multiple treatment durations however improved the crystallinity of the subsequent Uid-GaN epilayer significantly. The on-axis XRC reveals significant reduction in the anisotropic property where the XRC FWHM along [-1-123] and [1-100] was 0.15° (540 arcsec) and 0.33° (1188 arcsec) respectively, with the use of 40 alternates of treatments. Off-axis XRCs however, reveals that the multiple $NH_3$ treatment approach would enable significant reduction in certain types of defects and dislocations namely, the PSFs, partial and perfect dislocation with a c-axis component. The morphological property on the other hand portrayed considerable reduction in the density of the arrowhead features. The width of the arrowheads was significantly broadened resulting in the reduced density within the scanned area (similar scanned area as previous single treatment approach). However, the undulation-induced arrowhead features were increased to ~32 nm in height leading to a higher surface RMS roughness of 13.57 nm.

Since the use of multiple $NH_3$ treatment approach was found to enhance the crystallinity of the subsequent Uid-GaN epilayer with specific defect and dislocations reductions, an additional in-situ defect reduction technique was implemented to further enhance the crystallinity of the epilayers whilst also addressing the morphological qualities. The approach was conducted via utilizing the same exact growth conditions of the multiple treatment whilst substituting the treatment step with the growth of a thin AlN interlayer (with the same growth conditions of the AlN NL). The alternations were varied from 20 to 200 alternates which reveals a variation in the crystal and morphological properties of the subsequent Uid-GaN epilayers. On axis XRC reveals exceptional reduction in the anisotropic properties where the FWHM broadening along [-1-123] and

[1-100] was recorded at 0.11° (396 arcsec) and 0.21° (756 arcsec) for the Uid-GaN with 200 pairs of AlN/GaN inter-multilayers (I-MLs). Remarkable narrowing in the off-axis XRC FWHMs in the (n0-n0) series were also observed for the 200 pairs of I-MLs, where the FWHM along (10-10) and (20-20) was recorded to be around 0.20° (720 arcsec) and 0.18° (648 arcsec) respectively. Such narrowing of the FWHM in the (n0-n0) series was scarcely evident from the previous optimizations, even with the use of the multiple $NH_3$ treatments. Additionally, the surface morphological properties were also far more superior than the previous optimizations where the arrowhead-like features were evidently absent. The undulation-induced arrowheads were significantly reduced with remarkably low peak-to-valley heights of ~10 nm. The terrace-steps were also remarkable arranged with terrace sizes homogenously distributed resulting in the significantly improved surface properties of the subsequent Uid-GaN epilayer. The remarkable enhancement in the crystal and morphological properties of the Uid-GaN was further evaluated via TEM measurements elucidating the defect reduction occurred mainly owing to the presence of the I-MLs. Interaction between the defects (BSFs, PSFs, partial and perfect dislocations) evidently occurred which aids in the termination and annihilation of the defects leading to a unison propagation of the defects and dislocation. The occurrence of such phenomenon leads to the reduction of the defects propagating through the Uid-GaN epilayer. In addition, higher number of I-MLs alternates induce higher propagation union of the defects which facilitates higher degree of reduction in the defects enabled to enter the Uid-GaN epilayer.

Further growth of an n-GaN epilayer as a prior to the thin GaN buffer layer for device fabrication was conducted as to ensure lightly doped n-GaN epilayer was attained. Optimization of the n-GaN epilayer was conducted with variation in the disilane ($Si_2H_6$) flux from 5 to 20 sccm. XRC analysis indicates crystal deterioration would occur with highly doped n-GaN. Such deterioration would be unfavorable as the higher defect densities would perturb the device performance. Low disilane flow of 5 sccm however, slightly improved the crystallinity with lower anisotropic property as observed in the on- and off-axis XRCs. Surface property on the other hand, was maintained with low disilane flux ensuring low to none degradation of the epilayer prior to the device fabrication.

As all the optimization of the epilayers growth conditions was realized, the UV-photodetector device fabrication was commenced on two dissimilar templates namely: with and without the presence of the I-ML (200 pairs of AlN/GaN). The symmetric I-V characteristics of both devices indicate successful integration of the semi-polar (11-22) epilayers with an MSM UV-photodetector structure. Both devices exhibit similar peak absorption wavelength of 358 nm. However, the device fabricated on the template with higher crystal quality (with 200 alternates of I-ML) exhibited lower dark current of 4.6 μA compared to 9.5 μA at 2 V bias voltage exhibited by the other device with lower crystal quality (without I-MLs, on NL-3 template). Higher photocurrent was also observed for photodetector with higher crystal quality with increasing bias during the presence of illuminations. The response and recovery time yielded by the higher crystallinity template was around 170 and 240 ms respectively, compared with 480 and 914 ms of response and recovery time exhibited by the other device (S-PD-1). The responsivity of was almost doubled for the device with I-ML of 200 alternates (S-PD-2) of ~ 325 mA/W. The results indicate enhanced semi-polar (11-22) GaN-based UV photodetector was achieved with the use of an enhanced semi-polar template. The higher crystal quality exhibited by the semi-polar (11-22) template with the insertion of an in-situ defect reduction technique consisting of an inter-multilayer (I-ML) portrayed enhanced responsivity and fast response time ever for semi-polar (11-22) GaN UV photodetecting application.

## 7.2 Future works

Although the high crystalline quality of the bulk GaN epilayer was achieved via utilization of I-MLs (with significantly higher periods) approach, various additional crystal quality enhancement technique can be further imbedded within the structure as mentioned in the previous chapter. In addition, various other device application can be implemented on the pre-optimized semi-polar (11-22) GaN templates such LEDs, LDs, HEMTs, HFETs as well as solar cells as the main pre-requisite for such devices require high quality crystal and morphological properties. Furthermore, for the UV-photodetector device application, numerous additional optimizations can be conducted in realizing an enhanced device performance, such as growth of additional adaptation/absorbing/ transition/current-suppressing layers. The metal contacts deposition can also be further optimized for enhanced Schottky contact. The interdigitated fingers of the electrode's optimization can also be conducted with lower finger width for better photo-generated carrier collection. In addition, semi-polar (11-22) AlGaN deep UV-photodetectors have yet been reported. By realizing the ternary group AlGaN growth in the semi-polar (11-22) orientation for UV-sensing application, bandwidth tuning can also be achieved with reduced polarization fields. The future goals would also include challenging the device performance of polar c-plane oriented GaN based UV-photodetectors via integration of the acquired epilayers with dissimilar UV-photodetector device structures such as the more advanced structures achieved in p-i-n structures.

This work opens up the potential exploitation of the semi-polar (11-22) oriented Ga, Al, In, AlGaN materials for UV-photosensing with bandwidth tuning capabilities application.

## REFERENCES


Akasaki, I., Amano, H., Koide, Y., Hiramatsu, K., & Sawaki, N. (1989). Effects of ain buffer layer on crystallographic structure and on electrical and optical properties of GaN and $Ga_{1-x}Al_xN$ ($0<x\leq0.4$) films grown on sapphire substrate by MOVPE. *Journal of Crystal Growth, 98*(1-2), 209-219.

Alhassan, A. I., Farrell, R. M., Saifaddin, B., Mughal, A., Wu, F., DenBaars, S. P., . . . Speck, J. S. (2016). High luminous efficacy green light-emitting diodes with AlGaN cap layer. *Optics express, 24*(16), 17868-17873.

Bai, J., Gong, Y., Li, Z., Zhang, Y., & Wang, T. (2018). Semi-polar InGaN/GaN multiple quantum well solar cells with spectral response at up to 560 nm. *Solar Energy Materials and Solar Cells, 175*, 47-51.

Baik, K. H., Seo, Y. G., Hong, S.-K., Lee, S., Kim, J., Son, J.-S., & Hwang, S.-M. (2010). Effects of Basal Stacking Faults on Electrical Anisotropy of Nonpolar a-Plane (11-20) GaN Light-Emitting Diodes on Sapphire Substrate. *IEEE Photonics Technology Letters, 22*(9), 595-597.

Baker, T. J., Haskell, B. A., Wu, F., Speck, J. S., & Nakamura, S. (2006). Characterization of planar semipolar gallium nitride films on sapphire substrates. *Japanese Journal of Applied Physics, 45*(2L), Article#L154.

Bernardini, F., Fiorentini, V., & Vanderbilt, D. (1997). Spontaneous polarization and piezoelectric constants of III-V nitrides. *Physical Review B, 56*(16), Article#R10024.

Bougrioua, Z., Laügt, M., Vennéguès, P., Cestier, I., Gühne, T., Frayssinet, E., . . . Leroux, M. (2007). Reduction of stacking faults in (11-20) and (11-22) GaN films by ELO techniques and benefit on GaN wells emission. *Physica Status Solidi (a), 204*(1), 282-289.

Caliebe, M., Han, Y., Hocker, M., Meisch, T., Humphreys, C., Thonke, K., & Scholz, F. (2016). Growth and coalescence studies of oriented GaN on pre-structured sapphire substrates using marker layers. *Physica Status Solidi (b), 253*(1), 46-53.

Caliebe, M., Meisch, T., Madel, M., & Scholz, F. (2015). Effects of miscut of prestructured sapphire substrates and MOVPE growth conditions on (11-22) oriented GaN. *Journal of Crystal Growth, 414*, 100-104.

Cantu, P., Wu, F., Waltereit, P., Keller, S., Romanov, A., Mishra, U., . . . Speck, J. (2003). Si doping effect on strain reduction in compressively strained $Al_{0.49}$ $Ga_{0.51}N$ thin films. *Applied Physics Letters, 83*(4), 674-676.

Chakraborty, A., Baker, T. J., Haskell, B. A., Wu, F., Speck, J. S., Denbaars, S. P., . . . Mishra, U. K. (2005). Milliwatt power blue InGaN/GaN light-emitting diodes on semipolar GaN templates. *Japanese Journal of Applied Physics, 44*(7L), Article#L945.

Chakraborty, A., Haskell, B. A., Keller, S., Speck, J. S., Denbaars, S. P., Nakamura, S., & Mishra, U. K. (2005). Demonstration of nonpolar m-plane InGaN/GaN light-emitting diodes on free-standing m-plane GaN substrates. *Japanese Journal of Applied Physics, 44*(1L), Article#L173.

Chang, S.-H., Fang, Y.-K., Hsu, K.-C., & Wei, T.-C. (2008). GaN UV MSM photodetector on porous β-SiC/(1 1 1) Si substrates. *Sensors and Actuators A: Physical, 147*(1), 1-5.

Chang, S.-J., Ko, T., Sheu, J.-K., Shei, S.-C., Lai, W.-C., Chiou, Y., . . . Shen, C. (2007). AlGaN ultraviolet metal-semiconductor-metal photodetectors grown on Si substrates. *Sensors and Actuators A: Physical, 135*(2), 502-506.

Chen, Y., Lu, H., Wang, G., Chen, D., Ren, F., Zhang, R., & Zheng, Y. (2014). Metal-semiconductor-metal ultraviolet photodetectors directly fabricated on semi-insulating GaN: Fe template grown by hydride vapor phase epitaxy. *Sensors and Actuators A: Physical, 216*, 308-311.

Chèze, C., Sawicka, M., Siekacz, M., Turski, H., Cywiński, G., Smalc-Koziorowska, J., . . . Boćkowski, M. (2013). Step-flow growth mode instability of N-polar GaN under N-excess. *Applied Physics Letters, 103*(7), Article#071601.

Dadgar, A., Ravash, R., Veit, P., Schmidt, G., Müller, M., Dempewolf, A., . . . Krost, A. (2011). Eliminating stacking faults in semi-polar GaN by AlN interlayers. *Applied Physics Letters, 99*(2), Article#021905.

Dahal, R., Pantha, B., Li, J., Lin, J., & Jiang, H. (2009). InGaN/GaN multiple quantum well solar cells with long operating wavelengths. *Applied Physics Letters, 94*(6), Article#063505.

Dai, Q., Zhang, X., Zhao, J., Luan, H., Liang, Z., & Cui, Y. (2017). Effects of Si-doping on characteristics of semi-polar (11-22) plane $Al_{0.45}Ga_{0.55}N$ epi-layers. *Materials Science in Semiconductor Processing, 58*, 30-33.

Das, A., Magalhaes, S., Kotsar, Y., Kandaswamy, P., Gayral, B., Lorenz, K., . . . Monroy, E. (2010). Indium kinetics during the plasma-assisted molecular beam epitaxy of semipolar (11-22) InGaN layers. *Applied Physics Letters, 96*(18), Article#181907.

Dasilva, Y. A. R., Chauvat, M.-P., Ruterana, P., Lahourcade, L., Monroy, E., & Nataf, G. (2010). Defect structure in heteroepitaxial semipolar (11-22) (Ga, Al)N. *Journal of Physics: Condensed Matter, 22*(35), Article#355802.

Davidsson, S., Fälth, J., Liu, X., Zirath, H., & Andersson, T. (2005). Effect of AlN nucleation layer on the structural properties of bulk GaN grown on sapphire by molecular-beam epitaxy: *Journal of Applied Physics*, 98, Article#016109.

De Mierry, P., Guehne, T., Nemoz, M., Chenot, S., Beraudo, E., & Nataf, G. (2009). Comparison between polar (0001) and semipolar (11-22) nitride blue–green light-emitting diodes grown on c-and m-plane sapphire substrates. *Japanese Journal of Applied Physics, 48*(3R), Article#031002.

Decoster, D., & Harari, J. (2013). *Optoelectronic sensors*. London, England: John Wiley & Sons.

Diffey, B. L. (2002). Human exposure to solar ultraviolet radiation. *Journal of Cosmetic Dermatology, 1*(3), 124-130.

Dinh, D. V., Conroy, M., Zubialevich, V., Petkov, N., Holmes, J., & Parbrook, P. (2015). Single phase (11-22) AlN grown on (10-10) sapphire by metalorganic vapour phase epitaxy. *Journal of Crystal Growth, 414*, 94-99.

Dinh, D. V., Skuridina, D., Solopow, S., Frentrup, M., Pristovsek, M., Vogt, P., . . . Szczepańska, A. (2012). Growth and characterizations of semipolar (11-22) InN. *Journal of Applied Physics, 112*(1), Article#013530.

Drum, C. (1965). Intersecting faults on basal and prismatic planes in aluminium nitride. *Philosophical Magazine, 11*(110), 313-334.

Farrell, R., Young, E., Wu, F., DenBaars, S., & Speck, J. (2012). Materials and growth issues for high-performance nonpolar and semipolar light-emitting devices. *Semiconductor Science and Technology, 27*(2), Article#024001.

Frank, F., & Nicholas, J. (1953). CXXVIII. Stable dislocations in the common crystal lattices. *The London, Edinburgh, and Dublin Philosophical Magazine and Journal of Science, 44*(358), 1213-1235.

Frentrup, M., Ploch, S., Pristovsek, M., & Kneissl, M. (2011). Crystal orientation of GaN layers on (10-10) m-plane sapphire. *Physica Status Solidi (b), 248*(3), 583-587.

Fujita, M. (2013). Silicon photonics: Nanocavity brightens silicon. *Nature Photonics, 7*(4), 264-265.

Funato, M., Ueda, M., Kawakami, Y., Narukawa, Y., Kosugi, T., Takahashi, M., & Mukai, T. (2006). Blue, green, and amber InGaN/GaN light-emitting diodes on semipolar {11-22} GaN bulk substrates. *Japanese Journal of Applied Physics, 45*(7L), Article#L659.

Garrido, J., Monroy, E., Izpura, I., & Munoz, E. (1998). Photoconductive gain modelling of GaN photodetectors. *Semiconductor Science and Technology, 13*(6), Article#563.

Ghosh, S., Rivera, C., Pau, J., Muñoz, E., Brandt, O., & Grahn, H. (2007). Very narrow-band ultraviolet photodetection based on strained M-plane GaN films. *Applied Physics Letters, 90*(9), Article#091110.

Gil, B. (2014). *Physics of Wurtzite Nitrides and Oxides*. Switzerland: Springer, Cham.

Gundimeda, A., Krishna, S., Aggarwal, N., Sharma, A., Sharma, N. D., Maurya, K., . . . Gupta, G. (2017). Fabrication of non-polar GaN based highly responsive and fast UV photodetector. *Applied Physics Letters, 110*(10), Article#103507.

Guo, D., Wu, Z., An, Y., Guo, X., Chu, X., Sun, C., . . . Tang, W. (2014). Oxygen vacancy tuned Ohmic-Schottky conversion for enhanced performance in β-$Ga_2O_3$ solar-blind ultraviolet photodetectors. *Applied Physics Letters, 105*(2), Article#023507.

Hashimoto, R., Hwang, J., Saito, S., & Nunoue, S. (2014). High-efficiency yellow light-emitting diodes grown on sapphire (0001) substrates. *Physica Status Solidi (c), 11*(3-4), 628-631.

Hirano, A., Pernot, C., Iwaya, M., Detchprohm, T., Amano, H., & Akasaki, I. (2001). Demonstration of Flame Detection in Room Light Background by Solar-Blind AlGaN PIN Photodiode. *Physica Status Solidi (a), 188*(1), 293-296.

Hirsch, M. T., Wolk, J., Walukiewicz, W., & Haller, E. (1997). Persistent photoconductivity in n-type GaN. *Applied Physics Letters, 71*(8), 1098-1100.

Hsu, H.-C., Su, Y.-K., Huang, S.-J., Cheng, S.-H., & Cheng, C.-Y. (2011). Improvement of a-plane GaN crystalline quality by overgrowth of in situ etched GaN template. *Journal of Crystal Growth, 315*(1), 192-195.

Huang, K. M., Liang, S., Yeung, S., Oiyemhonlan, E., Cleveland, K. H., Parsa, C., . . . Huang, Y. (2017). Topically applied carvedilol attenuates solar ultraviolet radiation induced skin carcinogenesis. *Cancer Prevention Research, 10*(10), 598-606.

Hwang, J.-I., Hashimoto, R., Saito, S., & Nunoue, S. (2014). Development of InGaN-based red LED grown on (0001) polar surface. *Applied Physics Express, 7*(7), Article#071003.

Jain, S. K., Krishna, S., Aggarwal, N., Kumar, R., Gundimeda, A., Husale, S. C., . . . Gupta, G. (2018). Effect of Metal Contacts on a GaN/Sapphire-Based MSM Ultraviolet Photodetector. *Journal of Electronic Materials, 47*(10), 6086-6090.

Jang, J., Lee, K., Hwang, J., Jung, J., Lee, S., Lee, K., . . . Nam, O. (2012). Improvement of crystal quality and optical property in (11−22) semipolar InGaN/GaN LEDs grown on patterned m-plane sapphire substrate. *Journal of Crystal Growth, 361*, 166-170.

Jiang, Y., Li, Y., Li, Y., Deng, Z., Lu, T., Ma, Z., . . . Jia, H. (2015). Realization of high-luminous-efficiency InGaN light-emitting diodes in the "green gap" range. *Scientific reports, 5*, Article#10883.

Jo, M., Oshima, I., Matsumoto, T., Maeda, N., Kamata, N., & Hirayama, H. (2017). Structural and electrical properties of semipolar (11-22) AlGaN grown on m-plane (1-100) sapphire substrates. *Physica Status Solidi c, 14*(8), Article#1600248.

Johnston, C., Moram, M., Kappers, M., & Humphreys, C. (2009). Defect reduction in (11-22) semipolar GaN grown on m-plane sapphire using ScN interlayers. *Applied Physics Letters, 94*(16), Article#161109.

Jung, C., Jang, J., Hwang, J., Jeong, J., Kim, J., & Nam, O. (2013). Defect reduction in (11–22) semipolar GaN with embedded InN islands on m-plane sapphire. *Journal of Crystal Growth, 370*, 26-29.

Kioseoglou, J., Kalesaki, E., Lymperakis, L., Neugebauer, J., Komninou, P., & Karakostas, T. (2011). Electronic structure of 1/6 <20-23> partial dislocations in wurtzite GaN. *Journal of Applied Physics, 109*(8), Article#083511.

Komninou, P., Kioseoglou, J., Dimitrakopulos, G., Kehagias, T., & Karakostas, T. (2005). Partial dislocations in wurtzite GaN. *Physica Status Solidi (a), 202*(15), 2888-2899.

Kriouche, N., Vennéguès, P., Nemoz, M., Nataf, G., & De Mierry, P. (2010). Stacking faults blocking process in (11-22) semipolar GaN growth on sapphire using asymmetric lateral epitaxy. *Journal of Crystal Growth, 312*(19), 2625-2630.

Kumar, A., Latzel, M., Christiansen, S., Kumar, V., & Singh, R. (2015). Effect of rapid thermal annealing on barrier height and 1/f noise of Ni/GaN Schottky barrier diodes. *Applied Physics Letters, 107*(9), Article#093502.

Lacroix, B., Chauvat, M.-P., Ruterana, P., Nataf, G., & De Mierry, P. (2011). Efficient blocking of planar defects by prismatic stacking faults in semipolar (11-22)-GaN layers on m-sapphire by epitaxial lateral overgrowth. *Applied Physics Letters, 98*(12), Article#121916.

Lähnemann, J., Jahn, U., Brandt, O., Flissikowski, T., Dogan, P., & Grahn, H. T. (2014). Luminescence associated with stacking faults in GaN. *Journal of Physics D: Applied Physics, 47*(42), Article#423001.

Lahourcade, L., Bellet-Amalric, E., Monroy, E., Abouzaid, M., & Ruterana, P. (2007). Plasma-assisted molecular-beam epitaxy of Al N (11-22) on m sapphire. *Applied Physics Letters, 90*(13), Article#131909.

Lechner, L., Biskupek, J., & Kaiser, U. (2012). Improved focused ion beam target preparation of (S)TEM specimen—A method for obtaining ultrathin lamellae. *Microscopy and Microanalysis, 18*(2), 379-384.

Lee, M., Sheu, J., Lai, W., Chang, S.-J., Su, Y.-K., Chen, M., . . . Tsai, J. (2003). GaN Schottky barrier photodetectors with a low-temperature GaN cap layer. *Applied Physics Letters, 82*(17), 2913-2915.

Leszczynski, M., Teisseyre, H., Suski, T., Grzegory, I., Bockowski, M., Jun, J., . . . Foxon, C. (1996). Lattice parameters of gallium nitride. *Applied Physics Letters, 69*(1), 73-75.

Leung, B., Sun, Q., Yerino, C., Zhang, Y., Han, J., Kong, B. H., . . . Li, Y.-L. (2012). Growth evolution and microstructural characterization of semipolar (11-22) GaN selectively grown on etched r-plane sapphire. *Journal of Crystal Growth, 341*(1), 27-33.

Li, H., Khoury, M., Bonef, B., Alhassan, A. I., Mughal, A. J., Azimah, E., . . . Speck, J. S. (2017). Efficient semipolar (11–22) 550 nm Yellow/Green InGaN light-emitting diodes on low defect density (11–22) GaN/Sapphire templates. *ACS Applied Materials & Interfaces, 9*(41), 36417-36422.

Liu, S., Yang, J., Zhao, D., Jiang, D., Liang, F., Chen, P., . . . Xing, Y. (2019). The compensation role of deep defects in the electric properties of lightly Si-doped GaN. *Journal of Alloys and Compounds, 773*, 1182-1186.

Lu, L., Shen, B., Xu, F., Xu, J., Gao, B., Yang, Z., . . . Yu, D. (2007). Morphology of threading dislocations in high-resistivity GaN films observed by transmission electron microscopy. *Journal of Applied Physics, 102*(3), Article#033510.

Maruska, H. P., & Tietjen, J. (1969). The preparation and properties of vapor-deposited single-crystal-line GaN. *Applied Physics Letters, 15*(10), 327-329.

Matsumoto, K., Tokunaga, H., Ubukata, A., Ikenaga, K., Fukuda, Y., Tabuchi, T., . . . Uematsu, K. (2008). High growth rate metal organic vapor phase epitaxy GaN. *Journal of Crystal Growth, 310*(17), 3950-3952.

McLaurin, M. B., Hirai, A., Young, E., Wu, F., & Speck, J. S. (2008). Basal plane stacking-fault related anisotropy in X-ray rocking curve widths of m-plane GaN. *Japanese Journal of Applied Physics, 47*(7R), Article#5429.

Min, D., Yoo, G., Ryu, Y., Moon, S., Lee, K., & Nam, O. (2013). Improvement of crystal quality and optical property in (11-22) semipolar InGaN/GaN light emitting diodes grown on hemi-spherically patterned $SiO_2$ mask. *Journal Ceramic Processing Research, 14*, 521-524.

Min, D., Yoo, G., Ryu, Y., Moon, S., Nam, K., Lim, H., & Nam, O. (2013). Improved performance of (11-22) semipolar InGaN/GaN light-emitting diodes grown using a hemispherically patterned $SiO_2$ mask. *Japanese Journal of Applied Physics, 52*(10S), Article#10MA03.

Mishra, M., Gundimeda, A., Krishna, S., Aggarwal, N., Goswami, L., Gahtori, B., . . . Gupta, G. (2018). Surface-engineered nanostructure-based efficient nonpolar GaN ultraviolet photodetectors. *ACS Omega, 3*(2), 2304-2311.

Mogilatenko, A., Kirmse, H., Stellmach, J., Frentrup, M., Mehnke, F., Wernicke, T., . . . Weyers, M. (2014). Analysis of crystal orientation in AlN layers grown on m-plane sapphire. *Journal of Crystal Growth, 400*, 54-60.

Monavarian, M., Izyumskaya, N., Müller, M., Metzner, S., Veit, P., Can, N., . . . Christen, J. (2016). Improvement of optical quality of semipolar (11-22) GaN on m-plane sapphire by in-situ epitaxial lateral overgrowth. *Journal of Applied Physics, 119*(14), Article#145303.

Monroy, E., Calle, F., Munoz, E., Omnès, F., Beaumont, B., & Gibart, P. (1999). Visible-blindness in photoconductive and photovoltaic AlGaN ultraviolet detectors. *Journal of Electronic Materials, 28*(3), 240-245.

Moram, M., Johnston, C., Hollander, J., Kappers, M., & Humphreys, C. (2009). Understanding x-ray diffraction of nonpolar gallium nitride films. *Journal of Applied Physics, 105*(11), Article#113501.

Moram, M., & Vickers, M. (2009). X-ray diffraction of III-nitrides. *Reports on Progress in Physics, 72*(3), 036502.

Morkoç, H. (2009). *Handbook of nitride semiconductors and devices, Materials Properties, Physics and Growth* (Vol. 1). Weinheim, Germany: John Wiley & Sons.

Mou, W., Zhao, L., Chen, L., Yan, D., Ma, H., Yang, G., & Gu, X. (2017). GaN-based Schottky barrier ultraviolet photodetectors with graded doping on patterned sapphire substrates. *Solid-State Electronics, 133*, 78-82.

Mukundan, S., Mohan, L., Chandan, G., Roul, B., & Krupanidhi, S. (2014). Semipolar and nonpolar GaN epi-films grown on m-sapphire by plasma assisted molecular beam epitaxy. *Journal of Applied Physics, 116*(20), Article#204502.

Munoz, E., Monroy, E., Garrido, J., Izpura, I., Sánchez, F., Sánchez-Garcıa, M., . . . Gibart, P. (1997). Photoconductor gain mechanisms in GaN ultraviolet detectors. *Applied Physics Letters, 71*(7), 870-872.

Nakamura, S. (1991a). GaN growth using GaN buffer layer. *Japanese Journal of Applied Physics, 30*(10A), Article#L1705.

Nakamura, S., Senoh, M., Nagahama, S., Iwasa, N., & Yamada, T., (1996). Characteristics of InGaN multiquantum-well-structure laser diodes. *Applied Physics Letters 68*(23), Article#3269.

Nakamura, S., Harada, Y., & Seno, M. (1991b). Novel metalorganic chemical vapor deposition system for GaN growth. *Applied Physics Letters, 58*(18), 2021-2023.

Nakamura, S., Pearton, S., & Fasol, G. (2000). *The blue laser diode: The complete story*. Springer Science & Business Media.

Nakamura, S., Senoh, M., Iwasa, N., & Nagahama, S.-i. (1995). High-brightness InGaN blue, green and yellow light-emitting diodes with quantum well structures. *Japanese Journal of Applied Physics, 34*(7A), Article#L797.

Nasser, N., Zhen, Y. Z., Jiawei, L., & Bou, X. Y. (2001). GaN Heteroeptaxial growth techniques. *Journal of Microwaves, Optoelectronics and Electromagnetic Applications (JMOe), 2*(3), 22-31.

Ni, X., Özgür, Ü., Baski, A., Morkoç, H., Zhou, L., Smith, D. J., & Tran, C. (2007). Epitaxial lateral overgrowth of (11-22) semipolar GaN on (10-10) m-plane sapphire by metalorganic chemical vapor deposition. *Applied Physics Letters, 90*(18), Article#182109.

Northrup, J. E. (2009). GaN and InGaN (11 2_2) surfaces: Group-III adlayers and indium incorporation. *Applied Physics Letters, 95*(13), Article#133107.

Onuma, T., Okamoto, K., Ohta, H., & Chichibu, S. (2008). Anisotropic optical gain in m-plane $In_xGa_{1-x}N$/GaN multiple quantum well laser diode wafers fabricated on the low defect density freestanding GaN substrates. *Applied Physics Letters, 93*(9), Article#091112.

Ozbay, E., Biyikli, N., Kimukin, I., Kartaloglu, T., Tut, T., & Aytur, O. (2004). High-performance solar-blind photodetectors based on $Al_xGa_{1-x}N$ heterostructures. *IEEE Journal of Selected Topics in Quantum Electronics, 10*(4), 742-751.

Paisley, M., Sitar, Z., Posthill, J., & Davis, R. (1989). Growth of cubic phase gallium nitride by modified molecular-beam epitaxy. *Journal of Vacuum Science & Technology A: Vacuum, Surfaces, and Films, 7*(3), 701-705.

Park, S., Park, J., You, D.-J., Joo, K., Moon, D., Jang, J., . . . Song, Y.-K. (2012). Improved emission efficiency of a-plane GaN light emitting diodes with silica nano-spheres integrated into a-plane GaN buffer layer. *Applied Physics Letters, 100*(19), Article#191116.

Ploch, S., Frentrup, M., Wernicke, T., Pristovsek, M., Weyers, M., & Kneissl, M. (2010). Orientation control of GaN {11-22} and {10-1-3} grown on (10-10) sapphire by metal-organic vapor phase epitaxy. *Journal of Crystal Growth, 312*(15), 2171-2174.

Ploch, S., Wernicke, T., Dinh, D. V., Pristovsek, M., & Kneissl, M. (2012). Surface diffusion and layer morphology of (11-22) GaN grown by metal-organic vapor phase epitaxy. *Journal of Applied Physics, 111*(3), Article#033526.

Ponce, F., & Bour, D. (1997). Nitride-based semiconductors for blue and green light-emitting devices. *Nature, 386*(6623), 351-359.

Ponce, F. A. (1997). Defects and interfaces in GaN epitaxy. *MRS bulletin, 22*(2), 51-57.

Potin, V., Ruterana, P., & Nouet, G. (2000). HREM study of stacking faults in GaN layers grown over sapphire substrate. *Journal of Physics: Condensed Matter, 12*(49), Article#10301.

Potin, V., Ruterana, P., Nouet, G., Pond, R., & Morkoç, H. (2000). Mosaic growth of GaN on (0001) sapphire: A high-resolution electron microscopy and crystallographic study of threading dislocations from low-angle to high-angle grain boundaries. *Physical Review B, 61*(8), Article#5587.

Qian, H., Lee, K., Vajargah, S. H., Novikov, S., Guiney, I., Zaidi, Z., . . . Humphreys, C. (2017). Novel GaN-based vertical heterostructure field effect transistor structures using crystallographic KOH etching and overgrowth. *Journal of Crystal Growth, 459*, 185-188.

Rahman, M. M., & Hasan, N. (2016). Compound Semiconductor Epitaxial Growth Techniques. *International Journal of Thin Film Science and Techology, 5*, 45-49.

Romanov, A., Baker, T., & Nakamura, S. (2006). Strain-induced polarization in wurtzite III-nitride semipolar layers. *Journal of Applied Physics, 100*(2) Article#023522.

Rössler, U. (1969). Energy bands of hexagonal II-VI semiconductors. *Physical Review, 184*(3), 733-738.

Saito, M., Kamber, D. S., Baker, T. J., Fujito, K., DenBaars, S. P., Speck, J. S., & Nakamura, S. (2008). Plane dependent growth of GaN in supercritical basic ammonia. *Applied physics express, 1*(12), Article#121103.

Saito, S., Hashimoto, R., Hwang, J., & Nunoue, S. (2013). InGaN light-emitting diodes on c-face sapphire substrates in green gap spectral range. *Applied physics express, 6*(11), Article#111004.

Sakai, S., Wang, T., Morishima, Y., & Naoi, Y. (2000). A new method of reducing dislocation density in GaN layer grown on sapphire substrate by MOVPE. *Journal of Crystal Growth, 221*(1-4), 334-337.

Scholz, F., Meisch, T., Caliebe, M., Schörner, S., Thonke, K., Kirste, L., . . . Baumbach, T. (2014). Growth and doping of semipolar GaN grown on patterned sapphire substrates. *Journal of Crystal Growth, 405*, 97-101.

Scholz, H., & Thiemann, K. (1977). Crystal structure refinement in AIN and GaN. *Solid State Commun., 23*, 815-819.

Schwaiger, S., Metzner, S., Wunderer, T., Argut, I., Thalmair, J., Lipski, F., . . . Zweck, J. (2011). Growth and coalescence behavior of semipolar (11-22) GaN on pre-structured r-plane sapphire substrates. *Physica Status Solidi (b), 248*(3), 588-593.

Sharma, R., Pattison, P., Masui, H., Farrell, R., Baker, T., Haskell, B., . . . Nakamura, S. (2005). Demonstration of a semipolar (10-1-3) InGaN/ GaN green light emitting diode. *Applied Physics Letters, 87*(23), Article#231110.

Shen, C., Lee, C., Stegenburgs, E., Lerma, J. H., Ng, T. K., Nakamura, S., . . . Ooi, B. S. (2017). Semipolar III–nitride quantum well waveguide photodetector integrated with laser diode for on-chip photonic system. *Applied physics express, 10*(4), Article#042201.

Shen, W., & Kwok, H. (1994). Crystalline phases of II-VI compound semiconductors grown by pulsed laser deposition. *Applied Physics Letters, 65*(17), 2162-2164.

Sheu, J.-K., Chen, P.-C., Shin, C.-L., Lee, M.-L., Liao, P.-H., & Lai, W.-C. (2016). Manganese-doped AlGaN/GaN heterojunction solar cells with intermediate band absorption. *Solar Energy Materials and Solar Cells, 157*, 727-732.

Shioda, T., Yoshida, H., Tachibana, K., Sugiyama, N., & Nunoue, S. (2012). Enhanced light output power of green LEDs employing AlGaN interlayer in InGaN/GaN MQW structure on sapphire (0001) substrate. *Physica Status Solidi (a), 209*(3), 473-476.

Sizov, D. S., Bhat, R., Napierala, J., Gallinat, C., Song, K., & Zah, C.-e. (2009). 500-nm optical gain anisotropy of semipolar (11-22) InGaN quantum wells. *Applied Physics Express, 2*(7), 071001.

Smirnov, A., Young, E., Bougrov, V., Speck, J., & Romanov, A. (2016). Critical thickness for the formation of misfit dislocations originating from prismatic slip in semipolar and nonpolar III-nitride heterostructures. *APL Materials, 4*(1), Article#016105.

Song, K.-R., Oh, D.-S., & Lee, S.-N. (2013). Optical and crystal improvements of semipolar (11-22) GaN/m-sapphire by in-situ thermal etching process. *Current Applied Physics, 13*(8), 1643-1646.

Stampfl, C., & Van de Walle, C. G. (1998). Energetics and electronic structure of stacking faults in AlN, GaN, and InN. *Physical Review B, 57*(24), Article#R15052.

Stellmach, J., Frentrup, M., Mehnke, F., Pristovsek, M., Wernicke, T., & Kneissl, M. (2012). MOVPE growth of semipolar (11-22) AlN on m-plane (10-10) sapphire. *Journal of Crystal Growth, 355*(1), 59-62.

Strite, S., Ruan, J., Li, Z., Salvador, A., Chen, H., Smith, D. J., . . . Morkoc, H. (1991). An investigation of the properties of cubic GaN grown on GaAs by plasma-assisted molecular-beam epitaxy. *Journal of Vacuum Science & Technology B: Microelectronics and Nanometer Structures Processing, Measurement, and Phenomena, 9*(4), 1924-1929.

Strittmatter, A., Northrup, J. E., Johnson, N. M., Kisin, M. V., Spiberg, P., El-Ghoroury, H., . . . Syrkin, A. (2011). Semi-polar nitride surfaces and heterostructures. *Physica Status Solidi (b), 248*(3), 561-573.

Stuerzebecher, L., Harzendorf, T., Vogler, U., Zeitner, U. D., & Voelkel, R. (2010). Advanced mask aligner lithography: fabrication of periodic patterns using pinhole array mask and Talbot effect. *Optics express, 18*(19), 19485-19494.

Su, Y.-K., Chang, P.-C., Chen, C.-H., Chang, S.-J., Yu, C.-L., Lee, C.-T., . . . Wang, C. (2005). Nitride-based MSM UV photodetectors with photo-chemical annealing Schottky contacts. *Solid-State Electronics, 49*(3), 459-463.

Sun, Q., Cho, Y., Lee, I.-H., Han, J., Kong, B., & Cho, H. (2008). Nitrogen-polar GaN growth evolution on c-plane sapphire. *Applied Physics Letters, 93*(13), Article#131912.

Sun, Q., Ko, T.-S., Yerino, C. D., Zhang, Y., Lee, I.-H., Han, J., . . . Wang, S.-C. (2009a). Effect of controlled growth dynamics on the microstructure of nonpolar a-plane GaN revealed by X-ray diffraction. *Japanese Journal of Applied Physics, 48*(7R), Article#071002.

Sun, Q., Leung, B., Yerino, C. D., Zhang, Y., & Han, J. (2009b). Improving microstructural quality of semipolar (11-22) GaN on m-plane sapphire by a two-step growth process. *Applied Physics Letters, 95*(23), Article#231904.

Tendille, F., De Mierry, P., Vennéguès, P., Chenot, S., & Teisseire, M. (2014). Defect reduction method in (11-22) semipolar GaN grown on patterned sapphire substrate by MOCVD: Toward heteroepitaxial semipolar GaN free of basal stacking faults. *Journal of Crystal Growth, 404*, 177-183.

Tendille, F., Martin, D., Vennéguès, P., Grandjean, N., & De Mierry, P. (2016). Selective heteroepitaxy on deeply grooved substrate: A route to low cost semipolar GaN platforms of bulk quality. *Applied Physics Letters, 109*(8), Article#082101.

Tsai, M.-C., Yen, S.-H., Chang, S.-H., & Kuo, Y.-K. (2009). Effect of spontaneous and piezoelectric polarization on optical characteristics of ultraviolet AlGaInN light-emitting diodes. *Optics Communications, 282*(8), 1589-1592.

Tyagi, A., Wu, F., Young, E. C., Chakraborty, A., Ohta, H., Bhat, R., . . . Speck, J. S. (2009). Partial strain relaxation via misfit dislocation generation at heterointerfaces in (Al, In) GaN epitaxial layers grown on semipolar (11-22) GaN free standing substrates. *Applied Physics Letters, 95*(25), Article#251905.

Ueda, M., Kojima, K., Funato, M., Kawakami, Y., Narukawa, Y., & Mukai, T. (2006). Epitaxial growth and optical properties of semipolar (11-22) GaN and InGaN⁄ GaN quantum wells on GaN bulk substrates. *Applied Physics Letters, 89*(21), Article#211907.

Velazquez, R., Aldalbahi, A., Rivera, M., & Feng, P. (2016). Fabrications and application of single crystalline GaN for high-performance deep UV photodetectors. *AIP Advances, 6*(8), Article#085117.

Vennéguès, P. (2012). Defect reduction methods for III-nitride heteroepitaxial films grown along nonpolar and semipolar orientations. *Semiconductor Science and Technology, 27*(2), Article#024004.

Vennéguès, P., & Beaumont, B. (1999). Transmission electron microscopy study of the nitridation of the (0001) sapphire surface. *Applied Physics Letters, 75*(26), 4115-4117.

Vennéguès, P., Bougrioua, Z., & Guehne, T. (2007). Microstructural characterization of semipolar GaN templates and epitaxial-lateral-overgrown films deposited on m-plane sapphire by metalorganic vapor phase epitaxy. *Japanese Journal of Applied Physics, 46*(7R), 4089-4095.

Vennéguès, P., Zhu, T., Martin, D., & Grandjean, N. (2010). Study of the epitaxial relationships between III-nitrides and M-plane sapphire. *Journal of Applied Physics, 108*(11), Article#113521.

Voelkel, R., Vogler, U., Bich, A., Pernet, P., Weible, K. J., Hornung, M., . . . Harzendorf, T. (2010). Advanced mask aligner lithography: new illumination system. *Optics Express, 18*(20), 20968-20978.

Vu, T. D., Chen, Z., Zeng, X., Jiang, M., Liu, S., Gao, Y., & Long, Y. (2019). Physical vapour deposition of vanadium dioxide for thermochromic smart window applications. *Journal of Materials Chemistry C, 7*(8), 2121-2145.

Walker, D., Monroy, E., Kung, P., Wu, J., Hamilton, M., Sanchez, F., . . . Razeghi, M. (1999). High-speed, low-noise metal–semiconductor–metal ultraviolet photodetectors based on GaN. *Applied Physics Letters, 74*(5), 762-764.

Wang, J., Xu, F., He, C., Zhang, L., Lu, L., Wang, X., . . . Shen, B. (2017). High quality AlN epilayers grown on nitrided sapphire by metal organic chemical vapor deposition. *Scientific Reports, 7*, Article#42747.

Wang, W., Yang, Z., Lu, Z., & Li, G. (2018). High responsivity and low dark current nonpolar GaN-based ultraviolet photo-detectors. *Journal of Materials Chemistry C, 6*(25), 6641-6646.

Wang, X., Zhang, Y., Chen, X., He, M., Liu, C., Yin, Y., . . . Li, S. (2014). Ultrafast, superhigh gain visible-blind UV detector and optical logic gates based on nonpolar a-axial GaN nanowire. *Nanoscale, 6*(20), 12009-12017.

Wernicke, T., Netzel, C., Weyers, M., & Kneissl, M. (2008). Semipolar GaN grown on m-plane sapphire using MOVPE. *Physica Status Solidi c, 5*(6), 1815-1817.

Weyher, J., Ashraf, H., & Hageman, P. (2009). Reduction of dislocation density in epitaxial GaN layers by overgrowth of defect-related etch pits. *Applied Physics Letters, 95*(3), Article#031913.

Won, Y., So, B., Woo, S., Lee, D., Kim, M., Nam, K., . . . Nam, O. (2014). Effect of nitridation on the orientation of GaN layer grown on m-sapphire substrates using hydride vapor phase epitaxy. *Journal of Ceramic Processing Research, 15*(2), 61-65.

Wu, X., Brown, L., Kapolnek, D., Keller, S., Keller, B., DenBaars, S., & Speck, J. (1996). Defect structure of metal-organic chemical vapor deposition-grown epitaxial (0001) GaN/$Al_2O_3$. *Journal of Applied Physics, 80*(6), 3228-3237.

Wu, Z., Song, P., Shih, T., Pang, L., Chen, L., Lin, G., . . . Shen, W. (2017). In situ site-specific gallium filling and nanograin growth for blocking of threading defects in semipolar (11-22) GaN. *Crystal Growth & Design, 17*(9), 4687-4693.

Xia, H., Xia, Q., & Ruoff, A. L. (1993). High-pressure structure of gallium nitride: Wurtzite-to-rocksalt phase transition. *Physical Review B, 47*(19), Article#12925.

Xie, F., Lu, H., Xiu, X., Chen, D., Han, P., Zhang, R., & Zheng, Y. (2011). Low dark current and internal gain mechanism of GaN MSM photodetectors fabricated on bulk GaN substrate. *Solid-State Electronics, 57*(1), 39-42.

Xu, G., Salvador, A., Kim, W., Fan, Z., Lu, C., Tang, H., . . . Goldenberg, B. (1997). High speed, low noise ultraviolet photodetectors based on GaN pin and AlGaN (p)-GaN (i)-GaN (n) structures. *Applied Physics Letters, 71*(15), 2154-2156.

Xu, S., Zhang, J., Cao, Y., Zhou, X., Xue, J., Lin, Z., . . . Hao, Y. (2012). Improvements in (11-22) semipolar GaN crystal quality by graded superlattices. *Thin solid films, 520*(6), 1909-1912.

Yamamoto, S., Zhao, Y., Pan, C.-C., Chung, R. B., Fujito, K., Sonoda, J., . . . Nakamura, S. (2010). High-efficiency single-quantum-well green and yellow-green light-emitting diodes on semipolar (20-21) GaN substrates. *Applied Physics Express, 3*(12), Article#122102.

Yang, H., Zhang, X., Wang, S., Wang, Y., Luan, H., Dai, Q., . . . Cui, Y. (2016). Effects of Si-doping on structural, electrical, and optical properties of polar and non-polar AlGaN epi-layers. *Superlattices and Microstructures, 96*, 1-7.

Young, E. C., Wu, F., Romanov, A. E., Tyagi, A., Gallinat, C. S., DenBaars, S. P., . . . Speck, J. S. (2010). Lattice tilt and misfit dislocations in (11-22) semipolar GaN heteroepitaxy. *Applied Physics Express, 3*(1), Article#011004.

Zainal, N., Ahmad, M., Maryam, W., Samsudin, M., Waheeda, S., Taib, M. I. M., & Hassan, Z. (2020). Performance of polycrystalline GaN based metal-semiconductor-metal (MSM) photodetector with different contact. *Superlattices and Microstructures, 138*, Article#106369.

Zakutayev, A. (2016). Design of nitride semiconductors for solar energy conversion. *Journal of Materials Chemistry A, 4*(18), 6742-6754.

Zhang, Y., Bai, J., Hou, Y., Smith, R., Yu, X., Gong, Y., & Wang, T. (2016). Defect reduction in overgrown semi-polar (11-22) GaN on a regularly arrayed micro-rod array template. *AIP Advances, 6*(2), Article#025201.

Zhao, G., Wang, L., Li, H., Meng, Y., Li, F., Yang, S., & Wang, Z. (2018). Structural and optical properties of semi-polar (11-22) InGaN/GaN green light-emitting diode structure. *Applied Physics Letters, 112*(5), Article#052105.

Zhao, G., Wang, L., Yang, S., Li, H., Wei, H., Han, D., & Wang, Z. (2016). Anisotropic structural and optical properties of semi-polar (11–22) GaN grown on m-plane sapphire using double AlN buffer layers. *Scientific Reports, 6*(1), 1-10.

Zhao, Y., Farrell, R. M., Wu, Y.-R., & Speck, J. S. (2014). Valence band states and polarized optical emission from nonpolar and semipolar III–nitride quantum well optoelectronic devices. *Japanese Journal of Applied Physics, 53*(10), Article#100206.

Zhao, Y., Yan, Q., Huang, C.-Y., Huang, S.-C., Shan Hsu, P., Tanaka, S., . . . Van de Walle, C. G. (2012). Indium incorporation and emission properties of nonpolar and semipolar InGaN quantum wells. *Applied Physics Letters, 100*(20), Article#201108.

Zheng, W., Huang, F., Zheng, R., & Wu, H. (2015). Low-Dimensional Structure Vacuum-Ultraviolet-Sensitive (λ< 200 nm) Photodetector with Fast-Response Speed Based on High-Quality AlN Micro/Nanowire. *Advanced Materials, 27*(26), 3921-3927.

Zhu, T., Ding, T., Tang, F., Han, Y., Ali, M., Badcock, T., . . . Oliver, R. A. (2016). Self-assembled multilayers of silica nanospheres for defect reduction in non-and semipolar gallium nitride epitaxial layers. *Crystal Growth & Design, 16*(2), 1010-1016.

Zhu, T., Sutherland, D., Badcock, T. J., Hao, R., Moram, M. A., Dawson, P., . . . Oliver, R. A. (2013). Defect reduction in semi-polar (11-22) gallium nitride grown using epitaxial lateral overgrowth. *Japanese Journal of Applied Physics, 52*(8S), Article#08JB01.

# LIST OF PUBLICATIONS AND PAPERS PRESENTED

## List of Publications

1. **Makinudin, A. H. A.,** Al-Zuhairi, O., Bakar, A. S. A., Anuar, A., & Supangat, A. (2020). Disilane Doping of Semi-Polar (11-22) n-GaN: The Impact of Terrace-Like Evolution toward the Enhancement of the Electrical Properties. *Thin Solid Films*, Article#138489. https://doi.org/10.1016/j.tsf.2020.1384891

2. **Makinudin, A. H. A.,** Al-Zuhairi, O., Anuar, A., Zainorin, M. Z., Bakar, A. S. A., DenBaars, S. P., & Supangat, A. (2020). Impact of crystallinity towards the performance of semi-polar (11-22) GaN UV-photodetector. *Materials Letters*, Article#129244. https://doi.org/10.1016/j.matlet.2020.129244

3. **Makinudin, A. H. A.**, Al-Zuhairi, O., Anuar, A., Bakar, A. S. A., DenBaars, S. P., & Supangat, A. (2019). Impact of a Strained Periodic Multilayer on the Surface and Crystal Quality of a Semipolar (11–22) GaN Template. *Crystal Growth & Design, 19*(11), 6092-6099.

4. Anuar, A., **Makinudin, A. H. A.**, Al-Zuhairi, O., Bakar, A. S. A., & Supangat, A. (2020). Crystal quality and surface structure tuning of semi-polar (11–22) GaN on m-plane sapphire via in-situ multiple ammonia treatment. *Thin Solid Films*, *697,* Article#137817.

5. Anuar, A., **Makinudin, A. H. A.**, Al-Zuhairi, O., Chanlek, N., Bakar, A. S. A., & Supangat, A. (2020). Growth of semi-polar (11-22) GaN on m-plane sapphire via In-Situ Multiple Ammonia Treatment (I-SMAT) method. *Vacuum, 174*, Article#109208.

6. Al-Zuhairi, O., Bakar, A. S. B. A., **Makinudin, A. H. A.**, Khudus, M. I. M. A., Azman, A., Kamarundzaman, A., & Supangat, A. (2018). Effect of low NH3 flux towards high quality semi-polar (11-22) GaN on m-plane sapphire via MOCVD. *Superlattices and Microstructures, 117*, 207-214.

## Papers Presented

1. **Makinudin, A. H. A,** Bakar, A. S. B. A., Al-Zuhairi, O., Azman, A., Kamarundzaman, A., Khudus, M. I. M. A., Supangat, A., (2018). *Controlling the growth mode of semi-polar (11-22) GaN epi-layers utilizing ammonia flux variation via MOCVD*. Paper presented at the International Workshop on Nitride Semiconductors (IWN), 11-16 November 2018, Kanazawa, Japan.

2. Al-Zuhairi, O., Bakar, A. S. B. A., **Makinudin, A. H. A,** Khudus, M. I. M. A., Supangat, A., (2018). *A reduction in the anisotropic characteristics of semi-polar (11-22) epitaxial layers by embedded AlN/GaN multi-layer via MOCVD.* Paper presented at the International Workshop on Nitride Semiconductors (IWN), 11-16 November 2018, Kanazawa, Japan.